



國立中山大學材料與光電科學學系

博士論文

Department of Materials and Optoelectronic Science

National Sun Yat-sen University

Doctorate Dissertation

非晶與奈米晶多層膜結構在壓縮測試下之

機械性質與變形行為

Mechanical Properties and Deformation Behaviors in

Amorphous/Nanocrystalline Multilayers under Microcompression

研究生：劉名哲

Ming-Che Liu

指導教授：黃志青 博士

Dr. Jacob Chih-Ching Huang

中華民國 一 百 年 十 月

Oct. 2011

國立中山大學研究生學位論文審定書

本校材料與光電科學學系博士班

研究生劉名哲（學號：D963060009）所提論文

非晶與奈米晶多層膜結構在壓縮測試下之機械性質與變形行為
Mechanical Properties and Deformation Behaviors in
Amorphous/Nanocrystalline Multilayers under Microcompression

於中華民國 100 年 10 月 11 日經本委員會審查並舉行口試，符合
博士學位論文標準。

學位考試委員簽章：

召集人 聶台岡

聶台岡

委員 黃志青

黃志青

委員 林仁輝

林仁輝

委員 鄭憲清

鄭憲清

委員 朱瑾

朱瑾

委員 _____

委員 _____

委員 _____

委員 _____

委員 _____

指導教授(黃志青)

黃志青

(簽名)

謝誌

轉眼間就過了五年多，在這五年多的研究生涯有了許多珍貴的回憶；首先，感謝指導教授黃志青老師孜孜不倦的教導；在學術上，總是不厭其煩的為我們解惑，常常遇到不順遂的時後，黃老師的加油與鼓勵，往往給了我們前進的力量，讓我們在追求學問的道路上不會感到寂寞，黃老師的指導與教誨，讓我們在實驗研究的方向上不會感到迷失；在生活上，老師的關心總是不會少，遇到了任何困難，老師總是在旁給予最大的協助與幫忙，在老師的開導與幫助下，讓我們能夠更專心於研究上；本人在此獻上誠摯的一聲：「老師您辛苦了，謝謝您！」；能夠跟隨老師學習新知並在老師的指導下做研究真的是一件很幸福的事情；另外，由衷地感謝美國田納西大學聶台岡教授、國立成功大學機械系林仁輝教授、國立中山大學機械系鄭憲清教授、國立台灣科技大學朱瑾教授在百忙之中抽空擔任口試委員，在論文的審查與口試過程中，給予許多寶貴的建議及指導，使得論文可以更加完整。

此外，在美國三個月學術交流其間，也要特別感謝聶台岡教授在實驗上及科學研究上的細心指導，其追求學問的嚴謹態度是我們所追隨的目標，也感謝聶師母、P. K. Liaw 教授與師母在美國其間對於生活上的幫助與照顧；還有 L. Wang 學姊、E. W. Huang 學長、J. Y. Hung、K. J. Lee、K. C. Chu 等朋友們在生活與實驗上的幫助，使得在美國田納西大學的三個月期間有非常難忘且多采多姿的回憶。

也要感謝材料系上以及奈米中心的各實驗室的技術員，感謝你們在實驗上的指導與協助，尤其是電子顯微鏡技術員王良珠小姐、林明政先生、X 光繞射儀技術員李秀月小姐，以及聚焦離子束技術員陳彥文學長，由於你們的幫忙使得研究可以順利的進行。另外，感謝所辦朱惠敏小姐、顏秀芳小姐、陳秀月小姐及奈米中心助理鹿文卿小姐與顏采蓉小姐在行政事務上的協助與幫忙，還有感謝熱心的華應麒大哥在生活上幫助以及待人處事態度上的教導。

在研究其間更受到研究室學長、學弟妹的幫助；首先研究室的精神領袖敬仁學長，

總是能開發新知，帶領著實驗室一起往前衝，在此論文中貢獻良多；還有已經畢業的科技新貴子翔學長，還記得剛進研究室時你總是默默關心新進成員並且跟大家打成一片，感謝學長的照顧與指導；感謝無所不能的育誠學長，每當遇到困難，總是有辦法從他身上找到答案，感謝育誠學長總是耐心的教導；感謝遠在美國打拼的宇庭學長，當初你樂觀的態度讓我覺得念博班充滿無限的希望；還有感謝志溢、友杰、鴻昇、志榮等學長的指導與幫助；還有一群充滿活力的學弟妹們，大豪、哲男、聖堯、碩陽、顛任、逸志、柏佑、婷婷、維昭、朝先、盈翰、sunny、嘉驊、中瀚，有了你們的陪伴，讓我的研究所生活充滿活力與能量，許多珍貴的回憶是一輩子都不會忘記的。還有中山材光系壘與東華材料系壘的大家的，感謝給了我在球場上無限的甜美回憶。接著要感謝我的好戰友--裴浩然大帥哥，還記得當初一起奮戰到白天的瘋狂日子，有你這個好夥伴，替我分憂解勞，真的是很幸運的一件事情，也先預祝你順利畢業囉！

最重要的要感謝一路相伴不離不棄夜間部同學--Q妹，感謝這一路來的陪伴與支持，每當遇到挫折時，總是會為我加油，給了我重新再來的勇氣，讓我有信念可以繼續走下去，一路上與我分享喜怒哀樂讓我倍感溫馨，謝謝妳！最後，我要特別地感謝我的家人，是你們提供我最佳的生長環境，生活上讓我無後顧之憂，可以全心全意投入在研究中，你們的支持與付出都會感念在心，我愛你們！

劉名哲 謹誌

於中山西灣

Content

Content	i
List of tables	v
List of figures	vi
中文摘要	xiv
Abstract	xvi
Chapter 1 Introduction.....	1
1-1 Amorphous alloys.....	1
1-2 The evolution of amorphous alloys	2
1-3 The development of Zr-based thin film metallic glass (TFMG)	3
1-4 Motivation	5
Chapter 2 Background and literature review	9
2-1 Manufacture methods of amorphous alloys.....	9
2-1-1 Cooling the gaseous state to the solid state	9
2-1-2 Cooling the liquid state to the solid state	10
2-1-3 Transforming the solid state to another solid state.....	10
2-2 The characters and forming conditions of amorphous alloys.....	11
2-2-1 Glass forming ability (GFA)	11
2-2-2 Supercooled liquid region (SCLR).....	12
2-2-3 The empirical rules for forming amorphous alloys.....	13
2-3 Principle of physical vapor deposition	15

2-3-1	Introduction of sputtering.....	15
2-3-2	DC and RF sputtering.....	16
2-3-3	Nucleation and growth of sputter-deposited films	17
2-3-4	Amorphous film growth.....	18
2-4	Properties of thin film metallic glasses.....	19
2-4-1	Thermal properties	19
2-4-2	Mechanical properties	20
2-4-3	Electrical Properties	22
2-4-4	Magnetic properties.....	23
2-4-5	Chemical properties.....	23
2-5	Characterization of microscale mechanical properties.....	24
2-5-1	Introduction to microcompression tests	24
2-5-2	Parameters of microcompression tests	24
2-5-3	Microscale mechanical properties on micropillars.....	27
2-5-4	Microscale mechanical properties on multilayer structures.....	31
Chapter 3 Experimental procedures		35
3-1	Raw materials	35
3-2	Sample preparation.....	35
3-2-1	Pretreatment for substrate.....	35
3-2-2	Preparation for monolithic thin films and multilayer thin films	36
3-3	Property measurements and analyses	37
3-3-1	X-ray diffraction.....	37
3-3-2	SEM observations	37
3-3-3	Qualitative and quantitative component analyses	37

3-4	Nanoindentation tests	38
3-5	Microcompression tests	38
3-5-1	Preparation for microcompression samples	38
3-5-2	Microcompression tests using nanoindentation system	39
3-5-2	Preparation for TEM foils of the deformed micropillars	39
3-6	In-situ TEM nanocompression tests	40
3-6-1	Preparation for nanocompression samples	40
3-6-2	In-situ TEM nanocompression tests using Hysitron system	41
Chapter 4	Experimental results.....	42
4-1	Sample preparations	42
4-2	EDS and XRD analyses	43
4-3	Mechanical property analyses	44
4-4	Microcompression tests	46
4-4-1	Results for ZrCu amorphous, Zr and Cu nanocrystalline micropillars	46
4-4-2	Results for ZrCu/Zr multilayer micropillars	48
4-4-3	Results for ZrCu/Mo and ZrCu/Cu multilayer micropillars.....	50
4-5	TEM analyses of the microstructures on deformed micropillars	53
4-5-1	TEM analyses for ZrCu/Zr micropillars.....	53
4-5-2	TEM analyses for ZrCu/Cu micropillars.....	55
4-6	In-situ TEM compression tests	56
4-7	Interface strength of multilayer pillars	57
Chapter 5	Discussion.....	59
5-1	Microcompression tests	59

5-1-1	Calculation of Young's modulus.....	59
5-1-2	Homogeneous-like and shear-band deformation of multilayer micropillars	61
5-1-3	Interaction of amorphous/crystalline interface.....	64
5-2	In-situ TEM compression tests	66
5-3	Interface strength of the inclined multilayer pillars.....	70
Chapter 6	Conclusions	76
Chapter 7	Prospective and future work.....	79
References	80
Tables	90
Figures	96

List of tables

Table 1.1	Fundamental properties and application fields of bulk amorphous and nanocrystalline alloys.....	85
Table 1.2	Bulk metallic glasses and their developed year.....	86
Table 2.1	Binary amorphous systems and mixing enthalpy values calculated based on Miedema's macroscopic model.....	87
Table 4.1	Deposition rates with variant target materials at different powers.....	88
Table 4.2	Summary of the modulus and hardness of the as-deposited thin films and silicon wafer, obtained from nanoindentation.....	89
Table 5.1	Summary of the results of various tested pillars, obtained from the microcompression tests.....	90

List of figures

Figure 1.1	Two typical arrangement of atomic structures in (a) crystal and (b) amorphous alloy. The inset Fourier transforms in left coner shows the structural differences.....	91
Figure 1.2	The shiny and smooth outward apperance of liquid metal.....	92
Figure 1.3	Schematic illustration of the splat quenching method.....	92
Figure 1.4	Schematic illustration of the two rollers quenching process.....	93
Figure 1.5	The relationship of critical casting thickness with the date of discovery.....	94
Figure 2.1	Schematic drawing of (a) sputtering and (b) vacuum evaporation.....	95
Figure 2.2	The DSC trace of a metallic glass.....	96
Figure 2.3	The relationship of R_c and ΔT_x	97
Figure 2.4	Mechanisms for the stabilization of supercooled liquid and the high glass-forming ability.....	98
Figure 2.5	Events that occur on a surface being bombarded with energetic atomic-sized particle.....	99
Figure 2.6	Schematic illustrations of three basic growth modes for thin film.....	100
Figure 2.7	DSC thermography curve of the Pd-TFMG.....	101
Figure 2.8	DSC thermography curve of the Zr-TFMG.....	101
Figure 2.9	TTT diagram for the onset of crystallization in the Zr-TFMG.....	102
Figure 2.10	TTT diagram for the onset of crystallization in the Pd-TFMG.....	102
Figure 2.11	Relationship between tensile strength or Vickers hardness (H_v) and E for various bulk amorphous alloys.....	103
Figure 2.12	The arrangement of atoms in (a) crystalline and (b) amorphous states.....	103
Figure 2.13	The illustration of the shear transformation zones (STZs) (a) before shear	

	deformation and (b) after shear deformation in two-dimensional space	104
Figure 2.14	Schematic drawing of the fluid zones of amorphous alloy.....	105
Figure 2.15	SEM micrograph of the cantilever microbeam for the bending test.....	106
Figure 2.16	SEM observations of the damaged surfaces at the fixed end of Pd-TFMGs microbeams deformed by bending: (a) sample 1, (b) sample 2, (c) sample 3.....	107
Figure 2.17	Resistivity and annealing temperature of Pd-TFMG	108
Figure 2.18	Change in electrical resistance with increasing annealing temperature for Zr-based amorphous alloy.....	108
Figure 2.19	Schematic of a cylindrical post and its base.....	109
Figure 2.20	Effect of specimen geometry (fillet size) on numerical simulation. The inset shows an enlargement of the circled region to facilitate comparison.....	109
Figure 2.21	(a) Deformed configuration of a circular cylindrical pillar with an aspect ratio $\alpha = 5$ at a strain of 0.1. (b) Deformed configuration of the pillar at the same strain of 0.1, but now considering friction. (c) Input and output stress-strain curves for a pillar with an aspect ratios $\alpha = 2\sim 5$, both with friction and without friction (NF).....	110
Figure 2.22	Effect of taper and system misalignment on numerical simulations output.....	111
Figure 2.23	Mechanical behavior at room temperature for Ni ₃ Al-Ta microsamples. (A) Representative stress-strain curves for microsamples ranging in size from 20 to 0.5 μm in diameter. (B) A SEM image of 20- μm diameter microsample, where the sample achieved $\sim 10\%$ strain during the rapid burst of deformation. (C) A SEM image of 1- μm -diameter microsample after testing.....	112
Figure 2.24	Stress-strain behaviors of micropillars: flow stresses increase significantly for pillars with a diameter of 500 nm and less.....	113
Figure 2.25	(a) A stress-strain curve for a 2 μm diameter micro-crystal of Ni ₇₆ Al ₂₄ . Strain	

	bursts are indicated by arrows. (b) A SEM image of the same micro-crystal shown in (a). The appearance of slip lines on the surface of the micro-crystal are indicated by arrows.....	114
Figure 2.26	Dark-field TEM images showing the deformation of (a) 640 nm and (c) 365 nm diameter pillars: the numbering in (a) and (c) corresponds to the instances numbered in the stress-response curves in (b) and (d), respectively, the inset in (d) being true stress. Open and solid white arrows annotate SBs and local bumps, respectively.....	115
Figure 2.27	Stress and morphological evolutions of nanopillars with diameters of (a) 100 nm and (b) 70 nm, respectively, as functions of strain.....	116
Figure 2.28	TEM microstructure of a deposited Cu-Zr nanolaminate. Between the Cu layers are amorphous Cu ₄ Zr ₃ layers.....	117
Figure 2.29	Stress-strain curve for Cu-Zr nanolaminate deformed at a strain rate of 2x10 ⁻³ s ⁻¹	117
Figure 2.30	Cross-sectional (a) and planview (b) TEM images of the as-deposited 5 nm/35 nm nanocrystalline Cu and amorphous Cu/Zr intermixing multilayer nanostructures. (c) True stress-strain curves for Cu/Zr nanolaminates. (d) The top-view of the gauge section after fracture for 5/35 Cu/Zu nanolaminate.....	118
Figure 2.31	Bright field TEM images of 100 nm Cu/ <i>a</i> -PdSi multilayer: (a) as-deposited and (b) tip region of a bent foil. The <i>a</i> -PdSi layers appear as thin dark lines.....	119
Figure 2.32	Schematic illustration of slip transmission across nanometer-scale crystalline (c)/amorphous (a)/crystalline sandwich structures.....	120
Figure 2.33	Shear band penetration or deflection on the interface of dissimilar materials.....	120
Figure 3.1	The flow chart of the experimental procedures in this study.....	121
Figure 3.2	Schematic illustrations for co-sputtering process.....	122

Figure 3.3	The standard Nano Indenter [®] XP is a complete, turnkey system consisting of the major components illustrated.....	123
Figure 3.4	The appearance of dual focus ion beam system (FIB, SEIKO SMI3050).....	124
Figure 3.5	SEM micrographs of the flat-punch tip: (a) plane view and (b) side view.....	124
Figure 3.6	SEM micrograph showing the projected area of the punch tip.....	125
Figure 3.7	Schematic illustration for fabricating TEM specimen by FIB.....	125
Figure 3.8	TEM sample preparation procedures: (a) Zr-TFMG micropillar with 1 μm diameter before compression test, (b) carbon is deposited around the pillar to fill the empty, (c) an energetic Ga ion beam is used to cut the trench, and (d) TEM sample can be further thinned by using the Ga ion beam with relative lower voltage or current.....	126
Figure 3.9	Typical six steps of in-situ lift-out method: (A) first cut; (B) release cut; (C) tip attach; (D) extraction; (E) holder attach; (F) and tip separation.....	127
Figure 3.10	Showing the PI 95 TEM picoindenter holder. Holder detail: by positioning the indenter tip directly opposite the sample and perpendicular to the electron beam, the deformation event can be viewed in situ.....	127
Figure 4.1	Cross-sectional TEM bright-field image of the L7 multilayer thin film.....	128
Figure 4.2	Cross-sectional TEM bright-field image of the L3 multilayer thin film.....	128
Figure 4.3	Cross-sectional SEM images of (a) ZrCu/Mo/ZrCu and (b) ZrCu/Cu/ZrCu multilayer thin films. The thickness of each layer is close to $500 \pm 10 \text{ nm}$	129
Figure 4.4	XRD pattern of the as-deposited ZrCu thin film.....	129
Figure 4.5	XRD pattern of the as-deposited pure Zr thin film.....	130
Figure 4.6	XRD pattern of the as-deposited pure Cu thin film.....	130
Figure 4.7	A representative load-displacement data for an indentation experiment. The quantities shown are P_{max} : the peak indentation load; h_{max} : the indenter	

	displacement at peak load; h_f : the final depth of the contact impression after unloading; and S : the initial unloading stiffness.....	131
Figure 4.8	SEM micrograph of the undeformed ZrCu micropillar, 1 μm in diameter.....	132
Figure 4.9	SEM micrographs of the undeformed (a) L7 and (b) L3 micropillars, 1 μm in diameter. (Note: In Fig. 4.9(b), the dark layer on the bottom of pillar is silicon wafer.).....	132
Figure 4.10	The compressive stress-strain curve of the monolithic ZrCu amorphous micropillar loaded at a strain rate of $2 \times 10^{-3} \text{ s}^{-1}$ to a preset displacement of 300 nm.....	133
Figure 4.11	SEM micrograph of the deformed monolithic ZrCu amorphous micropillar.....	134
Figure 4.12	The compressive stress-strain curve of monolithic Zr nanocrystalline micropillar loaded at a strain rate of $2 \times 10^{-3} \text{ s}^{-1}$ to a preset displacement of 300 nm.....	134
Figure 4.14	The engineering strain-stress curves of different micropillar samples loaded by microcompression tests.....	135
Figure 4.15	SEM micrographs showing the appearance of monolithic nanocrystalline Cu deformed micropillars samples, 1 μm in diameter.....	135
Figure 4.16	The engineering stress and strain curves of the L7 and L3 multilayered pillars compressed at $2 \times 10^{-3} \text{ s}^{-1}$ to a predetermined displacement of 300 nm (~15% strain).....	136
Figure 4.17	SEM micrograph of the deformed L7 ZrCu/Zr multilayer micropillar.....	136
Figure 4.18	SEM micrograph of the deformed L3 ZrCu/Zr multilayer micropillar. The top amorphous layer is appreciably barreled. Whereas many localized shear bands form, there is no sign of deep penetration of shear bands in the nanocrystalline Zr layer.....	137

Figure 4.19	(a) SEM micrograph showing the compressed ZrCu/Zr (100/100 nm) pillar to a present displacement of 300 nm. (b) The engineering stress and strain curve of the ZrCu/Zr laminated pillar loaded at $2 \times 10^{-3} \text{ s}^{-1}$ to a preset displacement of 300 nm.....	137
Figure 4.20	The engineering stress and strain curve of five-layer (ZrCu/Mo laminates) pillar loaded at $2 \times 10^{-3} \text{ s}^{-1}$ to a preset displacement of 300 nm.....	138
Figure 4.21	SEM micrographs showing: (a) 1- μm -diameter five-layer ZrCu/Mo micropillar. (b) the compressed pillars to a present displacement of 300 nm.....	138
Figure 4.22	(a) SEM micrograph showing the ZrCu/Cu five-layer pillar compressed to a predetermined displacement of 300 nm ($\sim 15\%$ strain), and (b) the recorded engineering stress and strain curve.....	139
Figure 4.23	SEM micrographs showing the appearance of the ZrCu/Cu 100/10 nm deformed micropillars, 1 μm in diameter.....	139
Figure 4.24	SEM micrographs showing the appearance of the round deformed micropillars of 100/100 nm ZrCu/Cu micropillar, 1 μm in diameter.....	140
Figure 4.25	SEM micrographs showing the appearances of the (a) undeformed and (b) strained up to $\sim 100\%$ 100/100 nm ZrCu/Cu rectangular micropillars. (c) A typical true stress-strain curve of the 100/100 nm ZrCu/Cu rectangular micropillar subjected to microcompression test.....	141
Figure 4.26	TEM longitudinal section of the L7 multilayer pillars compressed to a predetermined displacement of 300 nm ($\sim 15\%$ strain).....	142
Figure 4.27	TEM micrographs showing the ZrCu/Zr interface of the deformed L3 pillar. The shear bands were stopped by Zr crystalline layer. The thickness of top amorphous was decreased from the 550 nm to 280 nm after the microcompression and the Zr layer was decreased from 880 nm to 830 nm. (b) and (c) TEM micrographs of the amorphous/crystalline interface and the	

	deformed crystalline Zr layer.....	143
Figure 4.28	TEM micrographs showing the appearances of the deformed (a) 100/10 nm and (b) 100/100 nm ZrCu/Cu round micropillars.....	144
Figure 4.29	(a) TEM micrographs showing the appearances of the deformed 100/100 nm ZrCu/Cu rectangular micropillars. (b) High-magnitude TEM image of the circular region marked in Figure 4.29 (a).....	145
Figure 4.30	Representative load-displacement curves of the in situ TEM nanocompression tests on the ZrCu thin film metallic glass nanopillars, 140 nm in diameter....	146
Figure 4.31	Video snaps taken from the in-situ TEM compression showing the deformation of Zr-based pillar (Pillar 1). The different stages of the nanocompression process are depicted by individual frames [(a)-(h)] at different strains: (a) undeformed, (b) ~2%, (c) ~4%, (d) ~6%, (e) ~8%, (f) ~10%, (g) ~15%, and (h) ~20%. The corresponding stress strain curve is inserted on the left bottom corner for point to point correspondence.....	147
Figure 4.32	SEM image of the undeformed multilayered pillar, with labels of the diameter, height, and composition.....	148
Figure 4.33	SEM images of the pillar deformed to the preset displacement of 260 nm, taken from two sides of the pillar.....	148
Figure 4.34	SEM images of the pillar deformed till to failure, taken from two sides of the pillar.....	149
Figure 4.35	The compression stress and strain curve of the inclined multilayered pillar deformed till to failure.....	149
Figure 5.1	Schematic illustration for the deformation in a tapered sample.....	150
Figure 5.2	Schematic illustration of the deformation mechanism in the metallic amorphous/crystalline nanolayered composites as a function of metallic layers thickness. A: inherently ductile metallic amorphous layers (e.g. ZrCu) with L_a	

	thickness; B: soft pure metallic layers (e.g. Cu). Pronounced semi-homogeneous and superplastic-like deformation can occur when $L_a \leq L_m \leq L_2$	151
Figure 5.3	Showing the deformation planar defects (twins and stacking faults) in the nano-scale grained Zr layer, as indicated in Figure 5.3(c).....	152
Figure 5.4	Schematic illustration of interaction between the amorphous/crystalline interfaces.....	153
Figure 5.5	HRTEM lattice image showing one of the twinning operation in the nano-crystalline Zr layer. The (0002) planes in the matrix (on the left) possess an angle of 130° with respect to the (0002) planes in the twin region (on the right). The habit plane (or the <i>KI</i> undistorted plane) $(11\bar{2}1)$ lying at the center, possessing an angle of 68.93° with respect to both (0002) planes in the matrix and in the twin.....	154
Figure 5.6	The calculated solid line showing the estimate of the minimum stress required to raise the strain energy high enough to allow for shear band formation. (Upper right region: shear banding heterogeneous deformation; lower left region: homogeneous deformation.).....	155
Figure 5.7	Change in cross-sectional area versus distance for Figures 4.31(b), (d), (f), and (h). Distance stands for distance the top of the pillar sample.....	155
Figure 5.8	Area change ratio as a function of the distance from the specimen top (normalized by the base diameter) at three representative deformation stages with free volume contours in the insets. Contour plots are given in deformed mesh with displacement magnification ratios being 1 in all three directions.....	156

中文摘要

塊狀金屬玻璃(bulk metallic glass)在工程應用上展現出許多良好的性質，例如高強度、高抗腐蝕能力等等；但是除了良好的機械性質之外，其脆性的缺點限制了金屬玻璃與金屬玻璃薄膜的應用範圍。目前已有許多研究指出，利用複材的概念與結構，可以有效地解決這個問題。例如利用添加強化相在金屬玻璃或金屬玻璃薄膜中或是將其做熱處理之製程，皆可有效改善金屬玻璃之缺點。

在本篇研究論文中，利用單軸向微壓縮測試，研究非晶與奈米晶多層膜微米柱在室溫下之機械性質與變形行為。結晶材料我們選用面心立方(face-centered cubic)、六方最密堆積(hexagonal close-packed)、體心立方(body-centered cubic)，探討不同結晶結構對非晶材料變形之影響；結果顯示，在金屬玻璃薄膜中插入結晶鍍層薄膜，此特殊結構可以使得金屬玻璃薄膜之脆性被有效的改善並展現出高度的延性；其塑性形變量在室溫下可達到 50%。除此之外，我們也將延性較好但強度較低之結晶銅與金屬玻璃薄膜製作成另一種多層膜結構；利用一系列的研究與對結晶銅層厚度改變的探討，發現最佳的厚度，可以使得金屬玻璃薄膜與結晶銅在壓縮測試下產生類似超塑性變形的行為；因此可以推斷出多層膜的變形行為與結晶銅層厚度有很大的關係；然而，經由理論的計算與觀察變形後試片的微觀組織可以進一步發現，金屬玻璃薄膜與結晶銅層在 100 奈米的厚度之下，會產生互相容的流變應力(flow stress)與可匹配的塑性區域(plastic zone)，最後造成此有趣的多層膜結構在微米尺度的壓縮測試形成均勻且類似超塑性變形的行為；改善了金屬玻璃缺乏延性的缺點之後，將顯著提升材料的機械性質並且可以被廣泛的應用於微機電元件中。

除此之外，我們也利用有限元素分析法模擬金屬玻璃薄膜在直徑 140 奈米尺度下之變形行為，試圖找出金屬玻璃材料產生均勻變形之臨界尺度，經由實驗與模擬的結果可

以發現，剪切帶的形成會聚集在試片的上半部，並且研究出在 140 奈米尺度下，金屬玻璃材料依然是以剪切帶的行為來造成試片之破壞。

最後，我們利用理論的計算可以得知我們所研究的金屬玻璃薄膜與結晶層多層膜間的介面強度，此性質將會影響到試片設計與實驗之結果；經由理論計算之結果可以發現，金屬玻璃薄膜與結晶層薄膜之強度與其他金屬與金屬或金屬與陶瓷材料之介面強度相似；因此也提升了此多層膜結構往後可發展的空間。



Abstract

BMGs (bulk metallic glasses) exhibit many exceptional advantages for engineering applications, such as high strength, good corrosion resistance, etc. Despite of having these excellent properties, the brittle nature of metallic glasses in the bulk and thin film forms inevitably imposes limitation and restricts the wide application of BMGs and TFMGs. Composite concept might be another idea to solve this dilemma. In order to manufacture the bulk metallic glass composites (BMGCs), the approaches are classified into two categories: the intrinsic and extrinsic methods. For the intrinsic method, the in situ process and heat treatment process are two kinds of ways in common uses. Adding reinforcements into the BMGs or TFMGs is extensively used to manufacture composites in the extrinsic method.

In this study, the deformation behaviors of multilayer (amorphous/nanocrystalline) micropillars are studied by uniaxial microcompression tests at room temperature. The nanocrystalline layer to be coupled with the amorphous layer can be of either face-centered cubic (FCC), hexagonal close-packed (HCP) or body-centered cubic (BCC) in crystal structure. The current study demonstrates that brittle problem of a metallic glass coating can be alleviated by percolating with a nanocrystalline metallic underlayer. The brittle thin film metallic glass can become highly ductile and exhibit a plastic strain over 50% at room temperature. The present study has an important implication for MEMS applications, namely, the life span of a brittle amorphous layer can be significantly improved by using an appropriate metallic underlayer.

The brittle problem of thin film ZrCu metallic glasses was also treated by invoking soft Cu layers with optimum film layer thickness. Such multilayered amorphous/crystalline

samples exhibit superplastic-like homogeneous deformation at room temperature. It is found that the deformability of the resultant micropillars depends on the thickness of Cu layers. Microstructural observations and theoretical analysis suggest that the superplastic-like deformation mode is attributed to homogeneous co-deformation of amorphous ZrCu and nanocrystalline Cu layers because the 100 nm-thick Cu layers can provide compatible flow stress and “plastic zone” size well matched with those of ZrCu amorphous layers.

Besides, we also made attempts to investigate the critical sample size below which shear band localization would disappear and the sample can deform homogeneously. In situ TEM compression was conducted on amorphous ZrCu nanopillars to study shear band formation behavior. The nanopillar is 140 nm in diameter and with a taper angle of 3° . Experimental observations and simulations based on a free-volume model both demonstrate that the deformation was localized near the top of the tapered metallic glass pillar.

Eventually, the interface nature of metallic glass amorphous/crystalline was characterized through evaluating its energy and validated by the mechanical response of micropillar with $\sim 45^\circ$ inclined interface under compression. The calculated results showed that the ZrCu/Zr interface energy resides several joules per meter square, meaning that the Zr/ZrCu interface is inherently strong. The high strong adhesion ability of ZrCu/Zr interface was further confirmed by shear fracture happening rightly within the Zr layers rather than along the interface when compressing the ZrCu/Zr micropillars with 45° inclined interface.

Chapter 1 Introduction

1-1 Amorphous alloys

Amorphous alloys, in the substantial concept, are the metallic glasses with a disordered atomic-scale structure, and without crystalline periodicity. In contrast with crystalline materials (Figure 1.1a) [1], with a highly ordered arrangement of atoms, amorphous alloys are non-crystalline and also known as packing with short range order structures. Therefore, the atoms in amorphous alloys are not completely random, but retain a greater degree of short range order than that in the liquid, and both lack of the long range order arrangement, as shown in Figure 1.1b [1]. In general, amorphous alloys also called as liquid metals, glassy metals, non-crystalline metals, and metallic glasses. Also, amorphous alloys are glasses without transparency and look like shiny, opaque, smooth metals, as shown in Figure 1.2 [2]. Because of having a unique atomic arrangement, the amorphous alloys exhibit some special mechanical and physical characteristics, compared to the corresponding crystalline alloys, such as the followings; (1) much larger elastic elongation limit of about 2% [3], (2) high strength up to 5 GPa [4], (3) much larger elastic energy up to yielding, (4) absence of distinct plastic elongation due to inhomogeneous deformation mode, (5) relatively larger impact fracture energy, (6) better corrosion resistance, (7) easy shaping or forming ability [5], and (8) excellent electronic or magnetic properties [3, 6]. The features and future application potentials of amorphous alloys are summarized in Table 1.1 [6].

Over the last three decades, the series of metal alloys that display extraordinary resistance to crystallization in the undercooled liquid region have investigated by worldwide researchers. By the cooling processes, metal alloys readily vitrify to form bulk amorphous

alloys or bulk metallic glasses (BMGs). Bulk amorphous alloys exhibit very high strength, elastic strain limit, better corrosion resistance, as mentioned previously. Owing to these factors, researchers suggest that bulk amorphous metals will become widely used engineering materials in the future.

1-2 The evolution of amorphous alloys

In 1960, Klement et al. [7] first discovered the vitrification of a liquid metal alloy in the binary Au-Si alloy system. The splat quenching method [8] (Figure 1.3) was operated to solidify an Au₇₅Si₂₅ liquid into a supercooled state by rapid cooling rates of 10⁶ to 10¹⁰ K/s. In this pioneering literature, the metallic glass ribbons with 1~10 μm in thickness have been made. After several years, the ternary amorphous alloys of Au-Si-Ge and Pd-Si-X (X=Ag, Cu or Au) were fabricated by Chen and Turnbull [9, 10]. In the 1970s, Chen and Miller [11] synthesized an amorphous alloy ribbon with 2 mm in width, 50 μm in thickness, and several meters long, by using two rollers quenching process, as illustrated in Figure 1.4. This was the first time that amorphous alloys were synthesized in large length scales and in large amounts. Accordingly, continuous liquid quenching process has become the principle method to make amorphous alloy ribbons. In 1974, Chen [12] also demonstrated casting of millimeter diameter rods of Pd-Cu-Si amorphous alloys using a suction casting method. Afterward, in 1982–1984 [13, 14], using a boron oxide fluxing method, the Turnbull group at Harvard succeeded in synthesizing ~10 mm Pd–Ni–P BMGs at cooling rates well below 100 K/s. Turnbull and his coworkers indicated that these alloys had a reduced glass-transition temperature, $T_{rg} = T_g/T_L \approx 2/3$, similar to silicate glasses. Here, T_g is the glass-transition temperature (in K) and T_L is the alloy melting temperature.

Over the past two decades, the Inoue's group in Tohoku University of Japan carried out

the systematic studies of glass forming ability in a variety of multicomponent alloys using variable cooling rates [15, 16]. In 1991, the Inoue's group cast fully glassy $\text{La}_{55}\text{Al}_{25}\text{Ni}_{10}\text{Cu}_{10}$ with a critical thickness of 9 mm by using cooling Cu molds [15]. The next year, they also developed the $\text{Mg}_{65}\text{Cu}_{25}\text{Y}_{10}$ BMG with a diameter of 7 mm [16]. Meanwhile, the same group reported a family of Zr-Al-Ni-Cu based metallic glassy alloys with a high glass forming ability (GFA) and the supercooled liquid region in these alloys was extended to 127 K. Besides, $\text{Zr}_{65}\text{Al}_{7.5}\text{Ni}_{10}\text{Cu}_{17.5}$ amorphous alloy was seized of the largest diameter (~ 15 mm) among this family [17]. On the same year, Peker and Johnson discovered the first commercial $\text{Zr}_{41.2}\text{Ti}_{13.8}\text{Cu}_{12.5}\text{Ni}_{10}\text{Be}_{22.5}$ BMG alloy, also called as Vitreloy 1 (Vit 1), with a critical thickness of up to 12.6 mm [18]. In 1997, the Inoue's group re-investigated the first developed of $\text{Pd}_{40}\text{Ni}_{40}\text{P}_{20}$ BMG, and they discovered that the critical diameter increases from 5 mm up to 72 mm when 30% of nickel are replaced by copper [19]. However, Ma et al. [20] synthesized the Mg-based BMG with inch-diameter successfully in 2005, bringing on a significant progress on applications of Mg-based BMGs in all kinds of fields. During the past decade, a considerable number of papers appearing on amorphous alloys have been appeared. The list of the familiar amorphous alloys and BMG systems is shown in Table 1.2 [21], and the critical casting diameter of metallic glasses over the years are illustrated in Figure 1.5 [22].

1-3 The development of Zr-based thin film metallic glass (TFMG)

As mentioned above, it has been found that amorphization of metallic materials might result in a unique set of properties. That is why they have been under emphatic research from 1970s [23, 24] to present. The techniques available for obtaining amorphous alloys can be classified into two main types: metallurgical (melt quenching, melt casting, mechanical alloying, etc.) and microtechnological (deposition by sputtering or evaporation, solid-state

reactions, ion beam mixing, layer-by-layer deposition). Among them, thermal evaporation in high vacuum [25-27] and ion-magnetron sputtering [28] are widely used for deposition of thin films of amorphous alloys. In 1988, Minnigerode [25, 26] and his coworkers investigated the synthesis of Zr-Cu and Co-Cu thin films of amorphous alloys by means of co-condensation onto sapphire substrates by electron-beam evaporation. The structure of as-deposited thin films depends not only on the temperature of substrate, but also on other deposition parameters, such as working pressure, working distance, adatom mobility, etc.

Generally, thin films of amorphous alloys are also called as thin film metallic glasses (TFMGs), which can be synthesized by many physical vapor deposition processes. Two of most common methods to prepare TFMG specimens are sputtering and evaporation [29-31]. Subsequently, in 1996, Dudonis's group [32] studied the Zr_xCu_{1-x} amorphous films deposited by magnetron sputtering in relatively high vacuum. Various compositions of metal alloy Zr_xCu_{1-x} ($x = 0-1$) coatings were first established by simultaneous Zr and Cu magnetron deposition. By way of co-sputtering, amorphous Zr_xCu_{1-x} thin films can be obtained in relatively high vacuum (argon pressure, $p \leq 3 \times 10^{-2}$ Pa). After that, the Zr-based thin films were further studied [33] and applied in advanced micro-electro-mechanical-systems (MEMS) [34]. Based on the character of softening in a certain temperature range, called the supercooled liquid region, metallic glasses can be easily formed into a 3D shape and applied in advanced MEMS fields [35]. Professor Shimokohbe and his group members in Japan [34, 36] have fabricated Pd-based and Zr-based TFMGs by way of RF-magnetron sputtering system around 2000s. Although the bulk metallic glasses (BMGs) have been widely studied, little is known about applications of amorphous thin films for MEMS. Compared with conventional MEMS materials, TFMGs have the following advantages:

- (1) TFMGs soften and show viscous flow in the supercooled liquid region, which

makes them be easily formed into a 3D shape.

- (2) TFMGs are homogeneous and isotropic materials [37]. In consequence of their mechanical isotropy, structural homogeneity, and absence of crystalline defects such as lattice defects, grain boundaries, segregation, etc., TFMGs are assumed to have no size effect.
- (3) TFMGs are a kind of amorphous alloys in which their physical properties can be adjusted by changing their compositions and contents as well as by precipitation of nanoscale particles. For these reasons, TFMGs are considered to be practical materials for MEMS.

1-4 Motivation

BMGs exhibit many exceptional advantages for engineering applications, such as high strength, good corrosion resistance, easy shaping or forming ability, etc. Based on these unique properties, metallic glasses have recently been extended their research and application in MEMS. Despite of having these excellent properties, BMGs might be difficult to be made into micro- or nano-scale components in MEMS. The thin-film technique for MEMS has been employed in fabricating metallic glasses since 1980s. It supplied another way to solve the problems in applications of metallic glasses. As we know, however, the brittle nature of metallic glasses in the bulk and thin film forms inevitably imposes limitation and restricts the wide application of BMGs and TFMGs. Most amorphous alloys showed a very limited plastic strain [38-45] under mechanical testing at room temperature, except for some with particular compositions [46-48]. In order to improve the poor plastic property of amorphous alloys, there are many concepts proposed and discussed. For instance, Schroers and Johnson [49] reported that the Pt-based BMGs with higher Poisson ratios exhibit the ductility (plastic strain >20%) under both bending and unconfined compression loading. Moreover, Liu et al. [50]

mentioned that super plasticity (>160%) is achieved at room temperature in ZrCuNiAl synthesized through the appropriate choice of its composition by controlling elastic moduli. Likewise, Du et al. [51] used the computational-thermodynamic approach to calculate the two-glassy-phases composition of Zr-based BMG with remarkable plastic strain (>30%) at room temperature.

Composite concept might be another idea to solve this dilemma. In order to manufacture the bulk metallic glass composites (BMGCs), the approaches are classified into two categories: the intrinsic and extrinsic methods. For the intrinsic method, the in situ process and heat treatment process are two kinds of ways in common uses. Adding reinforcements into the BMGs or TFMGs is extensively used to manufacture composites in the extrinsic method.

The development of metal matrix composites is aimed primarily at improvements in room-temperature toughness [52] and in case of high-temperature strength [53], and there are, as well, examples of superplasticity developed in laminated composites [54]. As a result of advantages of thin-film processes, the composite or multilayer structure can be obtained with ease. With respect to these developments, it is particularly interesting to note that some nanocomposites and laminated thin films, i.e., composites containing components at the nanophase level of microstructure, have been studied. Recently, the suppression of shear bands in metallic glasses loaded at room temperature has been reported in crystalline/amorphous multilayers with the amorphous layer thickness less than 10 nm or in small scale (<100 nm) monolithic metallic glasses [55, 56]. The special movement behavior of the active dislocations in the nanocrystalline layers contributes mainly the attainment of co-deformation behavior [56]. However, for crystalline/amorphous multi-layers with more than 100 nm thick amorphous layer, no ductility in the glass layer has been observed due to

the formation of principal shear bands. For bulk metallic glass composites, large compressive plasticity [57, 58] and tensile ductility [59, 60] have been explored by matching the length scale of glassy phase with the “plastic zone” size, providing an opportunity to pursue the matched mechanical properties between amorphous/crystalline layers by tailoring their microstructural scale.

Recently ten years, several studies have revealed that metallic amorphous/crystalline nanolayered composites (MACNCs) have the capacity of simultaneously sustaining large plasticity and high strength at room temperature, making MACNCs promising in making nano- or micro-scaled devices, which are pervasive in modern industries [55, 56, 61]. For MACNCs, to form small-dimension devices with complex shapes, superplastic forming at low or even room temperature has been commonly accepted as one of the most feasible as well as economic methods. This fact makes it of great interest to explore the possibility of MACNCs to sustain intrinsically superplastic-like flow at room temperature.

An inspired fact is that some amorphous and nanocrystalline materials have inherently the capacity of superplastic-like deformation behavior under uniaxial compression [50, 62, 63]. From mechanical viewpoints, two factors beneficial to obtain the superplastic-like deformation of MACNCs are suggested: (a) matched plastic deformation capacity between nanoscaled amorphous and crystalline layers, and (b) perfect strain compatibility at amorphous/crystalline interfaces. Here, the strain compatibility is not a problem for the amorphous/crystalline interfaces owing to their positive roles as high-capacity sinks for dislocations, by which unique inelastic shear (slip) transfer properties are caused [55, 56]. So, how to achieve the matched plastic deformation capacity between nanoscaled amorphous and crystalline layers becomes the crucial point to obtain homogeneous deformation for MACNCs.

In this study, the deformation behaviors of multilayer (amorphous/nanocrystalline) micropillars are studied by uniaxial microcompression tests at room temperature. The nanocrystalline layer to be coupled with the amorphous layer can be of either face-centered cubic (FCC), hexagonal close-packed (HCP) or body-centered cubic (BCC) in crystal structure. The crystalline layers with nanocrystalline grains have two functions: one is to produce the unique plastic shear (slip or twinning) transfer at the amorphous-crystal interface; the other is to suppress local stress concentration due to paucity of dislocation pileups or twinning operations. The crystalline layers appear to be able to offer positive influence in enhancing the mechanical performance of the brittle metallic glass. In addition, deformation behaviors between amorphous/nanocrystalline interfaces are also explored in this study. Metallic amorphous/crystalline nanolayered micropillars are chosen to systematically investigate the effect of modulating layer thickness on their deformation behavior.

Chapter 2 Background and literature review

2-1 Manufacture methods of amorphous alloys

A lot of methods about fabricating amorphous alloys have been developed in the past twenty years. In terms of different cooling rates, these methods can be classified into following three groups: (1) cooling the gaseous state to the solid state: sputtering and evaporation in high vacuum; (2) cooling the liquid state to the solid state: splat quenching method, single or two-roller quenching process, spray forming process, casting method by a conventional metallic mold, high pressure die casting method and so on; (3) transforming the solid state to another solid state: ion beam mixing, mechanical alloying (MA) and accumulative roll bonding (ARB) [8].

2-1-1 Cooling the gaseous state to the solid state

The amorphous alloys can be produced by depositing the gaseous alloy or metal elements onto a cool substrate with a relatively high cooling rate of 10^{10} - 10^{12} K/s. The sputtering and vacuum evaporation [64], as shown in Figure 2.1 [65], are two kinds of processes that belong to this method.

For the sputtering process, a high voltage is added on two electrodes to create an electronic field under a gas (nitrogen or argon) environment. Then the electrons are emitted from the cathode and accelerated in the electronic field. These electrons will excite the gas molecules into positive gas ions and electrons. Once the gas ions impact an alloy or metal target, the alloy or metal atoms will deposit on the substrate and form an amorphous film. On

the other hand, it is necessary for the vacuum evaporation process to use the heating and vacuum systems. The alloy or element vapors which are emitted from the heating target are also deposited on the substrate to form the amorphous film. In order to reach a sufficient cooling rate, liquid nitrogen or helium is usually used. In 1954, Buckel [66] fabricated amorphous films of pure metals, such as Ga and Bi, by thermal evaporation onto the substrate maintained at the liquid helium temperature with the fast cooling rate above 10^{10} K/s. After that, in 1986, Cotts et al. [67] successfully synthesized the Ni-Zr multilayer thin films by the magnetron sputter method, and observed the amorphization of crystalline metallic thin film by differential scanning calorimetry (DSC). The reactions of cooling gaseous state to solid state to form metallic glasses are well known as gas deposition techniques. The multi-component monolayer TFMGs can be fabricated by two methods: (1) co-sputter deposition process [32], and (2) alloy sputter deposition process [34].

2-1-2 Cooling the liquid state to the solid state

Liquid quenching with a cooling rate of $10^3 - 10^8$ K/s is used extensively in fabricating the amorphous alloys. Amorphous alloys can be made into all kinds of forms by using this method, including the splat quenching, two rollers quenching, melt spinning, planar flow casting, metallic mold casting, high-pressure die casting and spray forming, etc [68-71]. The first step in this method is to melt or to atomize the alloys, and then quench them onto a low temperature mold or substrate with high thermal conductivity. Through this method (gun quenching), the first amorphous metal Au-Si was prepared in 1960 [7].

2-1-3 Transforming the solid state to another solid state

The cooling rate is not necessary to be critical while using this method, and the

processes include severe plastic deformation, the solid-state reaction, particle bombardment, and solid-state interdiffusion, etc.

The principle of severe plastic deformation is to refine the grain size of the alloy by creating a large amount of plastic deformation. Once the grain size is small enough, the structure of the crystalline alloy is transformed into the amorphous state. There are many ways to carry out a large amount of plastic deformation, such as cyclic extrusion or cyclic compression, torsion straining under high pressure, equal channel angular pressing (ECAP), mechanical alloying (MA), and accumulative roll bonding (ARB) [72-77].

When high-energy electrons or heavy ions such as N^+ impact an alloy surface, the atoms of alloy surface will rearrange to reach the amorphous state. This is the basic concept of the particle bombardment method. Various processes used for this method include neutron and ion particle bombardment irradiation, electron beam radiation, ion implantation, and ion beam mixing.

However, the solid-state interdiffusion reaction method is different from the two methods mentioned above. As two different metal layers or thin films are treated with an appropriate heat treatment process, the atoms between two metal layers will diffuse to each other and make an amorphous layer, provided that the temperature is not high enough to induce any intermetallic compound.

2-2 The characters and forming conditions of amorphous alloys

2-2-1 Glass forming ability (GFA)

Glass forming ability (GFA) is defined as the ease of glass forming. The high GFA of cast amorphous alloys means a larger size of an amorphous alloy can be fabricated easily under a lower cooling rate. A lot of studies have been made on the factors influencing the GFA. Furthermore, these researcher noted that GFA is related to the thermal properties [78-80], atomic sizes [81-83], and electronic configurations [84-87] of the amorphous alloy. Among these parameters, the thermal properties are applied extensively due to two advantages. One is that the thermal information of amorphous alloy is unique and can be obtained easily and quickly. Another advantage is that these data can be transformed to an index by simple calculation.

2-2-2 Supercooled liquid region (SCLR)

With regard to estimating GFA of metallic glasses, the well-known index is supercooled liquid region, also defined as ΔT_x . Based on the differential scanning calorimeter (DSC) trace of a metallic glass during the heating process, two reactions before the alloy melts were observed, as shown in Figure 2.2 [88]. One of the reactions is the glass transition reaction with an endothermic phenomenon, and the other is the crystallization reaction with an exothermic phenomenon. Therefore, the supercooled liquid region is defined by the difference between glass transition temperature (T_g) and crystallization temperature (T_x). And it can be expressed as

$$\Delta T_x = T_x - T_g. \quad (2-1)$$

When the metallic glasses are heated over T_g , they change into the supercooled liquid state. The supercooled liquid crystallizes, when the temperature exceeds T_x , and a metallic glass

becomes a solid of the crystal phase. The phase transition at T_g is reversible and that at T_x is irreversible.

Not only does this temperature region (ΔT_x) represent the thermal stability of amorphous alloy but also the GFA of this amorphous alloy. The relationship of critical cooling rate (R_c) and supercooled liquid region (ΔT_x) is presented in [Figure 2.3 \[6\]](#).

2-2-3 The empirical rules for forming amorphous alloys

After the first discovery of amorphous alloys around 1960s, various methods developed to produce bulk metallic glasses were mostly empirical in nature, but researchers gradually began to understand that the correct choices of elemental constituents would lead to amorphous alloys exhibiting critical cooling rates as slow as 1-100 K/s. The Inoue's group had developed series of amorphous alloy systems with high GFA in the past decade, and they summarized and proposed three simple empirical rules for the alloy design of BMGs with high GFA [\[6, 89-91\]](#). The three empirical rules are presented as below:

- (1) Multicomponent consisting of more than three elements.
- (2) Significantly different atomic size mismatches exceeding 12% among the main three constituent elements.
- (3) Negative heats of mixing among the main elements.

For the alloy system with more than three main elements, the difference of atomic sizes causes a retardation of atoms moving when quenching this melt into a solid state. Consequently, the atoms of the solid phase exhibit a short-range order arrangement, which leads to high dense random packing. Hence if there are three different elements mixed

together and the difference in atomic size is large, the GFA of amorphous alloys will be improved with increasing categories of main elements in the multi-component system. Furthermore, the atomic structure development also plays an important role for the mechanism of amorphous phase forming. The difference in atomic size ratios above 15% will induce a dense random packing in the supercooled region. The difficulty of atomic rearrangements attributes the formation of an amorphous phase and impedes the formation of a crystalline alloy.

According to the thermodynamic point of view, it starts from the generally known relation of $\Delta G = \Delta H_{mix} - T\Delta S_{mix}$. The heat of mixing ΔH_{mix} is regarded as the ability of atomic bonding between two atoms in an alloy system. Larger negative heat of mixing refers to the fact that the bonding ability of the same atoms is very weak, but the bonding ability for distinct atoms is strong. When the liquid alloy is solidified with a larger negative heat of mixing, the distinct atoms tend to bond together and arrange in a random way. Accordingly, the amorphous alloys form easily when the distinct main atoms have the larger negative heat of mixing. Based on Miedma's macroscopic model, the summary of ternary amorphous systems and mixing enthalpy values of three binary subsystems were obtained, as listed in Table 2.1 [92].

Besides what mentioned above, the new amorphous alloys following these empirical rules must have a higher liquid/solid interfacial energy, leading to the suppression of nucleation of crystalline phase as well as the difficulty of atomic rearrangements. The latter contributes the low atomic diffusivity and high viscosity, leading to the difficulty of growing a crystalline phase. These mechanisms for the reduced instability and the formation of bulk glassy alloys are shown in Figure 2.4 [6], containing three characteristics for a particular liquid structure.

2-3 Principle of physical vapor deposition

2-3-1 Introduction of sputtering

The physical sputtering process involves the physical vaporization of atoms from a surface by momentum transfer from bombarding atomic-sized particles. The energetic particles are usually ions of gaseous material accelerated in an electric field. Highly energetic ions and neutrals bombard a negatively biased target which can cause ejection of surface and near-surface target atoms through momentum transfer. Typically the use of the term, sputter deposition, only indicates that a surface being sputtered is the source of the deposited material. In some cases, the sputtering configuration may be indicated (e.g., ion beam sputtering, magnetron sputtering, RF sputtering, etc.). In general, sputter deposition can be operated in: (1) a good vacuum ($<10^{-5}$ torr) using ion beams; (2) a low pressure gas environment where sputtered particles are transported from target to the substrate without gas phase collisions using a plasma as the ion source of ions. Sputtering occurs whenever any particle strikes a surface with enough energy to dislodge an atom from surface. The sputtering yield is the ratio of atoms sputtered to the number of high energy incident particles [93] and it depends on the mass of the bombarding particle as well as its energy.

The bombarding particles can physically penetrate into the surface region while the collision effects can be felt into the near-face region. Figure 2.5 [93] shows the processes that occur at the surface region and in ten near-surface region of the bombarded surface. Most of the transferred energy (>95 %) appear as heat in the surface region and near-surface region. Some of the bombarding particles are reflected as high energy neutrals and some are implanted into the surface. When an atomic sized energetic particle impinges on a surface, the particle bombardment effects can be classified as [93]:

- (1) Prompt effects ($<10^{-12}$ s) – e.g., lattice collisions, physical sputtering, reflection from the surface.
- (2) Cooling effects ($>10^{-12}$ s to 10^{-10} s) – e.g., thermal spikes along collision cascades.
- (3) Delayed effects ($>10^{-10}$ s to years) – e.g., diffusion, strain-induced diffusion and segregation.
- (4) Persistent effects – e.g., gas incorporation compressive stress due to recoil implantation.

2-3-2 DC and RF sputtering

In DC (direct current) diode sputtering, the electrons that are ejected from cathode are accelerated away from the cathode and are not efficiently used for sustaining the discharge. By the suitable application of a magnetic field [93], the electrons can be deflected to stay near the target surface and by an appropriate arrangement of the magnets. The high flux of electrons creates a high density plasma from which ions can be extracted to sputter the target material producing a magnetron sputtering configuration. However, the real difference between the DC and RF (radio frequency) sputtering is that, for RF sputtering, the power supply is operated at high frequencies. Unlike DC sputtering, RF sputtering can be used to sputter electrically insulating materials despite the sputter yield is low. A chief disadvantage in RF sputtering of dielectric targets, is that most electrically insulating materials have poor thermal conductivity, high coefficient of thermal expansion, and brittle nature.

The major advantage for DC or RF magnetron sputtering configuration is that a dense plasma can be formed near the cathode at low pressures so that ions can be accelerated from plasma to cathode without loss of energy due to physical and charge-exchange collisions. This allows a high sputtering rate with a lower potential on the target than with the DC diode

configuration.

2-3-3 Nucleation and growth of sputter-deposited films

Film growth by the continuous nucleation of depositing atoms on previously deposited and the surface is continually being covered under newly depositing material. The thin film growth or nucleation mode determines many as-deposited film properties such as thin film density, surface morphology and grain size. There are several important aspects of thin film growth, as listed below [93]:

- (1) Substrate surface roughness – initially and as the thin film develops
- (2) Surface temperature – initially and as the thin film grows
- (3) Adatom surface mobility
- (4) Geometrical shadowing effects (angle-of-incidence effects)
- (5) Reaction and mass transport during deposition such as segregation effects and void formation.

Generally, as thin film grows, the surface roughness increases due to some features or crystallographic planes grow faster than others. When the adatom flux onto the substrate exceeds the flux of adatoms leaving from the substrate surface, film nucleation and growth occur. The nucleation process is controlled by adsorption energy between the adatoms and substrate or growing film, the surface diffusion energy required to transfer an adatom to an adjacent adsorption site as well as the binding energy between deposition atoms [94]. In reality, the migration of adatoms is not random and is dependent on the substrate crystallographic directions and surface topography as well as other external conditions such as temperature. This may lead to very fine grained polycrystalline films. Basically, film

formations have three basic growth modes, island (or Volmer-Weber) mode, layer (or Frank-Vander Merwe) mode, and Stranski-Krastanov mode [95]. These are illustrated schematically in Figure 2.6 [95] and described below respectively.

(1) Island (or Volmer-Weber) mode:

Island growth occurs when the smallest stable cluster nucleates on the substrate and grows in three dimensions to form an island. This happens when atoms or molecules in the deposit are more strongly bound to each other than to the substrate. Many systems of metals on insulators, alkali halide crystals, graphic, and mica substrates are of this growth mode.

(2) Layer (or Frank-Vander Merwe) mode:

Two-dimensional layer-by-layer growth occurs when the binding energy between coating atoms to substrate atoms is stronger than that between coating atoms. The first arriving atoms will condense as a single monolayer and there is no energy barrier for nucleation. This growth mode occurs for heteroepitaxial thin film growth in semiconductor-semiconductor systems and some metal-metal systems.

(3) Stranski-Krastanov mode:

The Stranski-Krastanov film growth mode is essentially a combination of the layer-by-layer and island growth modes.

2-3-4 Amorphous film growth

Amorphous materials are those that have no detectable crystal structure. Amorphous films can be fabricated by [93]:

(1) Deposition of a natural glassy material such as a glass composition.

- (2) Deposition at low temperatures where the adatoms do not have enough mobility to form a crystalline structure.
- (3) Ion bombardment of high modulus materials during deposition.
- (4) Deposition of materials some of whose bonds are partially saturated by hydrogen such as a-Si:H, a-C:H and a-B:H [96, 97].
- (5) Sputter deposition of complex metal alloys.
- (6) Ion bombardment of films after deposition.

2-4 Properties of thin film metallic glasses

2-4-1 Thermal properties

TFMGs have mechanical isotropy and structural homogeneity, and can be assumed to lack for size effect and defects. Moreover, the advantage of TFMGs as MEMS materials that they show the viscous flow in SCLR makes them easy to form 3D structures. To use the TFMGs as MEMS materials or make 3D microstructures of TFMGs, the micro-forming process has to be executed in SCLR. Thus one of the most important properties for TFMGs is thermal stability. SCLR and thermal properties of TFMGs were measured by differential scanning calorimetry (DSC). From the thermography trace of DSC result (Figures 2.7 and 2.8) [98], the glass transition temperature (T_g), crystallization temperature (T_x) and SCLR ($\Delta T_x = T_x - T_g$) can be determined. For the Pd-TFMG, its T_g , T_x and ΔT_x are 637 K, 669 K and 32 K; while for Zr-TFMGs, its T_g , T_x and ΔT_x are 643 K, 713 K and 70 K, respectively. Zr-TFMG exhibits an endothermic reaction, a slope change, due to glass transition at about 643 K and an exothermic reaction due to crystallization at about 713 K, as shown in Figure 2.9 [98].

From another point of view, time-temperature-transformation (TTT) diagrams, which

represent thermal stability of the TFMGs, were also conducted using DSC. From two typical TTT diagrams of Zr-TFMGs, as shown in [Figures 2.9 and 2.10 \[98\]](#), the time till the onset of crystallization and amorphization can be observed. In addition, the permissible interval of heating time and temperature of TFMGs can also be ascertained for the micro-forming process and annealing heat treatment.

2-4-2 Mechanical properties

Due to the dense packing structure and irregular rearrangement of atoms, when the stress is applied, the amorphous alloys only allow small displacements of atoms to resist deformation without the invoke of dislocations as for the case of crystalline metals. Therefore, the amorphous alloys show higher tensile strengths than the traditional crystalline alloys, as shown in [Figure 2.11 \[6\]](#).

In terms of a crystalline alloy, the alloy starts plastic deformation when the resolved shear stress is greater than the critical resolved shear stress on a particular plane (slip plane). Simultaneously, a dislocation is formed and begins moving along the slip direction on a slip plane. It is well known that the mechanical properties of crystalline materials strongly depend on their crystal and electronic structures. Nevertheless, amorphous alloys lack this kind of long-range-order structure as present in crystalline alloys. In other words, there is no slip system in amorphous alloys, and the plastic deformation of amorphous alloys do not use slip systems. Because of their disordered atomic structure, amorphous metals have difference in deformation mechanisms compared with polycrystalline metals. The chief difference in mechanical performances, such as strength and ductility, which vary with the chemical compositions of metallic glasses, indicates the existence of an intrinsic correlation between the mechanical properties and the atomic and electronic structures of metallic glasses.

Within the amorphous short-range-order structure, there are lots of small spaces among atoms, as shown in [Figure 2.12](#), which are called free volumes. Historically, several theories have been reported to describe the heterogeneous plasticity of metallic glasses. The plastic flow in amorphous alloy is considered as a diffusion-like process involving the stress-induced self-assembled of smaller unit of plasticity that are called flow defects or shear transformation zones (STZs) [\[99, 100\]](#). STZs are the fundamental unit of plasticity in a form of a small cluster of randomly close-packed atoms. These flow defects or STZs are associated with about 10~50 atoms in open spaces or free volume sites, which are distributed all over the amorphous structure. [Figure 2.13](#) illustrates the STZ deformation in two-dimensional space. Consequently, the dominated physical mechanisms behind glass structure and deformation are generally localized to this mere fine scale. In other words, it is usually assumed that the amount and distribution of the free volume dominate the plastic deformation of amorphous alloys.

Moreover, the moving of STZ is always accompanied by the releasing of adiabatic heat near the STZ [\[101\]](#). If more and more STZs start moving along a shear plane, the temperature around the shear plane will be risen due to the huge adiabatic heat. The temperature can generally reach the glass transition temperature at least, and after that a fluid region or fluid layer will be formed in the shear plane, as [Figure 2.14](#) shows. This fluid region offers more free volume sites to STZs, and makes the plastic deformation of amorphous alloy easier.

The mechanical properties of TFMGs are critical not only for the design of MEMS devices, but also for the predictions of their performance and life. In 2001, Liu et al. [\[29\]](#) pointed out the technique to examine the Young's modulus of TFMGs. For the Young's modulus measurement, cantilever microbeams of Pd-TFMG were fabricated using the surface micromachining process, as shown in [Figure 2.15](#) [\[29\]](#). The following equation was used to

calculate the Young's modulus from the bending test results:

$$E = \frac{4Px^3}{ywt^3}, \quad (2-2)$$

where E is Young's modulus, P the applied load, y the deflection, x the effective length from the indenter tip to the fixed point of the cantilever, w the width, and t is the thickness of the cantilever. The measured Young's modulus of a Pd-TFMG is 69.7 GPa. In 2005, the same group investigated mechanical properties of the small dimensional Pd₇₆Cu₇Si₁₇ TFMG, both as-deposited and annealed at SCLR near T_g by using bending of the free-standing microbeams. A set of microbeams with different annealing time, as deposited (sample 1), annealed for 90 s (sample 2) and 480 s (sample 3) near T_g (640 K) were chosen for static bending using a nanoindenter to study the deformation behavior of the Pd-TFMGs. [Figure 2.16 \[102\]](#) displays the observations of microbeam surface at the fixed end after bending test. For samples 1 and 2, clear shear bands were formed at surface ([Figures 2.16\(a\) and 2.16\(b\)](#)), while for sample 3, there are no any visible shear bands at the microbeam surface ([Figure 2.16\(c\)](#)). Some secondary shear bands along another shear plane occurred, as indicated by arrows in [Figures 2.16\(a\) and 2.16\(b\)](#). The author indicates that optimal mechanical properties of the Pd-TFMG for MEMS application can be obtained by carefully controlling of annealing time at SCLR.

2-4-3 Electrical Properties

The electrical properties of TFMG are also very important for applying them to microform in three-dimensional MEMS devices. As the possible MEMS devices of the TFMGs could be used not only as a conductor but also as an insulator. The electrical resistivity of Pd-TFMG was obtained by the conventional four-point probe method. [Figure](#)

2.17 [29] shows the resistivity-annealing temperature curve of Pd-TFMG. The obvious drop of resistivity may be caused due to the crystallization by heating above T_x . The typical change in the electrical resistance with increasing annealing temperature is shown in Figure 2.18 [29] for $Zr_{60}Al_{15}Ni_{25}$. The electrical resistance around room temperature decreases with increasing annealing temperature.

2-4-4 Magnetic properties

Permeability stands for the soft magnetic property of the material. Because the greater part of the magnetic materials is the pieces form, such as silicon steel lamination and wave filter, it is easy to fabricate the amorphous ribbons by melt spinning. In addition, some amorphous alloys exhibit great permeability and minimum magnetic energy loss. Hence, the application of this kind of magnetic amorphous alloy has been very wide [103]. The typical magnetic amorphous alloy systems can be divided into two categories: TM-M and TM-TM (TM: Fe, Co, Ni, Zr, Hf, etc; M: B, C, Si, P, Ge, etc).

2-4-5 Chemical properties

The very high corrosion resistance has been observed in some amorphous alloys as a result of the homogeneous single-phased structure which is lack of grain boundaries, dislocations, and the other crystal defects. Furthermore, one can improve the corrosion resistance of amorphous alloys by adding some kinds of corrosive solute. For instance, the corrosion resistance of Zr-Al-Ni-Cu amorphous alloy increases as adding the corrosive solute, such as Nb, Ta, Ti, and Cr [104]. The other amorphous alloys, such as the Pd-based as well as Fe-based [105] amorphous alloys, also have the highest corrosion resistance and they can serve as practical corrosion resistance materials.

2-5 Characterization of microscale mechanical properties

2-5-1 Introduction to microcompression tests

Microcompression tests were firstly been developed by Uchic et al. [106] in 2004. Their group first discovered the methodology to investigate the size effect in virtually any bulk inorganic material, using focus ion beam (FIB) machine for sample preparation. The microcompression tests were conducted with the MTS nanoindenter XP equipped with a flat-end Berkovich indenter which was machined by FIB. Compared with traditional compression tests, microcompression tests have following advantages: (1) the microcompression samples (denoted as micropillars) remain attached to the substrate and easy to handle; (2) the micropillars are loaded with the commercial nanoindentation system; (3) FIB can be scripted and automated to manufacture the micropillars. According to the advantages as described above, FIB and nanoindentation system have been widely applied to explore the size-scale effects on mechanical properties of metals or alloys. The related researches and results are discussed in following sections.

2-5-2 Parameters of microcompression tests

The factors that may affect the accuracy of microcompression tests have been discussed in 2006 by Zhang et al. [107]. They have made recommendations regarding allowable fillet radius (r_c), pillar aspect ratio (α), tapered angle (θ) and misalignment of the system, using the two-dimensional and three-dimensional finite element modeling.

First of all, the important geometric factor, fillet radius r_c , the curvature at the bottom of the pillar connecting to the base (Figure 2.19) [107]. Compared with input stress, 6% of flow

stress error from microcompression would cause by radius/pillar radius ratio $r_c/r = 1$. Based on the results analyzed by finite element analysis, the larger the fillet size (with respect to the post radius), the greater the error. When the fillet radius ratio is less than 0.5, the output curves are very close (within 3%) to the input data. This suggests the overestimate of flow stress of the material in the plastic range, as shown in [Figure 2.20 \[107\]](#). Another issue should be addressed is the distribution of the von Mises stresses in the micropillar and the base. The results demonstrate that with increase r_c/r , the stress concentration at the fillet is alleviated. Excessive stress concentrations may result in localized pillar failure prior to general yielding. Thus, the choice of fillet radius for an experiment represents a compromise between the need to accurately observe material behavior in the plastic range (requiring small r_c/r) and avoid localized failure at the pillar root (which requires large r_c/r). In the two-dimensional simulations, it suggest that a choice of r_c/r in the range of 0.2-0.5 represents a good compromise. In practice, the fillet size can be well controlled by the FIB or micro-machining parameters. Therefore, it is realistic to use microcompression to probe the mechanical properties of materials.

Secondly, pillar aspect ratio α is another important parameter that may affect the accuracy of measurement. For the aspect ratio $\alpha = 2$, even with the largest fillet radius/post radius ratio, i.e., $r_c/r = 1$, the error in flow stress from the microcompression test is less than 6%. The aspect ratio of the pillars has a relatively small effect on the output flow stress curves when it is larger than 2. Nevertheless, smaller α would lead to larger output flow. Owing to the constraint result from the pillar base and the output strain hardening of the pillar during the microcompression test, these two reasons will result in output flow tp deviate from input value. However, the increase of the aspect ratio could increase the effects of bucking, and causes the decreasing of the output stress. The reason for that is if pillars are not at the same stress axis as the tip is, the friction between the flattened indenter and pillar top should

be considered. Interacting due to these two conflicting affects is shown in [Figure 2.21 \[107\]](#), stress drop could be observed at the stress-strain curve. The result indicates that the pillar has been subjected to severe buckling which affects the corresponding stress-strain curve of the pillar. Furthermore, [Figure 2.21\(c\) \[107\]](#) shows the input and output stress-strain curves for pillar aspect ratio in the range of 2~5. This suggests that the plastic buckling is suppressed by the friction when aspect ratio is less than 5. Thus, from the both two-dimensional and three-dimensional simulation results, Zhang et al. [\[107\]](#) recommended that the aspect ratio of pillars should be 2~3.

The third geometric factor that may have a significant effect on the accuracy of microcompression experiments is taper angle of the pillar. The amount of taper is defined by tangent of the wall with respect to the axis, and often the radius of the top portion is smaller than the bottom as a result of the micropillar fabrication using FIB or other micromachining processes. The effects of taper result in an overestimate of the elastic modulus. Due to the taper angle of $\sim 2.86^\circ$, the measured elastic modulus is obviously larger than the input data. [Figure 2.22 \[107\]](#) displays the contrast taper affects with different aspect ratios, though the small aspect ratio would cause overestimation. Therefore, it is of need to avoid the load drop and minimize the overestimate of the output stress. Besides, the small taper angle must be chosen.

Finally, the last important factor that might cause the primary deviation of the stress-strain curve and affect the accuracy of testing elastic region of microcompression is the effect of misalignment of the system. This alignment is the angle between the normal direction of the flattened indenter and the pillar axis. It gives rise to underestimate of the elastic modulus of the material. The measured elastic modulus decreases with increasing misalignment. The excessive misalignment may result in buckling of the pillar. From

three-dimensional simulation, the results demonstrate that even perfect alignment ($\theta = 0^\circ$) has 20% underestimate the elastic modulus. The elastic modulus should be at least 1.25 times that from microcompression tests. Hence the effect of misalignment significantly affects the accuracy of measuring mechanical properties.

2-5-3 Microscale mechanical properties on micropillars

A “size effect” can be defined as a significant change in material properties, such as mechanical, electrical, optical, magnetic properties, that is due to a change in intrinsic or extrinsic sizes. Intrinsic size effects arise as a result of initial microstructural constraints and specific size-dependent deformation behaviors, such as grain size or second phase precipitation. Extrinsic size effects are controlled by dimensional constraints or experimental initial and boundary conditions. These extrinsic constraints might be due to small sample size or due to small strained volume, where the dimensional constraint arises from the testing system. However, this intrinsic or extrinsic effect governs the mechanical properties and material deformation mechanism at all sample dimensions. In recent years, there has been great motivation to reduce the size of many mechanical systems to the micron and sub-micron scale by fabricating devices out of small size-scale materials. In 2004, Uchic et al. [106] have discovered the size effect of Ni, intermetallic alloy of Ni₃Al-1%Ta and Ni superalloy single crystal. The authors have developed a testing method to investigate the size-scale effects on deformation and strength by the traditional compression test to the micrometer scale. The stress-strain curves for Ni microcompression samples having diameters in the 20- to 40- μm range are similar to the bulk samples. Figure 2.23 shows a SEM of 5- μm -diameter microsample after testing, where the sample achieved about 19% strain during a rapid burst of deformation. Strain bursts are also observed for samples 10 μm in diameter while the strain is less than 1%. Figure 2.23(c) also shows a SEM image of

1- μm -diameter microsample after microcompression testing, where the top of the sample has completely sheared off during the rapid strain burst. This behavior is observed for both the 1- and 0.5- μm -diameter samples. After that, great deals of researches on sample size effect have been attracted to study widely.

In 2005, Greer et al. [108] observed the same phenomenon on microscale Au samples. The results of their uniaxial microcompression tests indicate a strong sample size effect: pillars made by both fabrication methods yielded at stresses that are much higher than the typical yield strength of bulk gold estimated at 30 MPa at 2% strain [109]. Moreover, the flow stresses for single-crystal pillars rapidly increase as their diameters are reduced below 1 μm . A series stress–strain curves for the various pillars fabricated by FIB are shown in Figure 2.24 [108]. The author and his co-workers claimed that the high strengths in microcompression results from an indication of dislocation starvation. Dislocations are believed to pass through the sample free surface and out of crystal before they have an opportunity to interact and multiply. Because of the deformed pillars without the contribution of dislocations, the strength will tend toward to theoretical strength. To confirm this explanation and to exhaust the artifact condition during the microsample preparation processes, Greer et al. [108] developed another notable result, an alternative fabrication method based on lithographic patterning and electroplating. Based on the results on microspecimen fabricated by both FIB milling and lithographic patterning and electroplating, they demonstrate that the strength increase is not artificial. Meanwhile, Volkert et al. [110] have also developed the similar sample size effects in submicron pillars and attributed their results to source-limited behavior in small volumes.

In 2006, Uchic et al. [111] clarified the microscale compressive behavior of $\text{Ni}_{76}\text{Al}_{24}$ alloys by means of microcompression tests. The events of strain burst were observed in the

stress-strain curves of microscale samples. The strain burst means that the strain (or displacement) takes place almost instantly and it is much similar to the so-called the pop-in effect for the nanoindentation compression tests, as shown in Figure 2.25 [111]. The stress-strain curve shows (Figure 2.25(a)) a number of discrete strain bursts that are separated by periods of nearly-elastic loading. Observation of the surface of the sample after testing shows clearly-identifiable slip-band formation (Fig. 2.25(b)), and the number of observable slip bands is approximately the same as the number of slip events. Similar research published in 2006 by Schuster et al. [112], the maximum yield strength of the microscale compressive properties of electrodeposited nanocrystalline Ni is 1498 MPa for the 20 μm diameter samples. The result of the Mo-10Al-4-Ni alloy was reported by Bei and co-workers in 2007 [113]. While tested in compression with a nanoindentation system, the pillars all yielded, regardless of size, at a critical resolved shear stress of 4.3 GPa, or $G/26$, where G is the shear modulus. This shear yield strength is in the range expected for the theoretical strength, $G/30$ to $G/10$.

Recent mechanical tests on microscale metallic glass pillars have revealed a certain degree of increase in yield strength with decreasing sample size [114-116]. In 2007, Lee et al. [115] have indicated that strength increase of Mg-based metallic glasses can be rationalized using the Weibull statistics for brittle materials, and the Weibull modulus of the Mg-based metallic glasses is estimated to be about 35. Their results also interpreted that the number of shear bands increased with increasing sample size and strain rates. However, despite the small volume of micropillars, the catastrophically localized principal shear banding has remained to be the fundamental deformation mode. Even though the metallic glassy pillars can sustain the straining up to 20% or above, the strain was carried predominantly by a few principal localized shear bands. The pillars show little overall uniform ductility at room temperature and are still quasi-brittle in nature.

The STZ model has been universally used to demonstrate the formation of shear bands (SBs) for many MG systems [117, 118]. The STZs and SBs can explain basically most MG deformation behavior, but might not be fully feasible for the recent findings of metallic glasses in very refined sample size. In the case of metallic glasses, the deformation can be divided into inhomogeneous and homogeneous deformation. Homogeneous deformation occurs typically near and above the glass transition temperature (T_g) [119]. A remarkable ductility can be observed when a BMG is deformed homogeneously in the supercooled liquid. For inhomogeneous deformation, it typically occurs at ambient temperature well below T_g and the deformation mode is dominated by localized shear band formation [120]. Many attempts have been made to assess the critical sample size below which shear band localization would disappear and the sample can deform homogeneously [56, 114-116, 121-125]. Based upon SEM observations of deformed pillar samples, the length scale necessary for homogeneous deformation has been claimed to be less than 100 nm [56, 121, 122]. MG sample sizes below this critical length scale would lead to no shear band formation. Volkert et al. [123] reported that the length scale at the transition from shear band localization to homogeneous deformation occurred in their 400 nm pillar. In comparison, Chen et al. [124] predicted 200 nm as the minimum length scale below which shear band would not form. Intrinsically strong size effects on deformation behaviors of metallic glass pillars have also been demonstrated by Chen et al. [125]. They found the different deformation behaviors while the pillar diameter decreasing from 640 nm to 70 nm. With the pillar diameter gradually decreasing, the deformation mode evolves from (i) 640 nm: highly localized and catastrophic shear banding to, (ii) 365 nm: initially nonlocalized deformation developing toward stop-and-go shear banding accompanied by softening, (iii) 100 nm: apparently homogeneous and banding-less deformation but with intermittent shear events, and eventually (iv) 70 nm: fully homogeneous and smooth plastic flow. [Figures 2.26 and 2.27](#)

show the stress and morphological evolutions of nanopillars with diameters of (i) 640 nm, (ii) 365 nm, (iii) 100 nm, and (iv) 70 nm, respectively, as functions of strain. On the other hand, Schuster et al. [126] and Dubach et al. [127] claimed there is no evidence of deformation mode transition at the pillar diameter as small as 200 nm. Wu et al. [128] also conducted in situ compression experiment using 150 nm-diameter pillar in TEM and concluded there was no size effect. Obviously, despite these research efforts, the question still remains as to whether there exists an inhomogeneous to homogeneous transition.

2-5-4 Microscale mechanical properties on multilayer structures

Recently, the research and development of advanced structural materials has focused on two major areas: nanocrystals and composites. Measuring and understanding the mechanical properties of nanolayered composites has been a recent area of active investigation. These materials are of technological interest due to their enhanced hardness [129] and tensile strength [130] as compared to the rule of mixtures values for their bulk phase counterparts. In 1999, Nieh et al. [55] developed a novel and free-standing nanocrystalline Cu/amorphous Cu_4Zr_3 laminate (Figure 2.28) by means of a sputter deposition method. The material possesses a very high yield and tensile strength while still retaining a reasonable tensile elongation (~4%). The true stress-strain curves for the Cu-Zr laminate are shown in Figure 2.29. For example, the yield and tensile strengths of the nanolaminate are 600 and 1120 MPa, respectively. These values are significantly higher than the yield and tensile strengths of nanocrystalline Cu, which are only 180 and 275 MPa, respectively. Moreover, after several years, Wang et al. [61] reported that nanocrystalline–amorphous nanolaminates exhibit a high flow tensile stress of 1.09 ± 0.02 GPa, a nearly elastic-perfectly plastic behavior without necking, and a tensile elongation to failure of $13.8 \pm 1.7\%$, which is six to eight times higher than that typically observed in conventional crystalline–crystalline nanolaminates (<2%) and

most other nanocrystalline materials. [Figures 2.30\(a\) and 2.30\(b\)](#) show the cross-sectional and planview TEM images of the as-deposited amorphous CuZr 5 nm/nanocrystalline Cu 35 nm intermixing multilayer nanostructures. The average grain size in the nanocrystalline layers is approximately equal to the individual layer thickness. [Figure 2.30\(c\)](#) shows room-temperature tensile true stress–strain curves of the nanocrystalline–amorphous nanolaminate, in comparison with those of the Cu/304 stainless steel crystalline multilayer, with an individual layer thickness of 25 nm and pure nanocrystalline Cu with an average grain size of 30 nm. [Figure 2.30\(d\)](#) displays the top-view of the gauge section after fracture for 5/35 nm Cu/Zu nanolaminate.

Meanwhile, the suppression of shear bands and homogeneous deformation in nanoscale metallic glasses was demonstrated by Donohue et al. [\[131\]](#) in 2007. Shear band formation in metallic glass can be suppressed by confining nanometer-scale glass layers between ultrafine crystalline layers. The effect is observed when the crystalline layers are sufficiently stiff to produce a large elastic restoring force to counteract the nucleation of the surface steps required for extensive shear on the bands in the glass. The crystalline layers are sufficiently thin so that the dislocation pileups that create local stress concentrations are suppressed and the crystalline layers co-deform with the high strength amorphous film. [Figure 2.31\(a\)](#) shows the bright-field image of as-deposited 100/100 nm Cu/*a*-PdSi multilayer thin films. Cross-sectional TEM imaging of the bent sample shows that the layered structure remained intact even though the sample was deformed extensively, as shown in [Figure 2.31\(b\)](#). The model of atomic scale shear transformation zones has also been demonstrated in this paper. Schematic illustration of slip transmission across nanometer-scale crystalline (c)/amorphous (a)/crystalline(c) sandwich structures is depicted in [Figure 2.32](#) [\[131\]](#). Since dislocation pileups are suppressed in nanolayers, slip occurs via glide of single dislocations on closely spaced glide planes that deposit uniform arrays of interface dislocations. Following the

template of the dislocations deposited at the interface, atomic-scale shear transformation zones are nucleated in the amorphous layer resulting in homogeneous plastic flow without formation of shear bands.

In addition to amorphous/crystalline multilayer structure, the micromechanical response of amorphous/amorphous multilayer films has also been investigated. In 2009, Sharma et al. [132] introduces an approach to understanding and solving the problem of brittleness of metallic glasses. Even a very brittle metallic glass (La based) can be forced to deform plastically at room temperature by inserting the other metallic glass layers. Enhanced plastic deformation has been observed for the multilayered glassy thin films as compared to their monolithic glassy layer. They suggested the possibility of fabricating a different kind of two-phase BMGs to show large plastic deformation. Subsequently, Kuan and his teammates [133] also develop the amorphous nanolaminates to detect that the apparent deformation mechanism transforms from highly inhomogeneous mode in the monolithic amorphous alloys to relatively more homogeneous mode in the micropillars of nanolaminates. Similar phenomena were observed under nanoindentation tests. For the shearing in a micropillar, the shear band can be treated as the formation of interfaces. Similarly to crack propagation on the interface of dissimilar materials, the deflection phenomenon in some BMGs can also be explained in terms of the Dundur's parameter [59, 134]. As sketched in Figure 2.33 [133], the necessary condition for the shear band in material 2 to deflect along the interface rather than to propagate into material 1 is when [135]

$$G_d/G_p > G_{ic}/G_c, \quad (2-3)$$

where G_d is the strain energy release rate of a deflected crack, G_p is the strain energy release rate of a penetrated crack, G_{ic} is the fracture energy of the interface, and G_c is the mode I

fracture energy of materials 1. If the inequality is reversed, then the crack will penetrate the interface and proceed into material 1. Thus, the relative tendency of a crack to be deflected by the interface or to pass through can be assessed by using this equation. This model demonstrates that the brittle problem of amorphous metallic glass thin films can be alleviated by interlaminating another metallic glass layer with a different modulus.

Chapter 3 Experimental procedures

Amorphous-crystalline multilayer films were alternatively deposited on the cleaned silicon substrate by magnetron sputtering. The basic nature of the multi-layered thin films is examined by X-ray diffraction (XRD) and scanning electron microscopy (SEM) with energy dispersive X-ray spectrometry (EDS). The microstructures of samples, as well as FIBed pillars, are identified by transmission electron microscopy (TEM). The mechanical properties of metallic thin film are evaluated by nanoindenter. Furthermore, room temperature microcompression tests are conducted by nanoindenter equipped with a flat-end Berkovich indenter. The flow chart of experimental procedures is shown in [Figure 3.1](#).

3-1 Raw materials

The targets used in this study were purchased from Well Being Enterprise Co., Ltd, Taipei, Taiwan. The purities of the elements are as follows, copper (Cu) is as pure as 99.99%, zirconium (Zr) is as pure as 99.9%, molybdenum (Mo) is as pure as 99.9%.

3-2 Sample preparation

3-2-1 Pretreatment for substrate

Multilayer thin films were deposited on P-type (100) silicon wafer. Before the starting of the depositing process, in order to remove the dust and impurities attached on the substrate, the following steps are adopted to clean the surface of substrate.

- (1) The substrate is placed in the ultrasonic cleaner filled with deionized (DI) water for

10 minutes to remove the dust on the surface of substrate.

- (2) An ultrasonic cleaner is used to clean the substrates in alcohol for 15 minutes to clean the greasy dirt on the surface of substrate.
- (3) After rinsing in alcohol, an ultrasonic cleaner is used to clean it in acetone for 15 minutes.
- (4) After rinsing in DI water, we used an ultrasonic cleaner to clean it in DI water for 15 minutes.
- (5) Finally, N₂ is used to dry the substrate.

3-2-2 Preparation for monolithic thin films and multilayer thin films

Two kinds of thin films were synthesized by co-sputtering with magnetron DC and RF guns. One is monolithic amorphous and monolithic nanocrystalline thin films, and the other is layer-by-layer deposition with alternative amorphous and nanocrystalline thin films. All metallic targets with 50.8 mm (i.e., 2 inches) in diameter were used at a working pressure of 3×10^{-3} torr. A rotary pump was used to achieve medium vacuum and a turbomolecular pump was used to achieve a base pressure less than 5×10^{-7} torr. There was a load-lock chamber, for quick and convenient exchanging of substrates without venting the main chamber. After achieving the base pressure ($< 5 \times 10^{-7}$ torr), Argon was introduced into the chamber and targets were pre-sputtered by inserting a movable shutter for 10 minutes. The flow rate of Argon was fixed at 30 standard cubic centimeters per minute (sccm). The working distance from the holder to the sputtering guns was 120 mm. During the deposition, the substrate was rotated with an average speed of 15 rpm for the uniform distribution of the film thickness.

Multilayered thin films were fabricated by co-sputtering on Si substrates. Our sputtering does not have the function of measuring the thickness of thin film simultaneously as

sputtering. For this reason, we have to operate manually to deposit each layer. First we opened the two DC sputtering guns for a period time we intended to deposit. Then we shut the Cu target and started to deposit the pure Zr materials. Repeat the above steps to form the multilayered sample, as sketched in [Figure 3.2](#). The thickness of each layer depends upon the deposition time and power in use.

3-3 Property measurements and analyses

3-3-1 X-ray diffraction

The glassy nature of the as-deposited ZrCu thin films was characterized by X-ray (XRD). The SIEMENS D5000 X-ray Diffractometry with a monochromatic Cu-K α ($\lambda = 1.5406 \text{ \AA}$) radiation, a working voltage of 40 kV and electron current of 30 mA, equipped with 0.2 mm graphite monochromator, is used. The scanning angle (2θ) covers from 20° to 60° using a scanning rate of 0.1° per six seconds.

3-3-2 SEM observations

The JEOL ISM-6330 TF scanning electron microscope (SEM) was selected to observe the microstructure and morphology of the cross-sectional multilayer thin films or pillars. The outer morphologies of the pillar samples before and after microcompression test were also examined by SEM. It could reveal the several shear-banding formations, propagations and interactions between crystalline and amorphous interface for the deformed pillar through a 360° examination using SEM.

3-3-3 Qualitative and quantitative component analyses

In order to identify the constituent component and confirm the composition percentage of the as-deposited thin film metallic glasses, the SEM equipped with energy dispersive X-ray spectrometer (EDS) was used for the qualitative and quantitative constituent analysis in this study. The surface of thin film metallic glasses was selected to confirm the composition percentage of the designed samples. Besides, the mapping function of the EDS system can also identify the uniform atomic distribution.

3-4 Nanoindentation tests

The MTS XP nanoindenter system was used to measure the hardness and Young's modulus of nanocrystalline and amorphous thin films via continuous stiffness measurement (CSM) mode. For thin films or submicron samples, it's possible to investigate hardness (H) and elastic modulus (E) profiles by nanoindentation technique at very shallow depths (on the order of nm). The nanoindentation testing was executed with a maximum load of 500 mN (Figure 3.3), using the Berkovich tip. The Berkovich tip is a three sided pyramid which is geometrical symmetry. It has a flat profile with a centerline-to-face angle of 65.3 degrees. For current case, a general rule of thumb is to indent less than 10% of the total film thickness to eliminate the substrate effect [136]. Therefore the indented depth is controlled around 200 nm loaded at $5 \times 10^{-2} \text{ s}^{-1}$ in this study. In addition, the nanoindenter is very sensitive to the external environment and the flat condition of specimen surface. It is necessary to keep clean and dry of the surface of thin films before nanoindentation test.

3-5 Microcompression tests

3-5-1 Preparation for microcompression samples

Microscale pillar samples for micro-compression testing are prepared using the SEIKO SMI3050 dual focus ion beam system (FIB, [Figure 3.4](#)), following the Uchic and Dimiduk method [\[106\]](#) with modification. A series of concentric-circle patterns were utilized to machine pillars to render the pillars to reach the optimized and minimum taper angle. The 30 keV and 7–12 nA currents Ga beam is initially directed perpendicular to the surface of the thin film specimen to mill a crater with a much larger size (about five times of the diameter of the final pillar) island located in the center. Then, the same voltage but smaller currents of 0.7–0.09 nA are used to refine the preserved island in the center to a desired diameter and height of the pillar.

3-5-2 Microcompression tests using nanoindentation system

The microscale pillars are test in uniaxial compression at room temperature by using a commercially available nanoindentation system. Nanoindentation systems are nominally designed for performing low-load depth-sensing indentation tests using a diamond-like tip. With high datum acquisition rate, discrete events including phase transformation and shear instability initiation can be distinguished during a nanoindentation test. Microcompression tests are conducted with the MTS nanoindenter XP equipped with a flat-end Berkovich indenter (machined by FIB) which has an equilateral triangle cross-section measuring 13.5 μm in side length, as shown in [Figures 3.5 and 3.6](#). The microcompression is also performed in the CSM mode and range of the corresponding strain rates vary from 1×10^{-4} to $1 \times 10^{-2} \text{ s}^{-1}$.

3-5-2 Preparation for TEM foils of the deformed micropillars

In this study, one of the most important steps is to prepare the TEM specimen for the deformed micropillars. To explore the detailed microstructure of the deformed micropillars,

the TEM foils were fabricated by FIB using a trenching and liftout technique [137-139]. The schematic illustration for preparing TEM specimen procedures is shown in Figure 3.7 [139]. First of all, the carbon source is deposited onto the deformed micropillar to fill with empty around it in order to provide a support and protect sample, as shown in Figure 3.8. Then, the general process to fabricate TEM sample is applied. The slope-etching is employed to cut trenches around the pillar with an energetic Ga ion beam. Next, the TEM foils could be further thinned by using the Ga ion beam with relative lower voltage and current. Finally, the TEM samples are moved on a carbon-coated Cu grid by acicular capillary with electrostatic induction.

3-6 In-situ TEM nanocompression tests

3-6-1 Preparation for nanocompression samples

Nanopillars were prepared from as-deposited thin films using FIB system (FEI Nova-200 NanoLab Compatible). Figure 3.9 shows the typical six steps for in-situ lift-out from the thin film: (a) first cut; (b) release cut; (c) tip attach; (d) extraction; (e) holder attach; and (f) tip separation [140]. The first three steps are the excision of the lift-out sample using FIB milling and extraction of the sample, as shown in Figures 3.9(a), (b), and (c). The most important step is the “holder-attach” step, during which the wedge, also called a lift-out grid, was attached with sample by ion beam-induced carbon deposition, as shown in Figures 3.9(d), (e), and (f). Then the sample is attached to the lift-out grid by carbon deposition and later detached from the probe tip point using FIB milling. The final step is the thinning of the sample into an electron-transparent thin foil required for TEM inspection using FIB milling.

The nanopillars fabricated by FIB with ~140 nm in diameter for the pillar tip and ~250

nm in diameter for the central and bottom portions, with a pillar length of $\sim 1.5 \mu\text{m}$. The length to diameter aspect ratio is about 11, above the aspect ratio of 2-5 conventionally used for compression specimens. The high aspect ratio was used in order to prevent possible damage to the indenter as it may accidentally hit the pillar base.

3-6-2 In-situ TEM nanocompression tests using Hysitron system

In-situ TEM compression tests are conducted by a novel and recently developed Hysitron PI 95 picoindenter TEM holder (Hysitron Inc., Minneapolis, MN) on a JEOL 2010F TEM, equipped with a diamond flat punch $1.5 \mu\text{m}$ diameter. The PI 95 TEM picoindenter holder, as shown in [Figure 3.10](#), is the first depth-sensing indenter capable of direct-observation nanomechanical testing in a TEM. It is not only possible to catch the mechanical response of nanoscaled structure, but also to acquire load-displacement data simultaneously. Furthermore, a unique video system allows for time synchronization between the load-displacement curve and the corresponding TEM video image. The current TEM video has a framing speed of 13 frame/s. The PI 95 TEM holder utilizes a three-axis coarse positioner and a 3D piezoelectric actuator for tip fine positioning and mechanical testing. With this newly developed transducer, quantitative force-displacement curves and snapped video can be acquired simultaneously. It is powerful tool to record the deformation behavior of nanoscaled materials. The nanocompression is also performed in the displacement-control mode and the corresponding strain rate is $5 \times 10^{-3} \text{ s}^{-1}$.

Chapter 4 Experimental results

4-1 Sample preparations

In this study, a magnetron sputtering deposition system, with three independent magnetron targets (two DC guns and one RF gun), is used to sputter Zr, Cu, and Mo. All samples with layered structures were deposited onto the Si substrates with variable target powers. [Table 4.1](#) lists the deposition rates with variant target materials at different powers. In our general sense, the maximum limit in film thickness is approximately 5 μm by taking account of the adhesion trouble between interfaces of thin film and Si substrate.

Amorphous-crystalline multilayer films were alternatively deposited onto Si substrate by magnetron sputtering. To examine the length effect of the crystalline film on shear band interactions, two types of multilayer films were prepared. The first type consists of seven layers (denoted as L7), namely, ZrCu/Zr/ZrCu/Zr/ZrCu/Zr/ZrCu, with the individual thicknesses of the ZrCu amorphous (h_a) and Zr crystalline layers (h_c) being 570 and 190 nm, respectively. The total film thickness (h_t) of L7 is 2850 nm. The variant thicknesses of each layer were examined by cross-sectional TEM bright-field images, as shown in [Figure 4.1](#) for a typical multilayer (ZrCu/Zr) thin film. From the observation of TEM images, the gray layers and white layers represent the ZrCu layers with nominal 570 nm in thickness and the Zr layers with nominal 190 nm in thickness, respectively. The second type is a three-layer film (denoted as L3), namely, ZrCu/Zr/ZrCu, with h_a and h_c being 550 and 880 nm ([Figure 4.2](#)), respectively. This film has a total thickness of 1980 nm. All multilayer specimens have an amorphous top layer to ensure the initiation of shear bands from this layer. To provide the baseline comparison, monolithic ZrCu amorphous and pure Zr films were also prepared.

Both films are nearly 2500 nm in thickness. In addition, the Mo(BCC) and Cu(FCC) crystalline layer are also be coupled with the ZrCu amorphous layer, as shown in [Figure 4.3\(a\)](#) and [Figure 4.3\(b\)](#), respectively. The ratio of amorphous to crystalline layer in thickness is close to 1:1. Each layer is about 500 ± 10 nm in thickness.

4-2 EDS and XRD analyses

The compositions of the as-deposited thin films were characterized by SEM/EDS. The amorphous thin film (denoted as ZrCu) has a composition of $Zr_{45}Cu_{55}$ (in atomic percent), as also confirmed by EDS. Its composition is reliable within our prediction.

The nature of the deposited thin films was characterized by XRD. [Figure 4.4](#) shows the XRD patterns obtained from the ZrCu thin film. There is no detectable crystalline peak between the diffraction angles (2θ) of 20° to 60° for the ZrCu thin film. In the low diffraction angles range between 30° to 50° , a broad diffused peak is observed clearly in the XRD pattern of the as-deposited thin film, approximately indicating that the ZrCu thin film possesses the amorphous structure.

In the previous study of our lab, Chen [\[141\]](#) reported that the structure of as-deposited pure Zr thin film. According to the XRD pattern of the pure Zr thin film, there exhibits a predominant (0002) plane texture of Zr at 35° , as shown in [Figure 4.5](#). Moreover, the as-deposited Cu film displays the similar occurrence with the major (111) plane textures at 43.3° and a minor (002) peak at 50.5° , as shown in [Figure 4.6](#). Based on these XRD results, the growth of the individual crystalline Zr and Cu layers are both along the close-packed crystalline planes.

4-3 Mechanical property analyses

There has been considerable interest in the last decade in the mechanical characterization of thin film systems using nanoindentation tests, especially for measuring Young's modulus and hardness. The advent of nanoindentation testing instruments has enabled depths of penetration to be measured with nanometer resolution to depths of around several micrometers. A general rule of thumb is to indent to around 10% of film thickness so as to avoid the substrate effect. For the as-deposited thin films in this study, films of minimum thickness 2-3 μm (indent penetration depths of about 200-300 nm) can be expected to provide reliable data from most available instruments. Up to now, the most widespread and famous model for nanoindentation data analysis is one in which the unloading data are assumed to arise from a purely elastic contact. This approach was first developed by Oliver and Pharr [142], and was known as the Oliver-Pharr method. During the course of the instrumented indentation process, a record of the depth of penetration is made, and then the area of the indenter is determined using the known geometry of the indentation tip. While indenting, various parameters such as load and depth of penetration can be measured. The typical load-displacement curve is shown schematically in Figure 4.7. The slope of the curve, dP/dh , upon unloading is indicative of the stiffness S of the contact and the experimentally measured stiffness of the upper portion of the unloading data. The stiffness of the contact can be used to calculate the reduced elastic modulus E_r :

$$E_r = \frac{1}{\beta} \frac{\sqrt{\pi}}{2} \frac{S}{\sqrt{A_c}}, \quad (4-1)$$

where A_c is the projected indentation area at the contact depth h_c , and β is a geometrical constant on the order of unity. A_c is often approximated by a fitting polynomial as shown below for a Berkovich tip:

$$A_c(h) = C_0 h^2 + C_1 h + C_2 h^{1/2} + C_3 h^{1/4} + C_4 h^{1/8}, \quad (4-2)$$

where C_0 for a Berkovich tip is 24.5. The reduced modulus E_r is related to Young's modulus E_s of the test specimen through the following relationship from contact mechanics:

$$\frac{1}{E_r} = \frac{1-\nu_s^2}{E_s} + \frac{1-\nu_i^2}{E_i} \quad (4-3)$$

Here, the subscript i indicates a property of the indenter material and ν is the Poisson's ratio. For a diamond indenter tip, E_i is 1140 GPa and ν_i is 0.07 [142]. The Poisson's ratio of the specimen, ν_s , generally varies between 0 and 0.5 for most materials (though it can be negative) and is typically around 0.3. There are two different types of hardness that can be obtained from a nanoindenter: one is as in traditional macroindentation tests where one attains a single hardness value per experiment; the other is based on the hardness as the material is being indented resulting in hardness as a function of depth:

$$H = \frac{P}{A_c} . \quad (4-4)$$

The hardness (H) is given by the equation above, relating the maximum load to the indentation area. According to equation 4-2, the elastic modulus and hardness of the materials can be easily extracted by equation 4-4.

Prior to microcompression, these monolithic samples were subject to nanoindentation to measure the elastic modulus and hardness, and the results are compiled in [Table 4.2](#). As shown in the table, the nanocrystalline Zr has a higher modulus and hardness than the amorphous ZrCu. The Young's moduli for the ZrCu TFMG, Zr, Cu and Mo thin films are 93 GPa, 125 GPa, 136 GPa and 280 GPa, respectively. Besides, the modulus and hardness values of three-layer thin film conducted by nanoindenter are 106 and 4.8 GPa, respectively. Since the top layer of the three-layer thin films is the amorphous ZrCu, the modulus and hardness values of the three-layer film are similar to those of the monolithic amorphous ZrCu film.

4-4 Microcompression tests

4-4-1 Results for ZrCu amorphous, Zr and Cu nanocrystalline micropillars

The FIB machined pillar before microcompression test is shown in [Figure 4.8](#) for the (a) ZrCu TFMG and (b) monolithic Zr thin films. The L7 and L3 multilayer micropillars are also prepared FIB, as shown in [Figures 4.9\(a\) and \(b\)](#). In accordance with the recommendation provided by finite element modeling [107], all micropillars were designed to have an approximate aspect ratio of 2~3. Due to the convergence angle of the ion beam, all micropillars are slightly tapered, and the taper angle from the top to the bottom is around 2.5°~3.0°.

Microcompression tests on monolithic and multilayer pillars are conducted by the nanoindenter system loaded at strain rates around $2 \times 10^{-3} \text{ s}^{-1}$ to a preset displacement of 300 nm, which corresponds to about 15% of strain. The compressive engineering stress-strain curve of ZrCu amorphous micropillar is shown in [Figure 4.10](#). According to this figure, the

yield strength is obtained from the departure of the linearity of the early portion. Because the sample is tapered, yielding will occur from the top of the sample which is the location with the minimum cross-sectional area. Accordingly, the yield strength can be extracted from the departure load divided by the top area. The curve for amorphous ZrCu is noted to show two pronounced strain bursts with the first one occurs immediately after yielding. The sudden strain discontinuity has been commonly observed during the compression of amorphous micropillars.

To correlate the strain bursts with sample deformation, SEM micrograph of the compressed specimen was taken and is displayed in [Figure 4.11](#). Based on the morphology of the deformed ZrCu amorphous micropillar, it is readily observed that typical localized shear is the dominant deformation mode in the amorphous micropillar. Apparently, the pronounced strain bursts in the stress-strain curve are associated with the sudden sample slides resulted from the localized shears. Shear bands are anticipated to initiate from the corner of contact interface between sample and compression flat punch. The interface between sample and flat-punch is subjected to the maximum stress, not only because it is the minimum cross-sectional area as a result of tapered pillar, but also due to the large constraint caused by the friction between the test sample and flat punch. After suffering the compression test, it deserved to be mentioned that Zr-based micropillars did not appear the catastrophic fracture. It is consistent with Lai et al.'s results [\[116\]](#) on the micorscale compressive behavior of the Zr-based BMG.

In contrast to the ZrCu amorphous micropillar, the deformation of Zr nanocrystalline micropillar appears to be different. It exhibits a much uniform deformation. As shown in [Figure 4.12](#), the stress-strain curve for the material is essentially continuous and exhibits some strain hardening. The occurrence of strain hardening is usually indicative of the operation of dislocation-mitigated processes which can contribute to homogeneous deformation and

plasticity enhancement. Indeed, the compressed Zr micropillar (Figure 4.13) shows slight sample barreling, typically observed in ductile crystalline solids. It is particularly noted in Figures 4.10 and 4.12 that, despite the fact that the deformation mode of amorphous ZrCu and nanocrystalline Zr is entirely different, yield strengths of the two materials are similar, both at about 2.6-3.0 GPa.

As same as the results of nanocrystalline Zr, the curve for monolithic nanocrystalline Cu micropillar, as shown in curve (2) of Figure 4.14, is essentially continuous and possesses some strain hardening. The existence of strain hardening and large plasticity is usually attributed to the present of dislocation movement and interaction. The morphology of compressed Cu micropillar, as shown in Figure 4.15, is noted to be slightly sample barreling. Similar observations were reported earlier in other ductile nanocrystalline metals [143].

4-4-2 Results for ZrCu/Zr multilayer micropillars

Upon realizing that nanocrystalline Zr deforms uniformly and can exhibit large plasticity, we subsequently prepare two types of multilayer with alternating amorphous ZrCu and crystalline Zr layers. The ability of a crystalline layer to block a propagating shear band is further examined in L7 and L3 pillars (Figure 4.9) from a point of view of layer thickness. Both L7 and L3 specimens have the amorphous ZrCu as the top layer to ensure the initiation of shear bands under compressive loading. These samples were subsequently compressed at a strain rate of $2 \times 10^{-3} \text{ s}^{-1}$ to a predetermined displacement of 300 nm, which corresponds to about 15% of strain. Compressive stress-strain curves of L3 and L7 are presented in Figure 4.16. The two curves appear similar, each punctuated by several strain bursts, indicating discrete shear band formation in the samples. However, even though the curves are similar, deformation mode in these two samples is quite different; this is shown in Figures 4.17 and 4.18. For L7,

which contains 190 nm-thick inserted nanocrystalline Zr layers, several shear bands were developed in the top amorphous layer when the sample was compressed to a displacement of 300 nm, as shown in [Figure 4.17](#). SEM micrographs taken from all 360° angles reveal 5 visible shear bands on the sample surface and two of them are fully developed, shearing through and completely deforming the 190 nm Zr layer. The other three minor shear bands were apparently dissipated by the crystalline layer. Moreover, L7 deforms in a similar fashion as the monolithic ZrCu, namely, exhibiting extensive localized shear. Apparently, the thin nanocrystalline Zr layer ($h_c = 190$ nm) is unable to stop or block the propagating shear bands.

By contrast, the deformation mode of L3 sample ([Figure 4.18](#)) is different. The top amorphous layer is appreciably barreled. Whereas many localized shear bands form, there is no sign of deep penetration of shear bands in the nanocrystalline Zr layer. A careful 360° examination under SEM of this sample reveals eleven shear bands emerging onto the surface of the top amorphous layer. Each shear band either protrudes on the external surface or terminates at the amorphous-crystalline interface. This observation indicates that shear bands originated from the amorphous layer can be effectively arrested by the “thick” nanocrystalline Zr layer ($h_c = 880$ nm). To elucidate the interaction between shear band and nanocrystalline Zr, we conducted TEM examination of the microstructure in the Zr layer near the vicinity of an impinged shear band, as presented in section 4-5.

To explore the effect of the strength and the thickness ration of the crystalline layer with respect to the amorphous layer, the ZrCu/Zr 100/100 nm micropillar is tested. For microcompression test on ZrCu/Zr multilayered pillars, the deformation behavior appears to be the same as the monolithic ZrCu sample ([Figure 4.11](#)). [Figure 4.18](#) shows the engineering stress-strain curve and SEM micrograph of ZrCu/Zr 100/100 nm. Several strain bursts, indicating discrete shear band formation in the samples, can be easily observed from [Figures](#)

4.19(a) and 4.19(b). This strain discontinuity has been commonly observed during the compression of amorphous micropillars. Apparently, major shear band initiated in top ZrCu layer passes through the amorphous ZrCu and nanocrystalline Zr layers.

4-4-3 Results for ZrCu/Mo and ZrCu/Cu multilayer micropillars

In the above-mentioned study on L7 and L3 micropillars, amorphous layers are coupled with nanocrystalline Zr layers. In addition to the Zr with HCP in crystal structure, the nanocrystalline layer that can also be coupled with the amorphous layer can be of either FCC or BCC crystal structure. The effects of the different crystalline layers may be the one of important issues in this experiment. The microcompression tests were conducted on the ZrCu/Mo/ZrCu/Mo/ZrCu multilayered samples. According to the preliminary results, we expect that the sufficient thickness of crystalline layer can absorb the kinetic energy of the shear bands developed by the ZrCu amorphous layer. Based on the SEM cross-sectional image, the thicknesses of the ZrCu amorphous and Mo crystalline layers are 500 ± 10 nm, as shown in Figure 4.3. The engineering stress-strain curve of ZrCu/Mo/ZrCu/Mo/ZrCu is presented in Figure 4.20. Compared with the former stress-strain curve of the L3 pillar, major shear sliding was observed via the shear bands initiated from the ZrCu layer passing through the Mo crystalline layer. Figure 4.21 shows the SEM images of before and after microcompression, obviously the brittle Mo crystalline layer cannot absorb the kinetic energy of the shear bands initiated from the ZrCu amorphous layer. The Mo crystalline layer seems to crack after compression test even though Mo has higher modulus and hardness than ZrCu amorphous (Table 4.2). Several cracks were generated inside the Mo crystalline layer during the microcompression test.

To explore the effect of the strength of the crystalline layer with respect to the

amorphous layer, additional attempt was made to replace the “hard” nanocrystalline layer by a “soft” one. Specifically, we fabricate the L5 structure but, instead of having the Mo layer, a soft nanocrystalline Cu layer was used. Yield strength of the nanocrystalline Cu is only about 1.2 GPa [61, 144], far less than that of the amorphous ZrCu (> 2 GPa). As a result of strength disparity, this sample exhibits the preferential deformation of the “soft” nanocrystalline Cu layer in compression, as shown in Figure 4.22(a). In other words, at the stress level that the Cu layer was squashed, the amorphous phase was still in the elastic range, thereby no shear band could be initiated. This is also supported by the fact that the stress-strain curve (Figure 4.22(b)) exhibits yielding at about 1.2 GPa, the yield strength of nanocrystalline Cu, followed by work hardening associated with the deformation of the Cu layer. These results indicate that using thick (>500 nm) underlayers would probably not be very useful since, in principle, the strength of the amorphous-crystalline multilayer will be limited by the strength of this soft underlayer.

Continuous studies of the ZrCu/Cu multilayer micropillars have been conducted by our group member, Mr. I. C. Lin [145]. For the microcompression tests, the engineering stress-strain curves for the monolithic amorphous ZrCu and crystalline Cu as well as ZrCu/Cu multilayer micropillar samples are shown in Figure 13, in which these curves are plotted on the same axes with their origins offset strain of 0.1 for the clarity of presentation. In this study, the yield will occur from the top of the micropillar samples due to the taper effect which is inevitably caused by FIB milling process. For this reason, the yield strength of micropillar can be obtained from the departure load divided by the top area and elastic modulus can be extracted from a consideration of the substrate compliance [115]. The deformation behavior appears to be different among these three different multilayer systems. Although the stress-strain curve showed a bend-over phenomenon before the strain burst event, the deformation of 100/10 nm ZrCu/Cu multilayer micropillars is still dominated by

the emission of shear bands (Figure 4.23) in a manner of strain burst to release the energy, similar to that observed in the monolithic amorphous ZrCu micropillar, as shown in the curve (3) of Figure 4.14. This means that with increasing Cu layer thickness, the elastic-to-shear transition becomes more gradual. This should be caused firstly by the deformation and work hardening of the 10 nm Cu layers, followed by the shear band initiation in the ZrCu layers upon the system flow stress reaching the ZrCu yield stress. Following this trend, for the 100/100 nm micropillar, a smooth curve with no noticeable strain burst is recorded (curve (4) of Figure 4.14). The multilayered pillar exhibited a yield strength of ~ 2.3 GPa with an overall plastic engineering strain above 20%. Since the lower portion is basically undeformed, the original upper half (~ 1.3 μm in height and ~ 0.9 μm in diameter) has been compressed to ~ 0.6 μm in height and ~ 1.3 μm in diameter. This means that the upper half has experienced a compressive engineering strain in height of $\sim 50\%$, an increment of cross-section of $\sim 110\%$ or a true strain of ~ 0.75 . Note that the 100/100 nm micropillars did not fail after such extensive compressive straining, as shown in Figure 4.24.

Since the monolithic crystalline Cu and 100/100 ZrCu/Cu micropillar are both homogeneously deformed, the strain hardening behavior in these micropillars can be compared. The strain hardening exponents of the monolithic crystalline Cu and the 100/100 ZrCu/Cu micropillars are calculated to be ~ 0.16 and ~ 0.13 . It is noted that monolithic amorphous micropillars normally do not work harden [115, 116]. The appearance of strain hardening is obviously caused by the presence of Cu interlayers. Similar strain hardening effect has also been observed in an amorphous/crystalline nanolaminate [55]. Based on the microcompression results, we may conclude that the crystalline Cu layer produces a positive effect on the ZrCu/Cu multilayer films, in particular, the film plasticity. The current results reveal an important message that, specifically, the current finding from the microcompression tests is consistent with that observed from the nanoindentation tests; namely, the crystalline

Cu layers can offer positive influence on the ZrCu/Cu multilayer films. The current results demonstrate that the homogeneous deformation in the brittle amorphous ZrCu layer with the help from the crystalline Cu underlayer. The uniform deformation and the ultrahigh plasticity are mainly attributed to structure barrier strengthening, which results from the multilayer system.

To further demonstrate the compressibility of the 100/100 ZrCu/Cu micropillar with minimum taper effects, rectangle micropillars were tested. The pillars before and after compressive straining are shown in [Figures 4.25\(a\) and 4.25\(b\)](#). The original rectangle micropillar has been compressed significantly to multilayered pan-cake appearance. The corresponding true stress-true strain curve is shown in [Figure 4.25\(c\)](#), presenting the superplastic-like flow behavior at room temperature with a compressive engineering strain in height of ~70%, increment of cross-section of ~160% or a true strain of ~1.0.

These results show that the deformation of ZrCu/Cu nanolayered micropillars depends significantly on the thickness of ductile Cu layers under uniaxial microcompression conditions. It is interesting to observe that the critical metallic thickness of Cu layers for the superplastic-like flow is around 100 nm, equal to the thickness of amorphous ZrCu layers.

4-5 TEM analyses of the microstructures on deformed micropillars

4-5-1 TEM analyses for ZrCu/Zr micropillars

It is necessary to prepare the TEM foil of the deformed micropillars in the case of observing the interaction between shear band and nanocrystalline Zr. Cross-sectional TEM

samples were fabricated by FIB with a trenching and liftout technique [137-139]. The procedures for preparing TEM samples are shown in Figure 3.8.

TEM micrographs showing the L7 pillar deformed to a fixed displacement of 300 nm at $2 \times 10^{-3} \text{ s}^{-1}$ are presented in Figure 4.26. The ZrCu layer still retains its amorphous nature after compression, even in the region where shear bands were propagating through (marked by the dotted line). There are two offsets on the left pillar surface, as circled in Figure 4.26, as a result of propagating shear bands. The offset, when viewed exactly edged-on, is about 30-50 nm. It is evident in Figure 4.15 that the 190 nm-thick Zr layer were sheared by the passage of the principal shear band, in a fashion similar to the localized shear in a nanoscale Au/Cu multilayer system [146]. However, intersecting point of the shear band and the crystalline Zr layer is difficult to pin down because the lack of structure features to identify the exact path of a propagating shear band. Consequently, we trace the principal shear (the dotted line in Figure 4.14) to position the location of intersection and to characterize the structure of the crystalline Zr layer in the vicinity of the this region.

In contrast to L7 sample, the L3 (Figure 4.27) sample, which consists of thick Zr layer (880 nm) was deformed quite differently. In the L3 specimen, the top amorphous ZrCu layer was barreled and deformed semi-uniformly from the initial thickness of 550 nm to the final 250-300 nm, or a plastic strain of 50-55%. The initial diameter of the top layer was about 975 nm and became 1200 nm after deformation. This large uniform plastic deformation in a micropillar is remarkable and has only been observed in a ductile nanocrystalline Ni [62]. It is noted that the plastic deformation occurs not only in the top amorphous layer, but also in the nanocrystalline Zr, as shown in Figure 4.27. In fact, the total thickness of the Zr layer decreases from the initial 880 nm to the final 830 nm. However, deformation of the Zr layer occurs primarily in the region immediately underneath the amorphous-crystalline interface,

indicating a strain gradient.

4-5-2 TEM analyses for ZrCu/Cu micropillars

To further evaluate deformation behaviors of ZrCu/Cu multilayer micropillar samples during compression, the compressed micropillars are examined by TEM and displayed in [Figure 4.28](#). First, the TEM longitudinal section of the 100/10 nm ZrCu/Cu multilayer micropillars can be clearly observed several obvious offsets initiated from shear band propagation on the micropillar surface in [Figure 4.28\(a\)](#). For the 100/100 nm ZrCu/Cu multilayer micropillar, no shear fracture can be observed in [Figure 4.28\(b\)](#) and plastic deformation occurs not only in the crystalline Cu layer but also in the amorphous ZrCu layer. At the top portion of micropillar, the reduction in thickness is above 50%. Because of ductility nature of pure Cu, the crystalline Cu layer is easier to be deformed than the amorphous ZrCu layer under the applied stress. Thus, it exhibits a plastic flow along the transverse direction in copper layer and the plastic flow acts as a shear force at interface causing non-stress concentration at amorphous layer. It means that the amorphous layer can be deformed to large plastic strain without stress concentration, causing a homogeneous deformation. These results suggest that the plasticity of amorphous ZrCu has been alleviated by the addition of crystalline Cu layer.

Furthermore, the longitudinal section of the compressed 100/100 nm ZrCu/Cu rectangular micropillar was also examined by TEM, as shown in [Figure 4.29](#). By measuring the final thickness of the severely strained ZrCu or Cu layers (some drop to 10 nm from the unformed 100 nm thick), the local engineering strain in height can be as high as ~90% or a true strain of ~2.3. Multiple shear events could be observed in the thicker amorphous ZrCu layers. No shear event can be observed in the thinner amorphous ZrCu layers due to the

merging effect of pronounced plastic deformation to the shear events. Nevertheless, for the deformed 100/100 nm ZrCu/Cu micropillar, semi-homogeneous deformation occurred in both the nanocrystalline Cu and amorphous ZrCu layers. This means the shear cracks have been effectively suppressed during compression for the 100/100 nm ones. The Cu layers should still undergo conventional dislocation movements causing the strain hardening behavior as observed in [Figure 4.25\(c\)](#).

4-6 In-situ TEM compression tests

Based on the results of 100/100 nm ZrCu/Cu micropillars, the homogeneous-like deformation behavior was demonstrated. In the case of metallic glasses, the deformation can be divided into inhomogeneous and homogeneous deformation. We tried to figure out the critical sample size below which shear band localization would disappear and the sample can deform homogeneously. This experiment was conducted by in-situ TEM nanocompression tests. It provided a powerful tool to probe the deformation behavior under nanoscale resolution.

Several predetermined displacements, 100, 200 and 300 nm, were initially selected for the in-situ compression of ZrCu nanopillars. However, after several trials, it was found that displacements less than 200 nm would produce limited useful information. Subsequently, most examinations were conducted on samples compressed to a displacement of 300 nm. The load-displacement (similar to engineering stress-strain) curves from several samples are summarized in [Figure 4.30](#). Although there exist slight variations, probably caused by the initial misalignment of the samples, the shapes of these curves are similar. The yield strength is between 1.8 and 2.5 GPa, within the range reported in the literature [[114-116](#), [121-124](#), [128](#), [131](#), [147](#)].

The compressive load typically reaches its maximum level at a displacement of about 75 nm, followed by a gradual decrease. This load decrease is resulted from severe buckling or bending as will be shown below from the in situ TEM observations. The buckling phenomenon is inevitable due to the high aspect ratio (~ 11) and, possibly, sample bending due to misalignment. In fact, it has been pointed out by Zhang et al. [107] that buckling would be severe when the aspect ratio of as-prepared pillars is greater than 5. For the current ZrCu nanopillars, the reasonable maximum compressive strength, without severe buckling or bending, would be the upper-bound value of about 2.0-2.5 GPa.

To view the in situ deformation, a series of cropped TEM video frames recording the deformation of ZrCu nanopillar are shown in sequence in Figures 4.31(a)~(h), together with the corresponding load-displacement curve (inset). The bottom part of the sample (gray area) is the silicon substrate. The pillar is tapered ($\sim 3^\circ$). To perfectly align nm-sized compressive sample is extremely challenging and almost impossible. As shown in the Figure 3.31, the sample axis is slightly off the compressive axis ($\sim 2\sim 3^\circ$). The rationalization of the in situ TEM nanopillars deformation characteristics will be presented in Section 5-2.

4-7 Interface strength of multilayer pillars

In this section, the interface nature of metallic glass ZrCu/crystalline Zr is characterized through evaluating its energy and validated by the mechanical response of micropillar with $\sim 45^\circ$ inclined interface under compression. Previous multilayered specimens tested by tension or compression were all oriented with the interface parallel the loading axis under tension testing and perpendicular to the loading axis under compression testing. No inclined specimen was ever tested and examined. Thus, we can perform the compression testing for inclined ZrCu/Zr pillars with the layer interface oriented $\sim 45^\circ$ with respect to the loading

direction. In such a case, the applied shear stress reaches the maximum value along the interface, and the cohesion capacity of an interface can be evaluated, and then compared with the theoretical analysis calculated in Section 5-3.

Figure 4.32 shows the undeformed inclined pillar fabricated by focused ion beam (FIB). The thicknesses of the individual ZrCu and Zr layers, prepared by sputtering, are all around 500 nm. The diameter of the top micropillar portion is 910 nm, as labeled in Figure 4.32. It needs to make sure each time that the flat punch would contact the inclined pillar accurately during the microcompression process. For this reason, the current microcompression test was conducted with the method of load control under high drift rate (>1 nm/s). Thus, we can observe the instantaneous curves of load versus displacement. After compressing the pillar to the preset 260 nm displacement, the scanning electron microscopy (SEM) appearances of the deformed pillar taken from opposite views are shown in Figure 4.33. It shows that the deformation mainly occurred on the crystalline Zr layers despite of the existence of minor taper. In order to further elucidate the deformation characteristics of this inclined ZrCu/Cu pillar, a compressive test until failure was performed. The SEM observations of the failed pillar taken from opposite views are shown in Figure 4.34, showing that the shear fracture has rightly happened within the Zr metal layer. Figure 4.35 shows the stress and strain curve of the inclined multilayer pillar till to failure. The plastic compressive flow happens on the high stress scale of about 2.0-2.3 GPa, meaning that the maximum shear stress along $\sim 45^\circ$ is about 1.4-1.6 GPa. This suggests that the ZrCu/Cu interface strength, τ_i , should be higher than this level. The detailed calculation and discussion of interface strength on multilayer pillars will be presented in Section 5-3.

Chapter 5 Discussion

5-1 Microcompression tests

5-1-1 Calculation of Young's modulus

In consequence of the slightly tapered micropillars, it is difficult to calculate the Young's modulus (E) accurately, that is, Young's modulus is sensitive to the sample misalignment. In order to check the accuracy of yield strength, Lee et al. [115] have developed a methodology to evaluate the values of Young's modulus. In current study, the major effect of the tapered micropillars needs to be considered for modification of the Young's modulus.

Since the micropillars are uniformly tapered, as illustrated in Figure 5.1, the total measured displacement, Δh , is

$$\Delta h = \frac{1}{h_o} \int_0^{h_o} \Delta u(x) dx, \quad (5-1)$$

where h_o is the height of the pillar, $\Delta u(x)$ is the local displacement. In the elastic range, with $\sigma = E\varepsilon$, $\sigma(x) = P/A(x)$ and $\varepsilon(x) = \Delta h(x)/h_o$, where P and A are instantaneous load and sample cross section area, respectively, the Eq. (5-1) is deduced to

$$\Delta h = \int_0^{h_o} \varepsilon_x dx = \int_0^{h_o} \frac{P}{\pi(d_o + x \sin \theta)^2 E} dx, \quad (5-2)$$

where d_o is the radius of the pillar, and $\theta = 2.5^\circ$ is the taper angle. As $\sin \theta \approx \theta$, the equation leads to

$$\Delta h = \left(\frac{P}{\pi E d_o^2}\right) \left(\frac{d_o}{2\theta}\right) \ln\left(1 + \frac{2\theta h_o}{d_o}\right). \quad (5-3)$$

Therefore,

$$E = \left(\frac{P}{\Delta h}\right) \left(\frac{\ln\left(1 + \frac{2\theta h_o}{d_o}\right)}{\pi d_o 2\theta}\right). \quad (5-4)$$

Substitute $d_o = 1 \mu\text{m}$ and $h_o = 2.5 \mu\text{m}$ (for the $1 \mu\text{m}$ micropillar sample), one has

$$E = 2.64 \times 10^{12} \left(\frac{P}{\Delta h}\right), \quad (5-5)$$

where P and Δh are in the units of Newton and meter, respectively. Thus, the modulus of the micropillars can be extracted with the consideration of this methodology. It can be seen in [Table 5.1](#) that the modulus (E) and yield stress (YS) of the monolithic nanocrystalline Zr (129 and 3.2 GPa) are the highest among the four different pillar samples. The modulus strength, in a descending order, is nano-Zr (129 and 3.2 GPa), L3 (124 and 2.7 GPa), L7 (108 and 2.5 GPa), and amorphous ZrCu (92 and 2.7 GPa). In comparison with seven-layer sample, the higher volume fraction of the nanocrystalline Zr layer in the three-layer thin film would contribute higher modulus and stress of the pillar under microcompression. Therefore, the corrected results of the Young's modulus indirectly indicate that the misalignment artifact on the yield strength measurement is minimized in this experiment.

Besides, based on the concept of composite materials, in the present compression tests, the multilayer samples were under the iso-stress condition. Traditionally, the modulus of the sample E_t can be computed using the iso-stress model

$$\frac{1}{E_t} = \frac{V_a}{E_a} + \frac{V_c}{E_c}, \quad (5-6)$$

where E_a and E_c are the moduli, and V_a and V_c are the volume fractions of amorphous and crystalline phases, respectively. Based on the nanoindentation data (moduli of ZrCu and Zr thin films are 92.5 and 125.1 GPa), the predicted modulus values for L3 and L7 would be 104.6 and 97.5 GPa, respectively. These predicted values and the variation trends are in moderate agreement with that measured from microcompression tests (~124.3 and 106.6 GPa), suggesting the validity of the iso-stress model.

5-1-2 Homogeneous-like and shear-band deformation of multilayer micropillars

Due to the “shear events” controlled deformation, suppression of compressive instability for the 100/100 nm micropillar requires an operative mechanism to restrict the shear events to evolve into shear cracks. On one hand, the introduction of ductile Cu layers can provide the microstructural possibility to toughen the micropillar. On the other hand, under uniaxial compression, the amorphous ZrCu and crystalline Cu layers are subjected to tensile and compressive stress, respectively, owing to the preferential extension along the lateral direction for the softer Cu metallic layers. The existence of interior stress gradient is beneficial for the multilayer micropillars to exhibit plastic deformation ability, similar to the case of bending thin metallic amorphous plates [148, 149]. In this case, the high-stiffness ZrCu amorphous layers could become the effective geometric objects to hamper the propagation of shear bands initiated around the plastically soft objects, i.e. the amorphous ZrCu/crystalline Cu interfaces.

In previous studies, bending produces an inherently inhomogeneous stress state where a

shear band is arrested by the gradient in applied stress, $\Delta\sigma = 2\sigma_y/D$. Here, the σ_y is the yield stress and D is the thickness of the bending plate. Stability against crack opening is geometrically ensured when $D/2 < R_p$ [148, 149], where R_p is the size of plastic zone. Thus, following this fundamental concept, it is reasonable to derive that if the thickness of ZrCu glassy phase L_a , i.e., the distance for shear bands propagation, becomes comparable with the plastic zone size, i.e, $L_a \leq R_p$, the extension of shear band can be arrested. This concept has been exploited to design ductile bulk metallic glasses composites [44, 57, 59, 60].

The plastic zone size of metallic amorphous/crystalline nanolayered micropillars can be estimated by analogizing shear events as minor crack propagation. For a mode I opening crack, the characteristic dimension R_p of a crack tip plastic zone can be expressed as [150]:

$$R_p = K_{IC}^2 / 2\pi\sigma_Y^2, \quad (5-7)$$

where K_{IC} is plain-strain fracture toughness. In a laminate consisting of alternative brittle and ductile layers, the crack extension resistance is enhanced as the thickness of ductile metal layers increases, thus, a critical value of the stress intensity factor, i.e. the plain-strain fracture toughness, can be estimated by [151],

$$K_{IC} \approx \sigma_Y \sqrt{2\pi L_m}, \quad (5-8)$$

where L_m is the thickness of plastic metal layers. Therefore, combining eqns. (5-7) and (5-8), the plastic zone size of the amorphous/metallic laminates can be given by:

$$R_p \approx L_m. \quad (5-9)$$

This means that the plastic zone of amorphous/crystalline multilayered micropillars equals to the thickness of plastically crystalline layers, consistent perfectly with the experimental observation of this study. The condition with $R_p \approx L_m$ will provide the matched plastic deformation ability between amorphous ZrCu and nanocrystalline Cu layers. Thus, one of necessary conditions for amorphous/metallic multilayered micropillars to deform plastically is that the thickness of amorphous layers should be comparable or less than that of metallic layers, i.e., $L_a \leq L_m$.

To satisfy strain compatibility at the crystalline/amorphous interface, the metallic Cu layers must have matched flow stress with the amorphous ZrCu layers. Several researches have suggested that for the metallic layers thicker than a few tens of nanometer, the plastic deformation can be assisted by mechanical advantage of dislocations pile-ups, in which the Hall-Petch relationship between flow stress σ and the thickness of layers L_m is available, i.e., $\sigma \propto L_m^{-1/2}$ [152]. This provides an opportunity for the Cu layer to achieve matched mechanical properties with amorphous ZrCu layer by changing its thickness. From our current experimental results, 100 nm appears to be the right thickness range for metallic Cu layers to reach the matched flow stress with that of amorphous ZrCu layer. For the metallic Cu layers with the thickness much lower than 100 nm, such as 10 or 20 nm, the confined layer slip (CLS) behavior would result in the stress scales much higher than that of amorphous ZrCu layers. In this case, the shear bands initiated in the ZrCu layers would pass through the whole specimens (based on the model by Cao and Evans) [151], resulting in compression instability, as observed in Figure 4.23. Otherwise, if the thickness of metallic Cu layers is much higher than 100 nm, such as 500 nm in this study, the ultra low flow stress of metallic Cu layers with respect to that of amorphous ZrCu layers would make the pillar deformation basically carried only by the Cu layers, leaving ZrCu unchanged, as observed in Figure 4.22.

To explain the unusual superplastic-like plasticity of the 100/100 nm ZrCu/Cu nanolayered micropillars, the relationship between of mechanical properties and thickness between metallic and amorphous layers is schematically illustrated in Figure 5.2. We can estimate the thickness range of metallic layers giving rise to a matched strength with that of the amorphous layers. For the current ZrCu amorphous layer, the yield stress is about 2-2.5 GPa (a sharp burst will initiate at ~2.6 GPa). With the concept of $\sigma \propto L_m^{-1/2}$ for the crystalline Cu metal layer, we can define a length scale range L_1 to L_2 for the Cu layer to possess a similar flow stress of 2.0-2.5 GPa. Based on our experience, L_1 and L_2 for the current case are about 80 and 150 nm, respectively. As demonstrated in Figure 5.2, the metal layer with a thickness less than 20 nm would lead to inhomogeneous deformation in both the amorphous and crystalline layers. The metal layer with a thickness between L_1 and L_2 (within the blue dashed square in Figure 5.2) would ensure matched flow stresses of the metal and amorphous layers, leading to co-plastic deformation of both layers. Coupled with the requirement based on foregoing analysis from Eqns. (5-7) to (5-9), namely, $L_a \leq L_m$, the optimum crystalline metal layer thickness should satisfy the relationship, $L_a \leq L_m \leq L_2$, as demonstrated in the shaded area in Figure 5.2. Under this condition, superplastic-like homogeneous and co-deformation mode to large strains is possible.

5-1-3 Interaction of amorphous/crystalline interface

For HCP metals such as titanium, zirconium, and magnesium, slip and twinning occur simultaneously in many cases and the resulting mechanical properties are strongly influenced by the twinning. In particular, even for FCC metals, such as Al, twinning becomes a preferred deformation mode if the grain size is refined to the nanoscale [153]. The formation of multiple twinning can prevent effectively the active dislocation slip and thus raise the work hardening rate. This should modify the stress concentration state of the amorphous/crystalline

interfaces. As a result, more compatible strain at the amorphous/crystalline interface is expected.

Based on the TEM observations (Figure 5.3), we propose a twinning-accommodation mechanism to explain the happening of co-deformation at the amorphous/crystalline interfaces. On the one hand, the preferential happening of the deformation planar defects (twins and stacking faults) in nano-scale grained Zr layer than activated dislocations can avoid the dislocation pile-ups formation at the amorphous/crystalline interfaces, as shown in Figure 5.3. Thus, the local stress concentrations at the amorphous/crystalline interfaces are suppressed. On the other hand, the high-strength crystalline layer are sufficient stiff to produce a large elastic restoring forces to counteract the nucleation of the surfaces steps required for extensive shear on the bands in the glass.

High-magnitude TEM images of the deformed laminates (Figure 5.3b and 5.3b) show that the no characteristic offset can be found at the amorphous/crystalline interfaces. To satisfy strain compatibility at the amorphous/crystalline interfaces, the nano-twinning governed deformation in the Zr crystalline layers must be matched by plastic flow in the amorphous layers. As the load is transferred to the elastically deformed glass and the local stress is raised high enough, plastic shear events are nucleated in the amorphous layers. At low temperatures, these shear transition zones (STZs) are nucleated in regions in which a critical amount of free volume is concentrated. The homogenously strain provided by twinning mode in the crystalline layers induces a fairly uniform distribution of shear events in the glass layers that provided accommodation of the macroshear banding. As described above, Figures 5.4(a) and 5.4(b) show the schematic illustration of interaction between amorphous/crystalline interfaces.

TEM images taken from the HCP nanocrystalline Zr region of the L3 pillar reveal the absence of dislocation storage or pileup except the presence of planar defects, i.e. deformation twins. A high resolution TEM lattice image is presented in Figure 5.5, which shows the presence of many nano-twins with several variants. The first one is the common twins with a twin habit K_1 plane of $(10\bar{1}2)$, and a twin shear direction η_1 of $[\bar{1}011]$. Note that Zr has a c/a ratio of 1.5892, less than the ideal 1.633, thus twinning is favorable to operate under compression [154]. In the sputtered Zr layer, the (0002) plane is lying parallel to the substrate, and the twinning undistorted $(10\bar{1}2)$ K_2 plane forms 42.53° with respect to (0002) , which is good accord with the expected shear band orientation in the amorphous ZrCu layer and the twinning operation mode in crystalline Zr layer. The shear strain for this $\{10\bar{1}2\}\langle\bar{1}011\rangle$ twinning mode can be 17%, which might be large enough to accommodate the observed severe plastic shear strain in the Zr layer. The second variant is the $\{11\bar{2}1\}\langle11\bar{2}\bar{6}\rangle$ twin system. This twin shear strain is much higher, reaching the level 63%, which is very high and thus very effective in accommodate the shear strain and energy of the incoming shear bands. The angle between the $\{0002\}$ planes in the matrix and the habit plane $\{11\bar{2}1\}$ planes is 68.93° , which is in good agreement with the high resolution TEM micrograph in Figure 4.18. The third variant is the $\{11\bar{2}2\}\langle11\bar{2}\bar{3}\rangle$ system, which produces a twinning shear strain of 23% and the angle between $\{0002\}$ and $\{11\bar{2}2\}$ is 57.49° . In the current case, the exact strain accommodation obviously must include a thorough statistic analysis of the occurrence frequency of these twin variants in pillars deformed to various strains, which will be our future task. Nonetheless, it is demonstrated that nanocrystalline Zr layer can act as a sink to effectively dissipate the kinetic energy carried by incident shear bands.

5-2 In-situ TEM compression tests

From the view point of energy while the shear band propagates, Volkert et al. [123]

demonstrated that the elastic strain energy of the column is decreased by an amount $\pi\sigma\epsilon r^2 h/2$ (where σ , ϵ , r , and h is stress, strain, pillar diameter, and shear band thickness) and the shear band energy is increased by an amount $(2^{1/2}\pi r^2 \Gamma)^{1/2}$, where Γ is the energy per unit area of shear band. When the shear band formation, equaling these two energy terms gives an estimate of the critical stress required for shear band formation, $\sigma = (2^{3/2} \Gamma E/h)^{1/2}$, where E is the Young modulus. Using the measured flow stress σ and a typical shear band thickness h of 10 nm gives $\Gamma=10 \text{ J/m}^2$. Using this value for Γ and $E = 110 \text{ GPa}$, the critical condition for shear band formation is estimated and the corresponding stress and pillar diameter is shown in [Figure 5.6](#). The upper and lower regions of the solid line in [Figure 5.6](#) represent the shear band formation and homogeneous deformation, respectively.

Based on this estimation, the deformation behavior of the current nanopillar is classified in the heterogeneous (shear-band) deformation region, as shown in [Figure 5.6](#). It provides another evidence to illustrate the high yielding strength ($\sim 2.5 \text{ GPa}$) and heterogeneous deformation can be achieved in the 140 nm ZrCu TFMGs nanopillars under uniaxial in-situ compression tests. This implies that as the pillar size decreases below 140 nm in diameter, the shear band deformation still dominates the deformation behavior of metallic glasses.

Plastic deformation in the nanopillars sample is noted to be local, occurs mainly in the upper portion of the sample. The change in cross-sectional area as a function of distance from the top of the pillar sample after being deformed 300 nm is shown in [Figure 5.7](#). Apparently, the dimension of the bottom part of the sample remains practically unchanged even after being compressed to a 300 nm displacement. It is primarily because metallic glasses are perfectly plastic material and the test sample is tapered. The strain localization near the top of the sample was additionally supported by the observation that the initial TEM contrast of the top part of the sample was brighter, resulting from a smaller diameter because tapering. After

compression, the top part of the pillar gradually became darker as a result of increasing diameter. It is especially noted in [Figure 4.31](#) that, despite the strain localization near the top of the sample, there is no evidence of localized shear across the sample. According to the conventional wisdom, one would seemingly draw a conclusion that the pillar was homogeneously deformed. This is, in fact, not the case. As demonstrated later in the simulation, shear band initiates from the contact corner between the sample and punch and form inverse cone with the tip of the cone located along the centerline of the compressive axis.

However, differing from SEM, which can offer 3-dimension morphology of a deformed pillar, TEM provides only a 2-dimension view. It is hard to detect the formation of individual shear band from the current TEM images. The difficulty is caused by the fact that not only because the width of a shear band is extra thin (~10-20 nm), requiring a high-resolution TEM for observation [\[155\]](#), but also because shear band propagation speed is extremely rapid (~4 mm/s) [\[156\]](#). It would take less than 0.1 ms to propagate a shear band through the entire pillar sample. However, the current TEM video speed is 13 frame/s, thus unable to capture shear bands.

In order to investigate the tapering effects on the shear band formation and deformation behavior, finite element simulations were performed using the free volume model [\[99\]](#). The simulation experiments were supported by Prof. Gao and Prof. Nieh in University of Tennessee. In this model, the plastic shear strain rate $\dot{\gamma}^p$ is given by the flow equation,

$$\frac{\partial \gamma^p}{\partial t} = 2\nu \exp\left(-\frac{1}{\bar{v}_f}\right) \exp\left(-\frac{\Delta G^m}{k_B T}\right) \sinh\left(\frac{\tau}{\tau_0}\right), \quad (5-10)$$

with the atomic vibration frequency ν , the normalized free volume \bar{v}_f , the activation energy ΔG^m , the reference stress τ_0 which depends on the atomic structure and temperature, the applied shear stress τ , the Boltzmann constant k_B and the absolute temperature T . The free volume evolves by a stress-driven creation process and a diffusion-dominated annihilation process. The latter requires a number of atomic jumps to annihilate the free volume, taken as 3 in this simulation. Our simulations are based on the nonlinear finite element method developed previously [157]. A 3D tapered pillar with the aspect ratio of 4 was constructed for simulation in ABAQUS with a total number of 38,401 C3D8 elements. A flat-ended indenter is used to apply the compressive load from the above while the sample bottom is completely clamped. The constitutive parameters were specified $\bar{v}_f = 0.05$, $E/\tau_0 = 240$, and Poisson's ratio of 0.333. The normalized loading rate $(\dot{L}/L_0)\exp(\Delta G^m/k_B T)$, can be calculated to be 2.5×10^{-6} , where \dot{L} is the strain rate and L_0 is original length of sample.

As a result of sample tapering, the stress distribution in the initial elastic stage of compression test is non-uniform. Usually for a material obeying classic continuum plasticity, the plastic zone will gradually extend from the pillar top to the entire sample, and the entire deformation history is smooth and continuous. The taper angle has insignificant effect on the final, barrel-like deformed shape. For metallic glasses, however, the scenario is radically different. Strain localization in the form of shear band is initiated near the pillar top because of the stress concentration. As shown in [Figure 5.8](#), these shear bands lead to a drastic increase of the cross-sectional area although the absolute strain level is generally small except in the shear bands. The shear bands are formed inside the pillar and therefore are not observable from outside. In contrast to the catastrophic failure in large pillar compression tests, these shear bands will not evolve into cracks because the taper angle results into a geometric hardening effect. The comparison between the simulations and experiments indicate a significant effect of the taper angle, so that the deformation becomes highly

localized near the top and the resulting force-displacement curve cannot be directly and easily translated to the constitutive behavior of the material. It is also noted that our predicted area change ratio is much larger than experiments, which is mainly due to the misalignment-induced bending in experiments that accommodates the compressive displacement. Nevertheless, the functional trend for both experiment and simulation are similar.

5-3 Interface strength of the inclined multilayer pillars

The magnitude of interface energy plays an essential role in determining the mechanical response of a lot of advanced composited materials and has attracted great attention in both experimental investigation and theoretical prediction, and many in-depth researches have been done on the metal/metal and metal/ceramics composites [158-160]. It has found that besides the strong metal/metal interfaces, the clean metal/ceramics interfaces devoid of reaction products are also inherently tough and ductile with the interface energy of several joules per meter square despite of the greater chemical bonding difference of the two materials [161]. From these remarkable findings, it is expected that high interfacial adhesion can be achieved if clean interfaces are fabricated.

Recently, in an attempt to apply the amorphous metals in thin film coatings and micro-electro-mechanical systems (MEMS) devices, several efforts have been made to explore the high-performance nanolaminated amorphous/crystalline composites [55, 61, 131, 147]. And For the amorphous–crystalline multilayers with the individual layer thickness in the nanometer range, great progress has been obtained in demonstrating large plasticity both in tension and compression [55, 61, 131, 147]. The amorphous–crystal interfaces are assumed to be inherently strong and exhibit unique inelastic shear (slip) transfer characteristics [55,

61]. However, no interface energy has been evaluated so far, which is thought to be critical to determine the stability of the interfaces during the deformation process. In this paper, by using a well-established model, the interface energy of as-sputtered amorphous ZrCu/crystalline Zr multilayered composites is calculated, and the calculated results are compared with measured mechanical response of the ZrCu/Zr micropillars with 45° inclined interfaces.

The interface energy γ is the excess energy per unit area of a system owing to the appearance of the interface, and it is stemmed from the change in the interfacial atomic chemical bonding and structural strain at the interface, i.e., γ compose of the chemical interface energy γ_c and the structural interface energy γ_s . Based on the model of Liang et al. [162], the size-dependent chemical interface energy between two materials can be expressed as

$$\gamma_c = \frac{2}{3R} \left[\frac{h_1 S_{v1} H_{m1}}{V_{m1}} \left(1 - \frac{h_1}{2D}\right) + \frac{h_2 S_{v2} H_{m2}}{V_{m2}} \left(1 - \frac{h_2}{2D}\right) \right], \quad (5-11)$$

where R is the ideal gas constant, h_1 and h_2 are the atomic diameters of the involved materials (0.361 nm for ZrCu and 0.412 nm for Zr), S_v is the vibrational part of the melting entropy for metals ($S_v = H_m / T_m$, where H_m is the melting enthalpy, and T_m is the melting temperature, S_v is calculated to 11.84 J/mol*K), and V_m is the molar volume of the solids (10.57 cm³/mol for ZrCu and 14.02 cm³/mol for Zr). For interfaces of two thin films, $D = t_1 + t_2$ denotes the total thickness, t_1 and t_2 are the thickness of the two materials, respectively. For the ZrCu part of interface, the physical parameter can be obtained by taking the average value of Zr and Cu owing to their equal-mole contents. Thus, for the amorphous ZrCu/metallic crystalline Zr with 500 nm thickness for each layer, the chemical interface energy is calculated to be $\gamma_c =$

1.1 J/m². This calculated chemical interface energy is very close to that of metal/metal interface, such as Ag/Ni interface [163].

On the other hand, owing to the amorphous nature of the ZrCu layer, the structure interface energy caused by the lattice mismatch between amorphous ZrCu and crystalline Zr should be evaluated. Based on the model of Liang et al. [162], the bulk solid-solid structural interface energy can be expressed as:

$$\gamma_s = \frac{G_1 G_2 b \varepsilon_0}{4\pi[(1-\nu_1)G_2 + (1-\nu_2)G_1]} \left[\ln\left(\frac{D}{2b}\right) + 1 \right] \times \left(1 - \frac{\varepsilon}{\varepsilon_0}\right), \quad (5-12)$$

where G is the shear modulus (37 GPa for ZrCu and 45 GPa for Zr), b is the average Burgers vector or defect displacement unit (estimated to be around 1 nm for the ZrCu/Zr system), $\varepsilon_0 = (h_2 - h_1)/h_1$ is the misfit strain (where h_1 and h_2 are the effective glide plane spacings, and ε_0 is calculated to be 0.141), and ν is the Poisson's ratio (0.35 for ZrCu and 0.34 for Zr). Further, the mismatch induced strain ε is given by

$$\varepsilon = -\frac{2\kappa f}{3D}, \quad (5-13)$$

where κ is the compressibility and $\kappa = 1/B$, where B is the volume modulus and taken as the average value of the two materials, namely, 111 GPa for ZrCu and 125 GPa for Zr, or 118 GPa in average. It follows that κ is equal to $8.47 \times 10^{-3} \text{ GPa}^{-1}$. And ε is size-dependence due to the corresponding bulk materials based on the Laplace-Young equation and isotropic assumption [163, 164]. The expression of the intrinsic interface stress f has been derived as [163, 164]:

$$f = -[(3\gamma_m D_0)/(8\kappa)]^{1/2}, \quad (5-14)$$

where the negative sign shows the compressive interface stress, γ_m is the solid-liquid interface energy, and D_0 is the critical size, $D_0=2h$ (equal to 0.776 nm) for the thin films [164]. Here, based on the Gibbs-Thomson equation, the solid-solid interface energy γ_m can be expressed by:

$$\gamma_m = 4hS_v H_m / (3V_m R). \quad (5-15)$$

By taking the average value of two materials of γ_m ($\sim 1.1 \text{ J/m}^2$) and D_0 (0.776 nm), the structural interface energy of ZrCu/Zr can be calculated. From Eqn. (2), the structural interface energy γ_s for the amorphous ZrCu/metallic crystalline Zr, with 500 nm thickness for each layer, is calculated to be $\gamma_s = 2.9 \text{ J/m}^2$. Hence, combining Eqns. (1) and (2), the total amorphous ZrCu/crystalline Zr interface energy γ is calculated to be $\gamma = \gamma_c + \gamma_s = 4.0 \text{ J/m}^2$.

Similar to that of the inherently strong metal/ceramic interfaces [158-160], the interface energy of amorphous ZrCu/metallic crystalline Zr interfaces also resides several joules per meter square, implying that the stability of as sputtered metallic amorphous/crystalline interfaces is also inherently strong and thus it is difficult for the interface to separate during loading. This has been evidenced by the mechanical response of ZrCu/Zr or ZrCu/Cu nanolaminated thin films [55, 131, 147] under tension and compression. The interfaces were observed to be strong and maintain homogeneous-like deformation during the whole straining process.

Till now, the nature of strengths and fracture resistances of interfaces between metallic glasses and metallic crystals are still not fundamentally understood. However, the currently

calculated data on interface energy of the ZrCu/Zr multilayers is very close to that of the pure metals/ceramics interfaces [158-160]. The current results show that the bonding characteristics of metallic glasses and metallic crystals have significant influence on its interface energy due to the greater chemical and structural bonding differences of the two materials. It is well known that the atomic arrangement of the amorphous ZrCu material is random (i.e., no periodicity). Each atom in the amorphous ZrCu layer has different nearest neighbors and coordinate number (CN) despite of the fact that it is difficult to define the nearest neighbor distances or the CNs [165]. Thus, to some extent, the as-sputtered ZrCu amorphous thin film can be regarded as a uniform mixture composing of interpenetrated Zr and Cu atoms. This will result in the great chemical bonding difference and structural mismatch at the interface of the two materials.

The rough theoretical estimations of the interface energy ($\gamma \sim 4.1 \text{ J/m}^2$) and the experimental mechanical responses ($\tau_i > 1.5 \text{ GPa}$) of the amorphous ZrCu/crystalline Zr nanolaminates with 45° inclined interfaces support that the amorphous/metals interface is inherently strong. Similar researches on the metal/ceramics have shown that the clean interfaces devoid of reaction products are inherently tough and ductile. Such high adhesion is realized even though the metals are polycrystalline and non-epitaxial: that is, despite the interfaces being either incoherent or subject to a high density of misfit dislocations [9]. The clean interfaces can be provided by using rigorous processing practices that exclude contaminants during bonding. In the current study, sputtering is a right way in producing such clean interfaces for ZrCu/Zr multilayered materials.

As to the shear fracture mechanism within the Zr layer, some reasonable prostitution can be given. Our observations on the as-sputtered Zr samples with different thickness by using transmission electron microscopy (TEM) have shown that the grain sizes of the sputtered Zr

all fall into a range from ten to several decades nanometer (with an average of 30 ± 10 nm). It is conceivable that such nano-scale grains can make it possible for a large group of grains to quickly develop the texturing favorable for slip propagation in a cooperative manner, facilitating the localization of the plastic deformation. Many similar studies have also shown that due to the lack of strain hardening in metals with nano-scale grains, the strong materials is likely to develop the shear banding instability (i.e., localized shearing) under certain loading sample conditions [166, 167].

Chapter 6 Conclusions

According to the present study, some major points and important conclusions on the mechanical properties and deformation behaviors of the monolithic ZrCu TFMGs and the amorphous/crystalline multilayer micropillars are summarized below.

1. The presence of a nanocrystalline Zr layer of sufficient thickness (above 500 nm) can effectively absorb the kinetic energy of the shear bands developed in the ZrCu amorphous layer. The arresting and blocking effect for the incoming shear band by the Zr nanocrystalline layer could result in ductile plastic deformation of the ZrCu metallic glass to a high strain level over 50%. For the results of 100/100 nm multilayer pillar, shear band initiated in the ZrCu layer passes through the Zr layer. In the nanocrystalline Zr layer, the nano-twinning plastic deformation mode is responsible for the accommodation mechanism of the incident high-energy shear bands.
2. The brittle problem of an amorphous coating can be alleviated by percolating with a nanocrystalline Zr metallic underlayer. However, the metallic underlayer must have a similar strength, be sufficiently thick, to be able to absorb the kinetic energy of the incident shear bands. The critical thickness of the crystalline layer would be dependent upon relatively strength of the amorphous and crystalline layers.
3. The deformation behaviors for metallic glass thin films can be controlled by certain thickness ratios of amorphous versus nanocrystalline layers. For the same thick ratio of ZrCu/Zr and ZrCu/Mo multilayer samples, inhomogeneous deformation can be seen easily. In term of ZrCu/Cu, these results suggest that the plasticity of amorphous alloy

can be improved significantly with the addition of copper layer.

4. To design superplastic-like amorphous/crystalline nanolayered micropillars, we should choose the inherently ductile amorphous forming alloys (such as Zr-, Pd-base alloys) as well as soft pure metals (such as Cu, Al, Ag, Au, Pd) with high deformation capacity in room temperature. Beside, the two basic principles should be followed: (1) modulating the thickness of metal layers to ensure their flow stress of metallic layers matched with that of amorphous layers ($L_1 \leq L_m \leq L_2$); (2) presetting the thickness of amorphous layers equal or less than that of the metallic layers ($L_a \leq L_m$). Based on the two principles, we can derive a definite criterion, $L_a \leq L_m \leq L_2$, for various amorphous/crystalline multilayers to deform plastically.
5. According to the in situ TEM results, it is found that inhomogeneous deformation prevails down to 140 nm pillars. If homogeneous deformation should dominate at small scales, localized deformation near the tip of the tapered pillars would not have occurred. Both taper angle and tip rounding do not change the general deformation behavior, while the degrees of deformation localization depend on these two parameters.
6. Based on the simulation and experiment findings, the in situ compressive test of the ZrCu tapered pillar samples is not a viable technique for the identification of the transition from inhomogeneous to homogeneous deformation modes in metallic glasses. The nanopillar is 140 nm in diameter and with a taper angle of 3° . Experimental observations and simulations based on a free-volume model both demonstrate that the deformation is localized near the top of the tapered metallic glass pillar. Localized shear bands appear to be absent, but they form inside the tapered samples.

7. The interface nature of metallic glass ZrCu/crystalline Zr is characterized through evaluating its energy and validated by the mechanical response of micropillar with $\sim 45^\circ$ inclined interface under compression. The rough theoretical estimations of the interface energy ($\gamma \sim 4.1 \text{ J/m}^2$) and the experimental mechanical responses ($\tau_i > 1.5 \text{ GPa}$) of the amorphous ZrCu/crystalline Zr nanolaminates with 45° inclined interfaces support that the amorphous/metals interface is inherently strong. This result provides some useful physical data in designing safe metallic amorphous/crystalline thin film coatings and MEMS devices.

Chapter 7 Prospective and future work

In order to extend the present study, some future research directions of the deformation behaviors on monolithic TFMGs and amorphous/crystalline multilayer structure are suggested as follows:

1. The traces of shear bands initiated from amorphous layers are not observed in the present study by TEM. Shear band propagation plays a key role for the improvement on the plasticity of TFMGs. The way to observe the traces of shear bands within the amorphous layer is a crucial issue. If it can be carried out, it will be helpful to demonstrate the interaction between the amorphous/crystalline interfaces.
2. In addition to current results of ZrCu/Cu pillars, the systemic ZrCu/Cu laminates at variant thicknesses, such as 200/200 or 50/50 nm, will be developed. It will help us to have the remarkable results and complete the whole study.
3. For the in situ nanocompression test, the tapering effect is considered in this study. In the future, the geometric effects of nanopillar samples, such as dome-shaped top, should be further investigated and explored. The effect on misalignment between the sample axis and the compressive axis will also be considered in the further study.

References

- [1] A. C. Lund and C. A. Schuh, *J. Appl. Phys.*, **95**, 4815-4822 (2004)
- [2] <http://www.liquidmetal.com>.
- [3] W. L. Johnson, *MRS Bull.*, **24**, 42-56 (1999)
- [4] A. Inoue, B. Shen, H. Koshiba, H. Kato, and A. R. Yavari, *Nature Mater.*, **2**, 661-663 (2003)
- [5] N. H. Pryds, *Mater. Sci. Eng. A*, 186-193 (2002)
- [6] A. Inoue, *Acta Mater.*, **48**, 279-306 (2000)
- [7] W. Klement, R. H. Willens, and P. Duwez, *Nature*, **187**, 869-870 (1960)
- [8] 吳學陞, *工業材料*, **149**, 154-165 (1999)
- [9] H. S. Chen and D. Turnbull, *J. Chem. Phys.*, **48**, 2560-2571 (1968)
- [10] H. S. Chen and D. T. Turnbull, *Acta Metall.*, **17**, 1021-1031 (1969)
- [11] H. S. Chen and C. E. Miller, *Rev. Sci. Instrum.*, **41**, 1237-1238 (1970)
- [12] H. S. Chen, *Acta Metall.*, **22**, 1505-1511 (1974)
- [13] A. J. Drehman, A. L. Greer, and D. Turnbull, *Appl. Phys. Lett.*, **41**, 716-717 (1982)
- [14] H. W. Kui, A. L. Greer, and D. Turnbull, *Appl. Phys. Lett.*, **45**, 615-616 (1984)
- [15] A. Inoue, T. Zhang, and T. Masumoto, *Mater. Trans. JIM*, **31**, 425-428 (1990)
- [16] A. Inoue, T. Nakamura, and N. Nishiyama, *Mater. Trans. JIM*, **33**, 937-945 (1992)
- [17] A. Inoue, T. Zhang, N. Nishiyama, K. Ohba, and T. Masumoto, *Mater. Trans. JIM*, **34**, 1234-1237 (1993)
- [18] A. Peker and W. L. Johnson, *Appl. Phys. Lett.*, **63**, 2342-2344 (1993)
- [19] A. Inoue, N. Nishiyama, and H. Kimura, *Mater. Trans. JIM*, **38**, 179-183 (1997)
- [20] H. Ma, L. L. Shi, J. Xua, Y. Li, and E. Ma, *Appl. Phys. Lett.*, **87**, 181915 (2005)
- [21] W. H. Wang, C. Dong, and C. H. Shek, *Mater. Sci. Eng. R*, **44**, 45-89 (2004)
- [22] J. F. Loffler, *Intermetallics*, **11**, 529-540 (2003)
- [23] T. Masumoto and R. Maddin, *Mater. Sci. Eng.*, **19**, 1-24 (1975)

- [24] R. B. Schwarz, *Mater. Sci. Eng.*, **97**, 71-78 (1988)
- [25] G. Minnigerode, A. Regenbrecht, and K. Samwer, *Z. Phys. Chem. Neue Folge, Bd.*, **157**, 197-201 (1988)
- [26] A. Regenbrecht, G. Minnigerode, and K. Samwer, *Z. Phys. B: Condensed Matter.*, **79**, 25-31 (1990)
- [27] S. Eickert, H. Hecht, and G. Minnigerode, *Z. Phys. B: Condensed Matter.*, **88**, 35-38 (1992)
- [28] J. Dudonis and R. Bruèas, *Proc. Conf. Physics and Technology of Plasma*, 269-272 (1994)
- [29] Y. Liu, S. Hata, K. Wada, and A. Shimokohbe, *Jpn. J. Appl. Phys.*, **40**, 5382-5388 (2001)
- [30] P. Sharma, W. Zhang, K. Amiya, H. Kimura, and A. Inoue, *J. Nanosci. Nanotechnol.*, **5**, 416-420 (2005)
- [31] T. Fukushige, S. Hata, and A. Shimokohbe, *J. Microelectromech. Syst.*, **14**, 243-253 (2005)
- [32] J. Dudonis, R. Brucas, and A. Miniotas, *Thin Solid Films*, **275**, 164-167 (1996)
- [33] C. J. Chen, J.C. Huang, H.S. Chou, Y.H. Lai, L.W. Chang, X.H. Du, J.P. Chu, and T. G. Nieh., *J. Alloys Compd.*, (2008)
- [34] S. Hata, K. Sato, and A. Shimokohbe, *Proc. SPIE*, 97-108 (1999)
- [35] S. Hata, Y. Liu, T. Kato, and A. Shimokohbe, *10th ICPE*, 37 (2001)
- [36] Y. Liu, S. Hata, K. Wada, and A. Shimokohbe., *MEMS, 18th IEEE International Conference*, (2001)
- [37] A. Inoue, H. Yamaguchi, T. Zhang, and T. Masumoto, *Mater. Trans., JIM*, **31**, 104 (1990)
- [38] H. M. Chen, Y. C. Chang, T. H. Hung, X. H. Du, J. C. Huang, J. S. C. Jang, and P. K. Liaw, *Mater. Trans.*, **48**, 1802-1805 (2007)

- [39] C. P. Chou and F. Spaepen, *Acta Metall.*, **23**, 609-613 (1975)
- [40] G. Y. Yuan and A. Inoue, *J. Alloys Compd.*, **387**, 134-138 (2005)
- [41] Z. G. Li, X. Hui, C. M. Zhang, and G. L. Chen, *J. Alloys Compd.*, **454**, 168-173 (2008)
- [42] G. Y. Yuan, K. Amiya, and A. Inoue, *J. Non-Cryst. Solids*, **351**, 729-735 (2005)
- [43] C. Fan, P. K. Liaw, T. W. Wilson, H. Choo, Y. F. Gao, C. T. Liu, T. Proffen, and J. W. Richardson, *Appl. Phys. Lett.*, **89**, 231920 (2006)
- [44] G. He, W. Loser, J. Eckert, and L. Schultz, *Mater. Sci. Eng. A*, **352**, 179-185 (2003)
- [45] S. W. Lee, M. Y. Huh, E. Fleury, and J. C. Lee, *Acta Mater.*, **54**, 349-355 (2006)
- [46] T. Mukai, T. G. Nieh, Y. Kawamura, A. Inoue, and K. Higashi, *Intermetallics*, **10**, 1071-1077 (2002)
- [47] W. J. Wright, R. B. Schwarz, and W. D. Nix, *Mater. Sci. Eng. A*, **319-321**, 229-232 (2000)
- [48] D. M. Xing, T. H. Zhang, W. H. Li, and B. C. Wei, *J. Alloys Compd.*, **433**, 318-323 (2007)
- [49] J. Schroers and W. L. Johnson., *Phys. Rev. Lett.*, **93**, 255506 (2004)
- [50] Y. H. Liu, G. Wang, R. J. Wang, D. Q. Zhao, M. X. Pan, and W. H. Wang, *Science*, **315**, 1385-1388 (2007)
- [51] X. H. Du, J. C. Huang, K. C. Hsieh, Y. H. Lai, H. M. Chen, J. S. C. Jang, and P. K. Liaw, *Appl. Phys. Lett.*, **91**, 131901 (2007)
- [52] D. W. Kum, T. Oyama, J. Wadsworth, and D. Sherby, *J. Mech. Phys.*, **31**, 173-186 (1983)
- [53] C. K. Yoon and I. W. Chen, *J. Am. Ceram. Soc.*, **73**, 1555-1565 (1990)
- [54] B. C. Snyder, J. Wadsworth, and O. D. Sherby, *Acta Metall.*, **32**, 919-932 (1984)
- [55] T. G. Nieh, T. W. Barbee, and J. Wadsworth, *Scripta Mater.*, **41**, 929-935 (1999)
- [56] A. Donohue, F. Spaepen, R. G. Hoagland, and A. Misra, *Appl. Phys. Lett.*, **91**, 3

(2007)

- [57] C. C. Hays, C. P. Kim, and W. L. Johnson, *Phys. Rev. Lett.*, **84**, 2901-2904 (2000)
- [58] G. He, J. Eckert, W. Loser, and L. Schultz, *Nature Mater.*, **2**, 33-37 (2003)
- [59] D. H. Hofmann, D. C., J. Y. Suh, A. Wiest, M. L. Lind, M. D. Demetriou, and W. L. Johnson, *Proc. Natl. Acad. Sci. U.S.A.*, **105**, 20136-20140 (2008)
- [60] D. C. Hofmann, J. Y. Suh, A. Wiest, G. Duan, M. L. Lind, M. D. Demetriou, and W. L. Johnson, *Nature*, **451**, 1085-U3 (2008)
- [61] Y. M. Wang, J. Li, A. V. Hamza, and J. T. W. Barbee, *Proc. Natl. Acad. Sci. U.S.A.*, **104**, 11155-11160 (2007)
- [62] D. Pan, S. Kuwano, T. Fujita, and M. W. Chen, *Nano Lett.*, **7**, 2108-2111 (2007)
- [63] K. F. Yao, F. Ruan, Y. Q. Yang, and N. Chen, *Appl. Phys. Lett.*, **88**, (2006)
- [64] K. L. Chopra, ed. *Thin Film Phenomena*. 1985, McGraw-Hill, New York, USA.
- [65] P. J. Hsieh, PhD Thesis, *Nanocrystallization and Amorphization of Zr Base Alloys during Accumulative Roll Bonding*, National Sun Yat-Sen University, Kaohsiung, Taiwan., (2004)
- [66] W. Buckel, *Z. Phys.*, **138**, 136 (1954)
- [67] E. J. Cotts, W. J. Meng, and W. L. Johnson, *Phys. Rev. Lett.*, **57**, 2295-2298 (1986)
- [68] P. S. Grant, *Prog. in Mater. Sci.*, **39**, 497-545 (1995)
- [69] B. Li, N. Nordstrom, and E. J. Lavernia, *Mater. Sci. Eng. A*, **237**, 207-215 (1997)
- [70] R. S. Liu, J. Y. Li, K. J. Dong, C. X. Zheng, and H. R. Liu, *Mater. Sci. Eng. B*, **94**, 141-148 (2002)
- [71] C. R. M. Afonso, C. Bolfarini, C. S. Kiminami, N. D. Bassim, M. J. Kaufman, M. F. Amateau, T. J. Eden, and J. M. Galbraith, *J. Non-Crystalline Solids*, **284**, 134-138 (2001)
- [72] M. S. El-Eskandarany and A. Inoue, *Metall. Mater. Trans. A*, **33**, 135-143 (2002)
- [73] C. C. Koch, O. B. Kavin, C. G. Mckamey, and J. O. Scarbrough, *Appl. Phys. Lett.*, **43**,

1017-1019 (1983)

- [74] Y. Saito, H. Utsunomiya, N. Tsuji, and T. Sakai, *Acta Mater.*, **47**, 579-583 (1999)
- [75] Z. P. Xing, S. B. Kang, and H. W. Kim, *Metall. Mater. Trans. A*, **33A**, 1521-1530 (2002)
- [76] J. Lee, F. Zhou, K. H. Chung, N. J. Kim, and E. J. Lavernia, *Metall. Mater. Trans. A*, **32**, 3109-3115 (2001)
- [77] A. Sagel, H. Sieber, H. J. Fecht, and J. H. Perepezko, *Acta Mater.*, **46**, 4233-4241 (1998)
- [78] D. Turnbull, *Contemp. Phys.*, **10**, 473-488 (1969)
- [79] M. Sasd and M. Poulain, *Mater. Sci. Forum*, **19-20**, 11-18 (1987)
- [80] I. W. Donald and H. A. Davies, *J. Non-Crystalline Solids*, **30**, 77-85 (1978)
- [81] O. N. Senkov and D. B. Miracle, *Mater. Res. Bull.*, **36**, 2183-2198 (2001)
- [82] Z. J. Yan, J. F. Li, S. R. He, and Y. H. Zhou, *Mater. Res. Bull.*, **38**, 681-689 (2003)
- [83] T. H. Hung, J. C. Huang, J. S. C. Jang, and S. C. Lu, *Mater. Trans.*, **48**, 239-243 (2007)
- [84] W. Chen, Y. Wang, J. Qiang, and C. Dong, *Acta Mater.*, **51**, 1899-1907 (2003)
- [85] Q. Wang, Y. M. Wang, J. B. Qiang, X. F. Zhang, C. H. Shek, and C. Dong, *Intermetallics*, **12**, 1229-1232 (2004)
- [86] Y. M. Wang, W. P. Xu, J. B. Qiang, C. H. Wong, C. H. Shek, and C. Dong, *Mater. Sci. Eng. A*, **375-377**, 411-416 (2004)
- [87] M. Iqbal, W. S. Sun, H. F. Zhang, J. I. Akhter, and Z. Q. Hu, *Mater. Sci. Eng. A*, **447**, 167-173 (2007)
- [88] Y. T. Cheng, MS Thesis, *Amorphization and Nanocrystallization Behavior in Mg-Cu-Y Alloy by Adding Boron*, National Sun Yat-Sen University, Kaohsiung, Taiwan., (2005)
- [89] A. Inoue, *Mater. Trans. JIM*, **36**, 866-875 (1995)

- [90] A. Inoue, A. Takeuchi, and T. Zhang, *Metall. Mater. Trans. A*, **29**, 1779-1793 (1998)
- [91] A. Inoue and K. Hashimoto, *Amorphous and Nanocrystalline Materials: Preparation, Properties, and Applications*, Springer-Verlag, Berlin and Heidelberg., (2001)
- [92] A. Takeuchi and A. Inoue, *Mater. Trans.*, **41**, 1372-1378 (2000)
- [93] D. M. Mattox, *Handbook of Physical Vapor Deposition (PVD) Processing*, (1998)
- [94] M. Ohring, *Materials Science of Thin Film*, Academic press., (1992)
- [95] K. Wasa and S. Hayakawa, *Handbook of Sputter Deposition Technology*, (1992)
- [96] S. Veprek and M. Heintz, *Plas. Chem. Plas. Proc.*, **10**, 3-26 (1990)
- [97] S. Veprek and M. G. J. Veprek-Heijman, *Appl. Phys. Lett.*, **56**, 1766-1768 (1990)
- [98] Y. Liu, S. Hata, K. Wada, and A. Shimokohbe, 14th IEEE International Conference on Micro Electro Mechanical Systems, Interlaken, Switzerland, 102-105 (2001)
- [99] F. Spaepen, *Acta Metall.*, **25**, 407-415 (1977)
- [100] A. S. Argon, *Acta Metall.*, **27**, 47-58 (1979)
- [101] L. H. Dai, M. Yan, L. F. Liu, and Y. L. Bai, *Appl. Phys. Lett.*, **87**, 141916 (2005)
- [102] G. P. Zhang, Y. D. Liu, and B. Zhang, *Adv. Eng. Mater.*, **7**, 606-609 (2005)
- [103] C. Suryanarayana, A. Inoue, and T. Masumoto, *J. Mater. Sci.*, **15**, 1993-2000 (1980)
- [104] T. G. Park, S. Yi, and D. H. Kim, *Scripta Mater.*, **43**, 109-114 (2000)
- [105] S. Pang, T. Zhang, K. Asami, and A. Inoue, *Mater. Trans.*, **42**, 376 (2001)
- [106] M. D. Uchic, D. M. Dimiduk, J. N. Florando, and W. D. Nix, *Science*, **305**, 986-989 (2004)
- [107] H. Zhang, B.E. Schuster, Q. Wei, and K. T. Ramesh, *Scripta Mater.*, **54**, 181-186 (2006)
- [108] J. R. Greer, W. C. Oliver, and W. D. Nix, *Acta Mater.*, **53**, 1821-1830 (2005)
- [109] E. M. Savitskii and A. Prince, E. M. Savitskii and A. Prince. *Handbook of precious metals. Hemisphere publications*, New York, (1969). (1969)
- [110] C. A. Volkert and E. T. Lilleodden, *Philos. Mag.*, **86**, 5567-5579 (2006)

- [111] M. D. Uchic, D. M. Dimiduk, R. Wheeler, P. A. Shade, and H. L. Fraser, *Scripta Mater.*, **54**, 759-764 (2006)
- [112] B. E. Schuster, Q. Wei, H. Zhang, and K. T. Ramesh, *Appl. Phys. Lett.*, **88**, 103112 (2006)
- [113] H. Bei, S. Shim, E. P. George, M. K. Miller, E. G. Herbert, and G. M. Pharr, *Scripta Mater.*, **57**, 397-400 (2007)
- [114] B. E. Schuster, Q. Wei, M. H. Ervin, S. O. Hruszkewycz, M. K. Miller, T. C. Hufnagel, and K. T. Ramesh, *Scripta Mater.*, **57**, 517-520 (2007)
- [115] C. J. Lee, J. C. Huang, and T. G. Nieh, *Appl. Phys. Lett.*, **91**, 161913 (2007)
- [116] Y. H. Lai, C. J. Lee, Y. T. Cheng, H. S. Chou, H. M. Chen, X. H. Du, C. I. Chang, J. C. Huang, S. R. Jian, J. S. C. Jang, and T. G. Nieh, *Scripta Mater.*, **58**, 890-893 (2008)
- [117] W. L. Johnson and K. Samwer, *Phys. Rev. Lett.*, **95**, (2005)
- [118] M. Zink, K. Samwer, W. L. Johnson, and S. G. Mayr, *Phys. Rev. B*, **73**, (2006)
- [119] T. G. Nieh and J. Wadsworth, *Scripta Mater.*, **54**, 387-392 (2006)
- [120] H. M. Chen, J. C. Huang, S. X. Song, T. G. Nieh, and J. S. C. Jang, *Appl. Phys. Lett.*, **94**, (2009)
- [121] D. C. Jang, C. T. Gross, and J. R. Greer, *Int. J. Plast.*, **27**, 858-867 (2011)
- [122] F. Shimizu, S. Ogata, and J. Li, *Acta Mater.*, **54**, 4293-4298 (2006)
- [123] C. A. Volkert, A. Donohue, and F. Spaepen, *J. Appl. Phys.*, **103**, (2008)
- [124] C. Q. Chen, Y. T. Pei, and J. T. M. De Hosson, *Acta Mater.*, **58**, 189-200 (2010)
- [125] C. Q. Chen, Y. T. Pei, O. Kuzmin, Z. F. Zhang, E. Ma, and J. T. M. De Hosson, *Phys. Rev. B*, **83**, (2011)
- [126] B. E. Schuster, Q. Wei, T. C. Hufnagel, and K. T. Ramesh, *Acta Mater.*, **56**, 5091-5100 (2008)
- [127] A. Dubach, R. Raghavan, J. F. Loffler, J. Michler, and U. Ramamurty, *Scripta Mater.*, **60**, 567-570 (2009)

- [128] X. L. Wu, Y. Z. Guo, Q. Wei, and W. H. Wang, *Acta Mater.*, **57**, 3562-3571 (2009)
- [129] X. Chu and S. A. Barnett, *J. Appl. Phys.*, **77**, 4403-4411 (1995)
- [130] D. Tench and J. White, *Metall. Trans.*, **15**, 2039 (1984)
- [131] A. Donohue, F. Spaepen, R. G. Hoagland, and A. Misra, *Appl. Phys. Lett.*, **91**, 241905 (2007)
- [132] P. Sharma, K. Yubuta, H. Kimura, and A. Inoue, *Phys. Rev. B*, **80**, (2009)
- [133] S. Y. Kuan, H. S. Chou, M. C. Liu, X. H. Du, and J. C. Huang, *Intermetallics*, **18**, 2453-2457 (2010)
- [134] M. E. Launey, D. C. Hofmann, W. L. Johnson, and R. O. Ritchie, *Proc. Natl. Acad. Sci. USA*, **106**, 4986-4991 (2009)
- [135] M. Y. He and J. W. Hutchinson, *J. Appl. Mech.-Trans. of the Asme*, **56**, 270-278 (1989)
- [136] A. C. Fischer-Cripps, *Vacuum*, **58**, 569-585 (2000)
- [137] E. C. G. Kirk, D. A. Williams, and H. Ahmed, *Inst. Phys. Conf. Ser.*, **100**, 501-506 (1989)
- [138] M. H. F. Overwijk, F. C. van den Heuvel, and C. W. T. Bulle-Lieuwma, *J. Vac. Sci. Technol.*, **B11**, 2021-2024 (1993)
- [139] R. M. Langford and A. K. Petford-Long, *J. Vac. Sci. Technol.*, **A19**, 2186-2193 (2001)
- [140] <http://www.omniprobe.com/>.
- [141] C. J. Chen, *Master Thesis, Preparation and Characterization of Sputtered Zr-Ti and Zr-Cu Thin Film Metallic Glasses*. 2007, National Sun Yat-Sen University, Kaohsiung, Taiwan.
- [142] W. C. Oliver and G. M. Pharr, *J. Mater. Res.*, **7**, 1564-1583 (1992)
- [143] D. Pan, S. Kuwano, T. Fujita, and M. W. Chen, *Nano Lett.*, **7**, 2108-2111 (2007)
- [144] Y.F. Shen, L. Lu, Q. H. Lu, Z. H. Jin, and K. Lu, *Scripta Mater.*, **52**, 989-994 (2005)
- [145] I. C. Lin, *Master Thesis, Deformation Mechanism and Shear Banding Behavior in*

Amorphous/Nanocrystalline Multilayer System. 2010, National Sun Yat-Sen University, Kaohsiung, Taiwan.

- [146] Y. P. Li, J. Tan, and G. P. Zhang, *Scripta Mater.*, **59**, 1226-1229 (2008)
- [147] M. C. Liu, J. C. Huang, H. S. Chou, Y. H. Lai, C. J. Lee, and T. G. Nieh, *Scripta Mater.*, **61**, 840-843 (2009)
- [148] R. D. Conner, W. L. Johnson, N. E. Paton, and W. D. Nix, *J. Appl. Phys.*, **94**, 904-911 (2003)
- [149] R. D. Conner, Y. Li, W. D. Nix, and W. L. Johnson, *Acta Mater.*, **52**, 2429-2434 (2004)
- [150] M. A. Meyers and K. K. Chawla, *Mechanical Metallurgy: Principles and Applications*. 1984, New Jersey: Prentice-Hall, Englewood. .
- [151] H. C. Cao and A. G. Evans, *Acta Metall.*, **39**, 2997-3005 (1991)
- [152] A. Misra, M. J. Demkowicz, J. Wang, and R. G. Hoagland, *Jom-U.S.*, **60**, 39-42 (2008)
- [153] X. Z. Liao, F. Zhou, E. J. Lavernia, D. W. He, and Y. T. Zhu, *Appl. Phys. Lett.*, **83**, 5062-5064 (2003)
- [154] R. E. Reed-Hill, R. Abbaschian, *Physical Metallurgy Principles*. 3rd ed., PWS publications, Boston, (1994),
- [155] M. W. Chen, A. Inoue, W. Zhang, and T. Sakurai, *Phys. Rev. Lett.*, **96**, (2006)
- [156] S. X. Song, X. L. Wang, and T. G. Nieh, *Scripta Mater.*, **62**, 847-850 (2010)
- [157] Y. F. Gao, *Modell. Simul. Mater. Sci. Eng.*, **14**, 1329 (2006)
- [158] T. S. Oh, R. M. Cannon, and R. O. Ritchie, *J. Am. Ceram. Soc.*, **70**, C352-C355 (1987)
- [159] D. M. Lipkin, D. R. Clarke, and A. G. Evans, *Acta Mater.*, **46**, 4835-4850 (1998)
- [160] M. R. Turner and A. G. Evans, *Acta Mater.*, **44**, 863-871 (1996)
- [161] A. G. Evans, J. W. Hutchinson, and Y. Wei, *Acta Mater.*, **47**, 4093-4113 (1999)
- [162] L. H. Liang, X. M. You, H. S. Ma, and Y. G. Wei, *J. Appl. Phys.*, **108**, (2010)

- [163] Q. Jiang, D. S. Zhao, and M. Zhao, *Acta Mater.*, **49**, 3143-3147 (2001)
- [164] Q. Jiang, L. H. Liang, and D. S. Zhao, *J. Phys. Chem. B*, **105**, 6275-6277 (2001)
- [165] C. Suryanarayana and A. Inoue, *Bulk Metallic Glasses*, *CRC Press, Taylor & Francis Group*. 2011, New York.
- [166] K. T. Ramesh, D. Jia, and E. Ma, *Acta Mater.*, **51**, 3495-3509 (2003)
- [167] Q. Wei, D. Jia, K. T. Ramesh, and E. Ma, *Appl. Phys. Lett.*, **81**, 1240-1242 (2002)

Tables

Table 1.1 Fundamental properties and application fields of bulk amorphous and nanocrystalline alloys [6].

Fundamental characteristic	Application field
High strength	Machinery structural materials
High hardness	Optical precision materials
High fracture toughness	Die materials
High impact fracture energy	Tool materials
High fatigue strength	Cutting materials
High elastic energy	Electrode materials
High corrosion resistance	Corrosion resistant materials
High wear resistance	Hydrogen storage materials
High viscous flowability	Ornamental materials
High reflection ratio	Composite materials
Good soft magnetism	Writing appliance materials
High frequency permeability	Sporting goods materials
High magnetostriction	Bonding materials
Efficient electrode (Chlorine gas)	Soft magnetic materials
High hydrogen storage	High magnetostrictive materials

Table 1.2 Bulk metallic glasses and their developed year [21].

Nonferrous metal BMG system	Years	Ferrous metal base BMG system	Years
Pd-Cu-Si	1974	Fe-(Nb,Mo)-(Al,Ga)-(P,C,B,Si,Ge)	1995
Pt-Ni-P	1975	Pd-(Cu,Fe)-Ni-P	1996
Au-Si-Ge	1975	Fe-(Zr,Hf,Nb)-B	1996
Pd-Ni-P	1982	Co-Fe-(Zr,Hf,Nb)-B	1996
Mg-Ln-Cu (Ln = lanthanide metal)	1988	Zr-Nb-Cu-Fe-Be	2000
Ln-Al-TM (TM = group transition)	1989	Fe-Mn-Mo-Cr-C-B	2002
Zr-Ti-Al-TM	1990		
Ti-Zr-TM	1993		
Zr-Ti-Cu-Ni-Be	1993		
Nd(Pr)-Al-Fe-Co	1994		
Zr-(Nb,Pd)-Al-TM	1995		
Cu-Zr-Ni-Ti	1995		
Co-(Al,Ga)-(P,B,Si)	1996		
Ni-(Zr,Hf,Nb)-(Cr,Mo)-B	1996		
Ti-Ni-Cu-Sn	1998		
La-Al-Ni-Cu-Co	1998		
Ni-Nb	1999		
Ni-(Nb,Cr,Mo)-(P,B)	1999		
Zr-based glassy composites	1999		
Ni-Nb-(Sn,Ti)	2003		
Pr(Nd)-(Cu,Ni)-Al	2003		

Table 2.1 Binary amorphous systems and mixing enthalpy values calculated based on Miedema's macroscopic model [92].

	Mg	Cu	Y	Gd	Ag	B
Mg		-3	-6		-10	
Cu	-3		-22	-22	2	0
Y	-6	-22			-29	-50
Gd		-22				-50
Ag	-10	2	-29			
B		0	-50	-50		

Table 4.1 Deposition rates with variant target materials at different powers.

System	Materials	Power (W)	Deposition rate (nm/min)
DC	Zr	200	15
		250	18.5
		300	22
	Cu	50	15
		100	24
		150	40
	Mo	100	15.1
		200	29.2
		300	34.1
RF	Cu	100	10
		150	13
		200	16
Co-sputtering	Zr/Cu	300/100	57

Table 4.2 Summary of the modulus and hardness of the as-deposited thin films and silicon wafer, obtained from nanoindentation.

Thin film specimen	Modulus E, (GPa)	Hardness, (GPa)
Monolithic ZrCu TFMG	93	4.7
Monolithic Zr crystalline film	125	5.2
Monolithic Cu crystalline film	136	2.4
Monolithic Mo crystalline film	280	14.8
Silicon wafer [100]	172	11.2

Table 5.1 Summary of the results of various tested pillars, obtained from the microcompression tests.

Thin film specimen	Strain rate, s⁻¹	Preset displacement, nm	E, GPa	YS, GPa
Monolithic ZrCu amorphous film	2x10⁻³	300	92	2.7
Monolithic Zr crystalline film	2x10⁻³	300	129	3.2
ZrCu/Zr seven layers: L7	2x10⁻³	300	108	2.5
ZrCu/Zr/ZrCu Three layers: L3	2x10⁻³	300	124	2.7

Figures

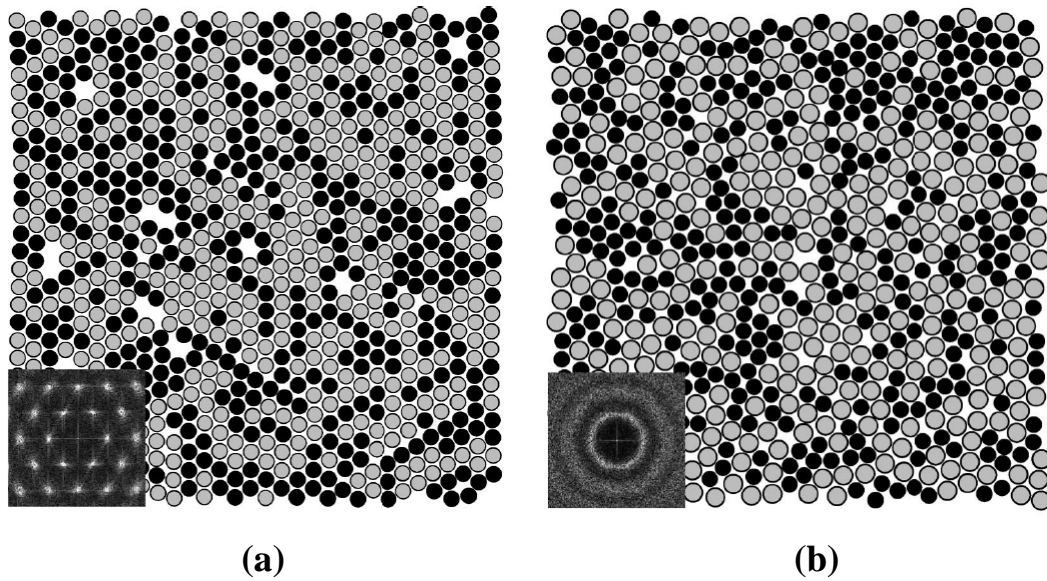


Figure 1.1 Two typical arrangement of atomic structures in (a) crystal and (b) amorphous alloy. The inset Fourier transforms in left corner shows the structural differences [1].



Figure 1.2 The shiny and smooth outward appearance of liquid metal [2].

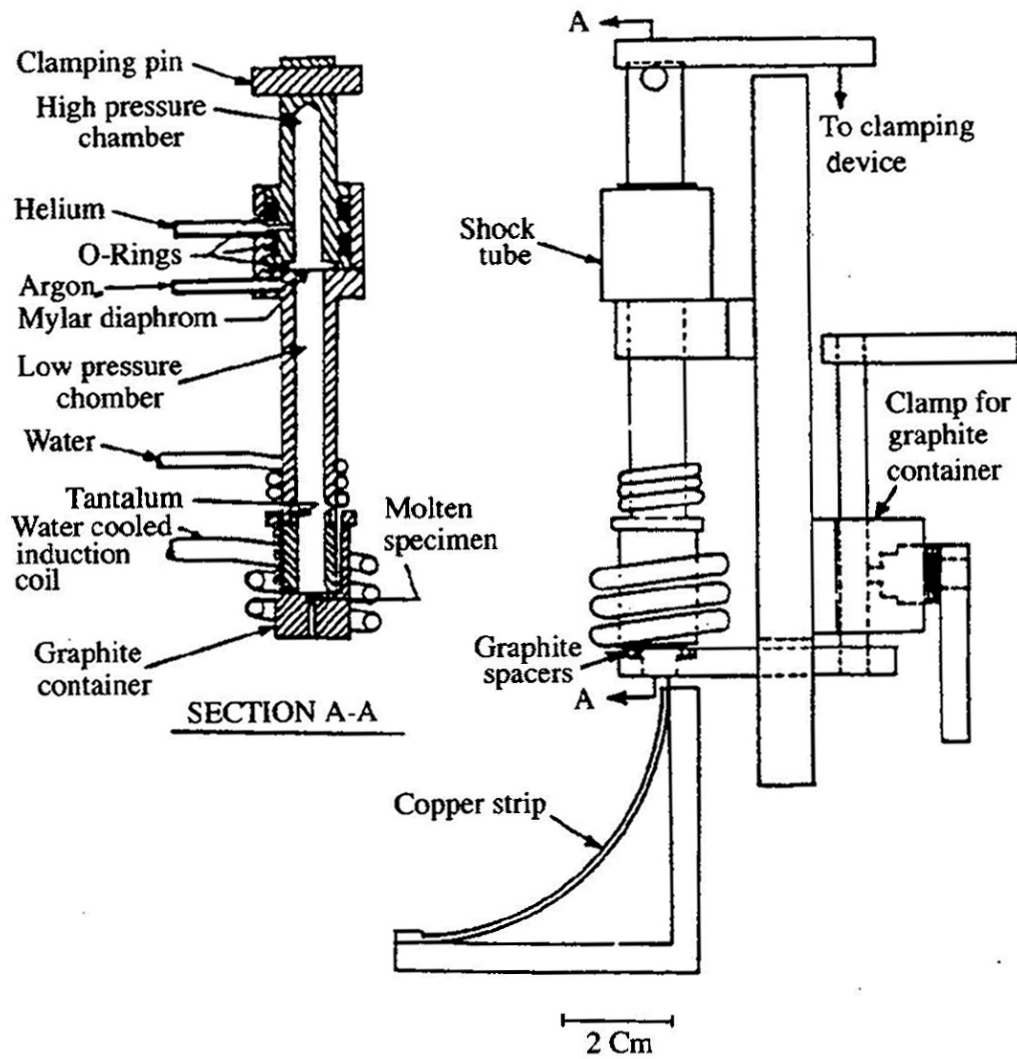


Figure 1.3 Schematic illustration of the splat quenching method [8].

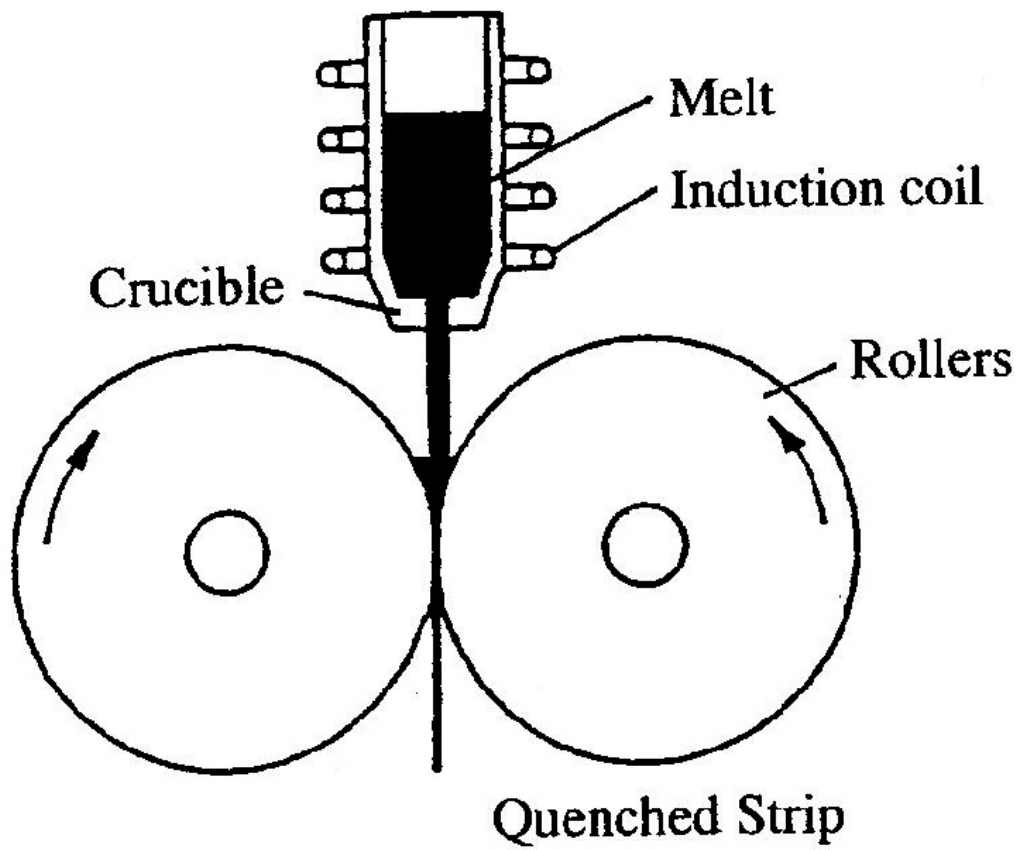


Figure 1.4 Schematic illustration of the two rollers quenching process [8].

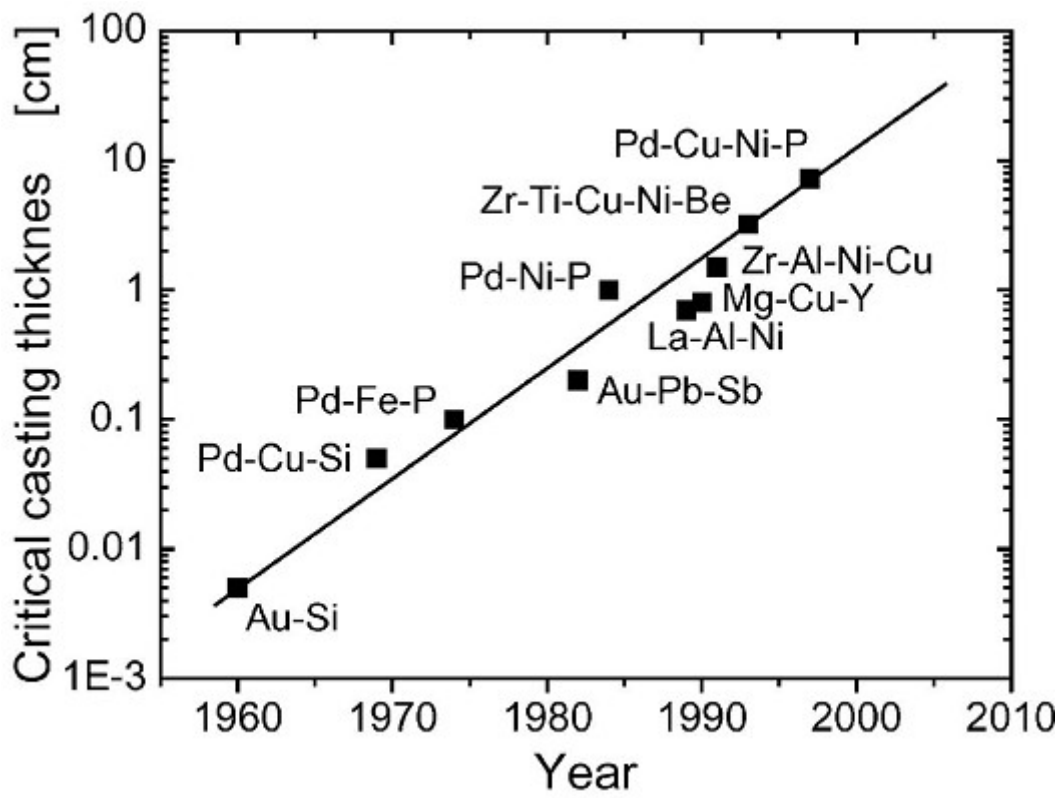


Figure 1.5 The relationship of critical casting thickness with the date of discovery [22].

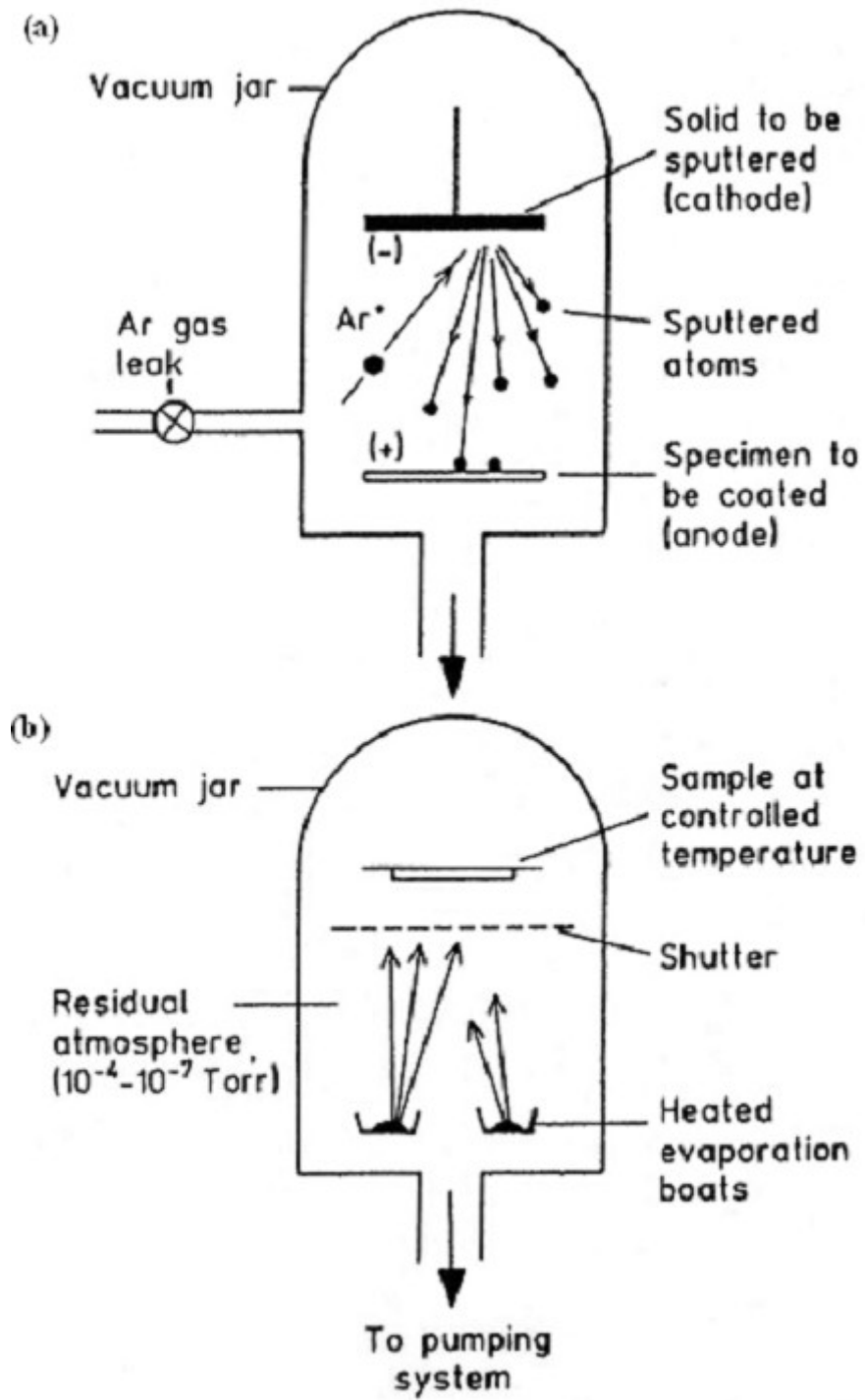


Figure 2.1 Schematic drawing of (a) sputtering and (b) vacuum evaporation [65].

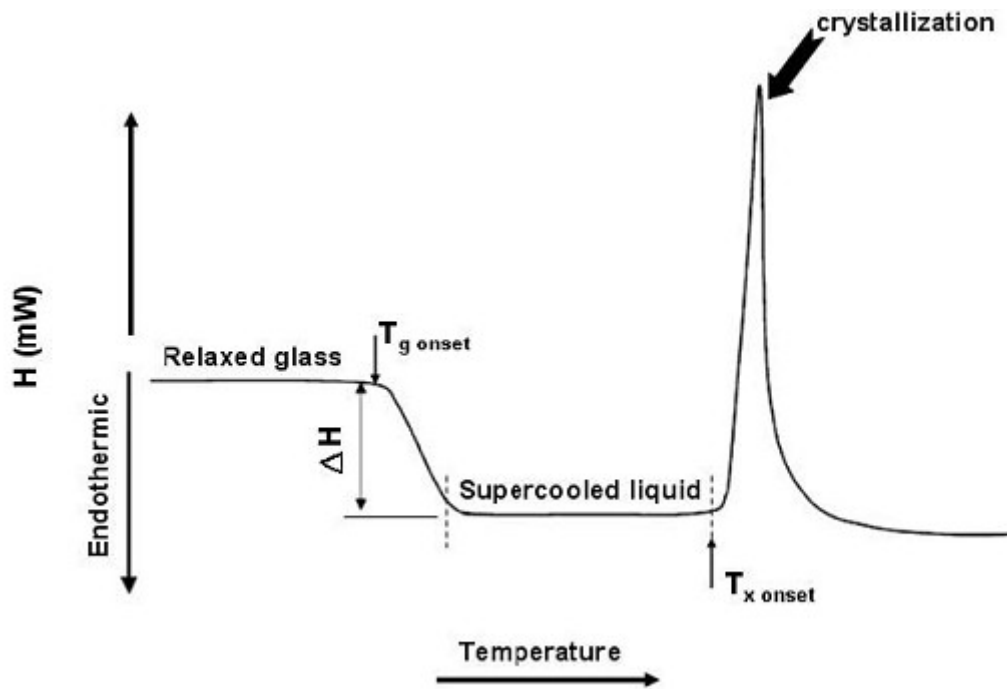


Figure 2.2 The DSC trace of a metallic glass [88].

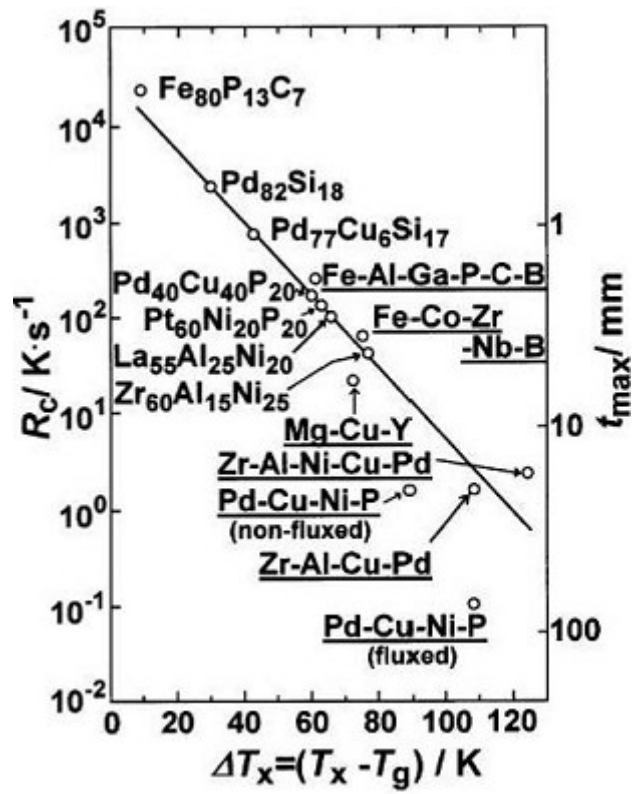


Figure 2.3 The relationship of R_c and ΔT_x [6].

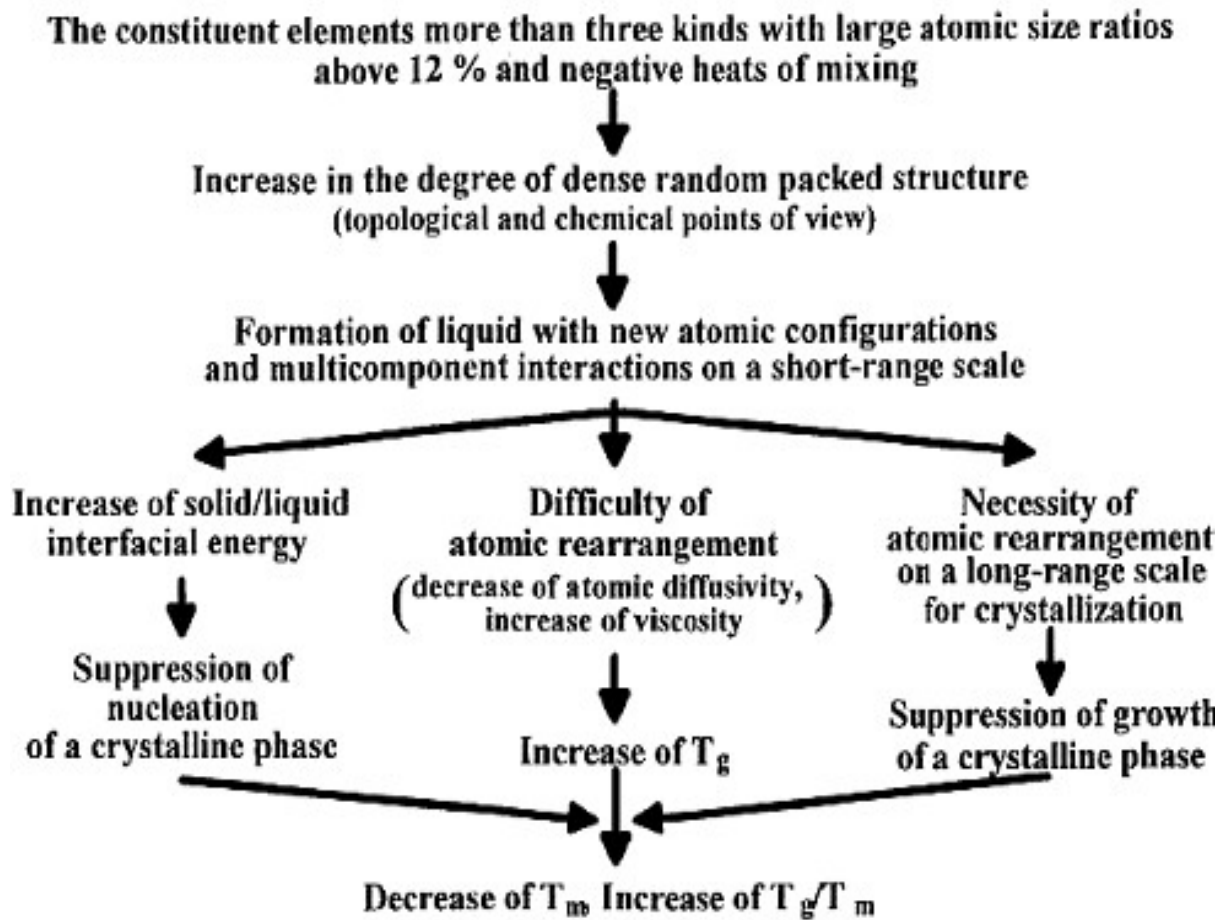


Figure 2.4 Mechanisms for the stabilization of supercooled liquid and the high glass-forming ability [6].

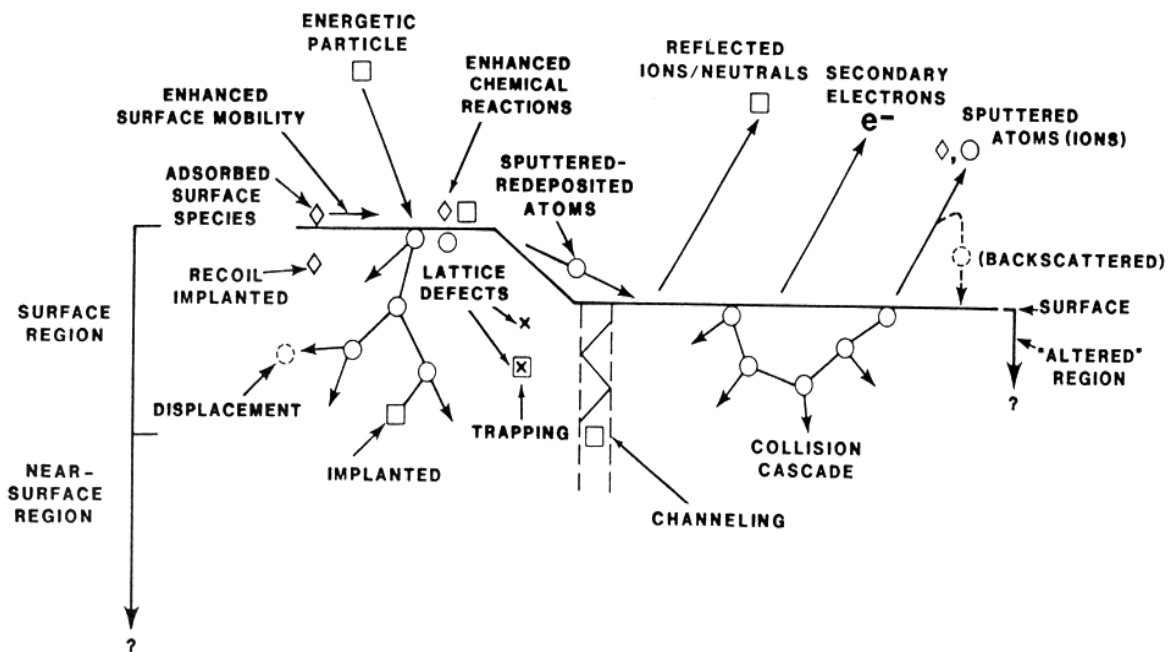


Figure 2.5 Events that occur on a surface being bombarded with energetic atomic-sized particles [93].

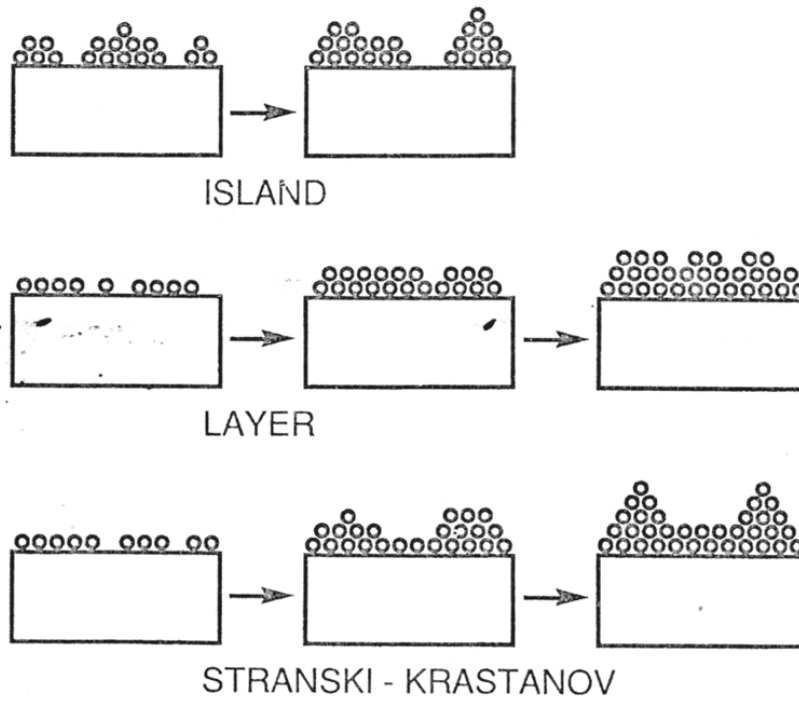


Figure 2.6 Schematic illustrations of three basic growth modes for thin film [95].

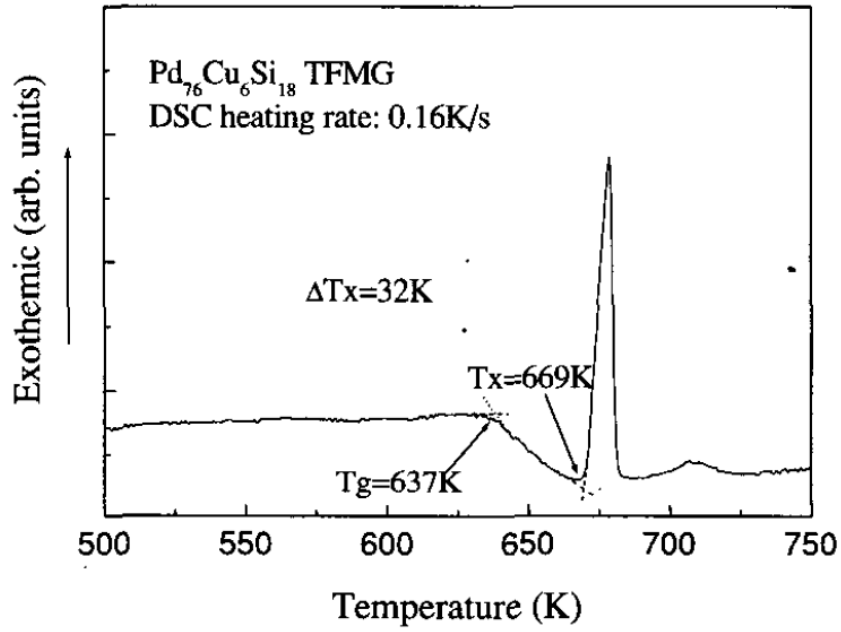


Figure 2.7 DSC thermography curve of the Pd-TFMG [98].

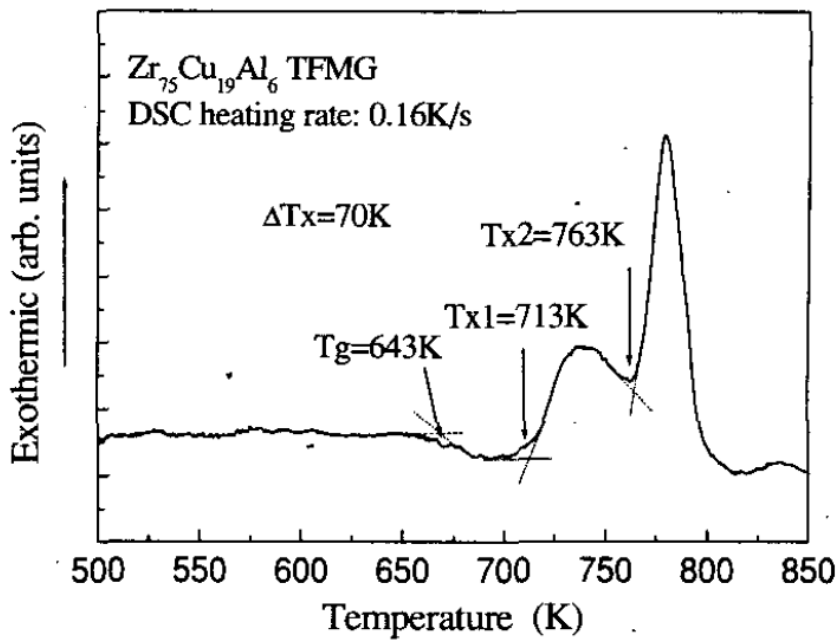


Figure 2.8 DSC thermography curve of the Zr-TFMG [98].

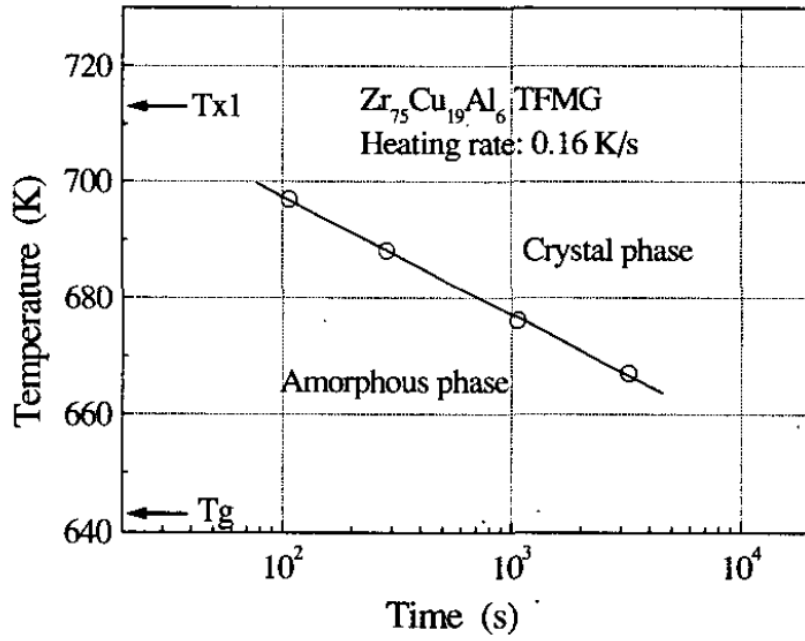


Figure 2.9 TTT diagram for the onset of crystallization in the Zr-TFMG [98].

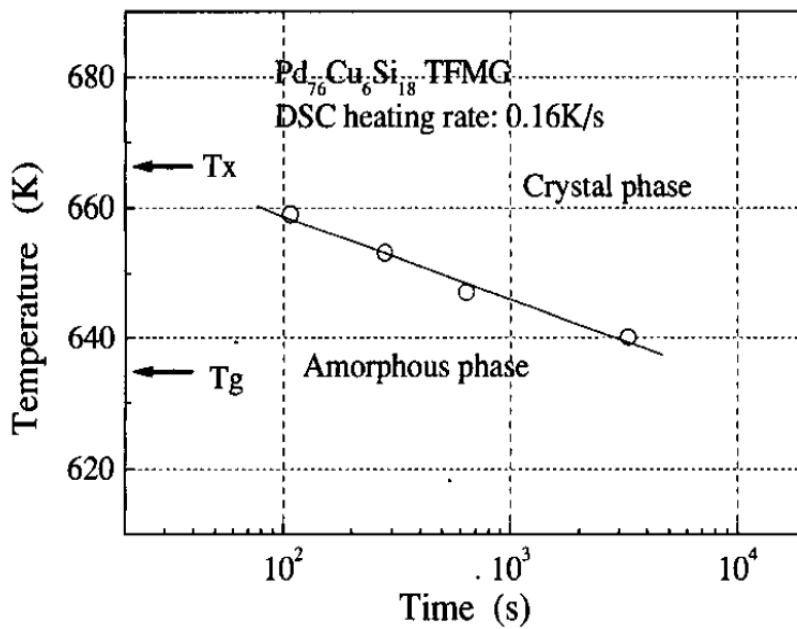


Figure 2.10 TTT diagram for the onset of crystallization in the Pd-TFMG [98].

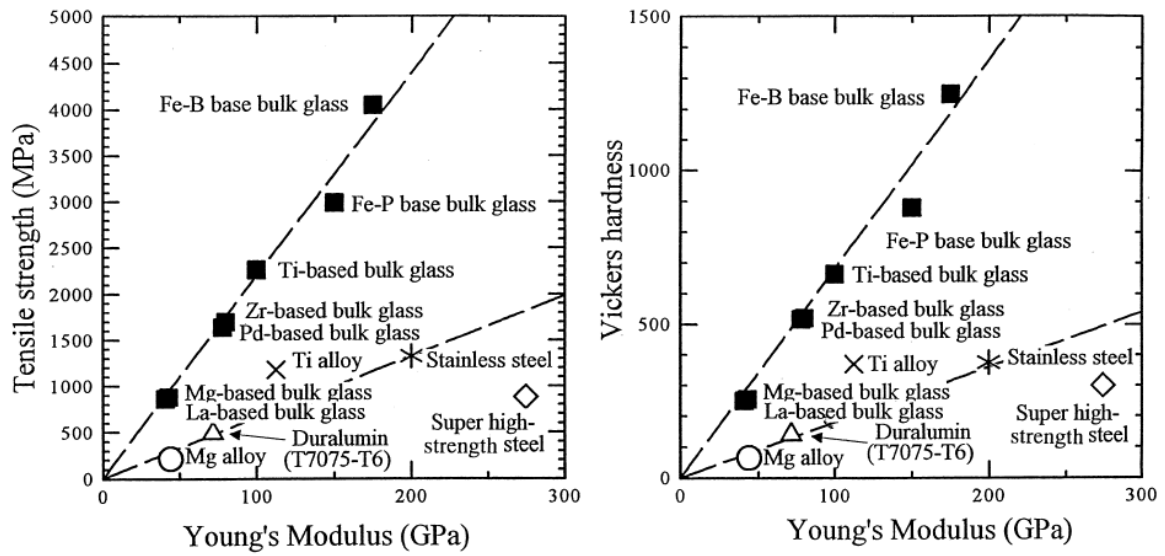


Figure 2.11 Relationship between tensile strength or Vickers hardness (H_v) and E for various bulk amorphous alloys [6].

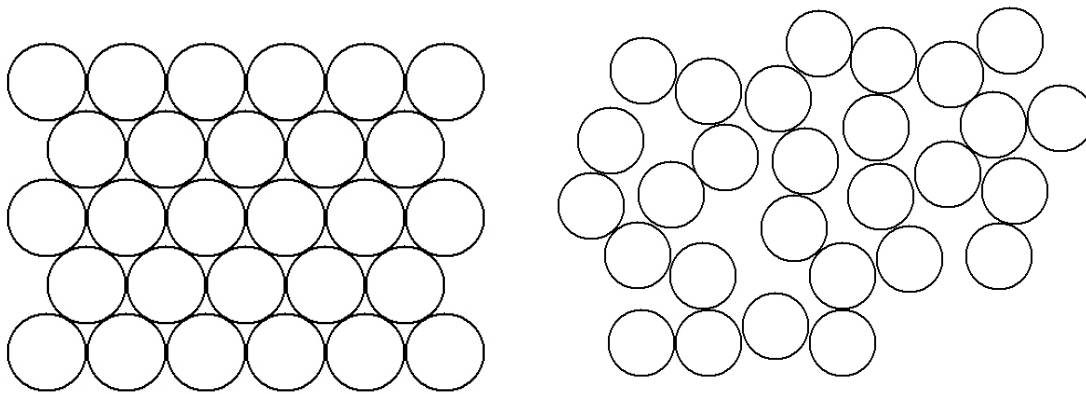


Figure 2.12 The arrangement of atoms in (a) crystalline and (b) amorphous states.

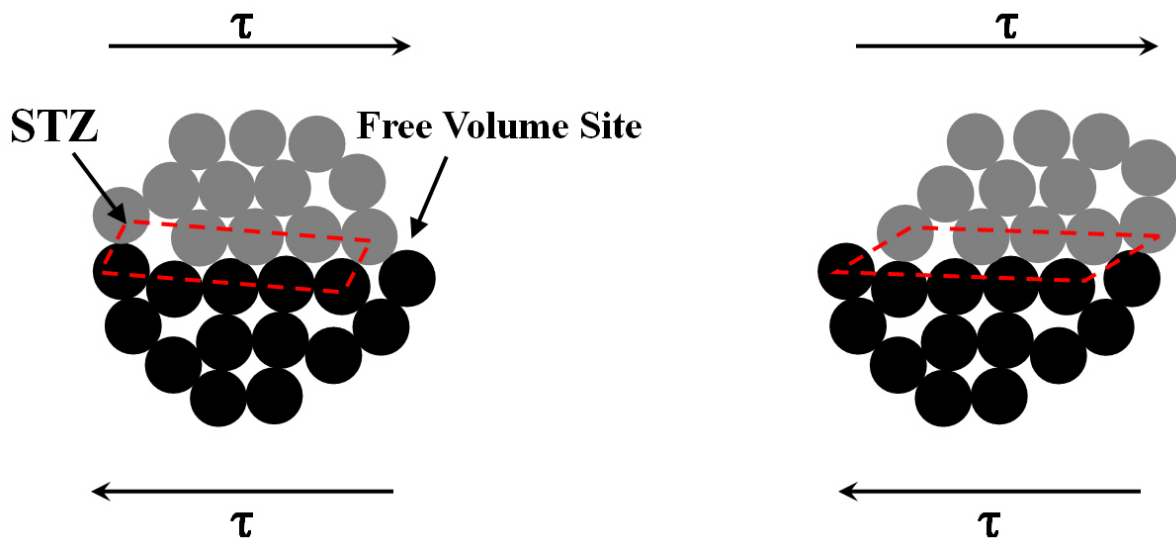


Figure 2.13 The illustration of the shear transformation zones (STZs) (a) before shear deformation and (b) after shear deformation in two-dimensional space.

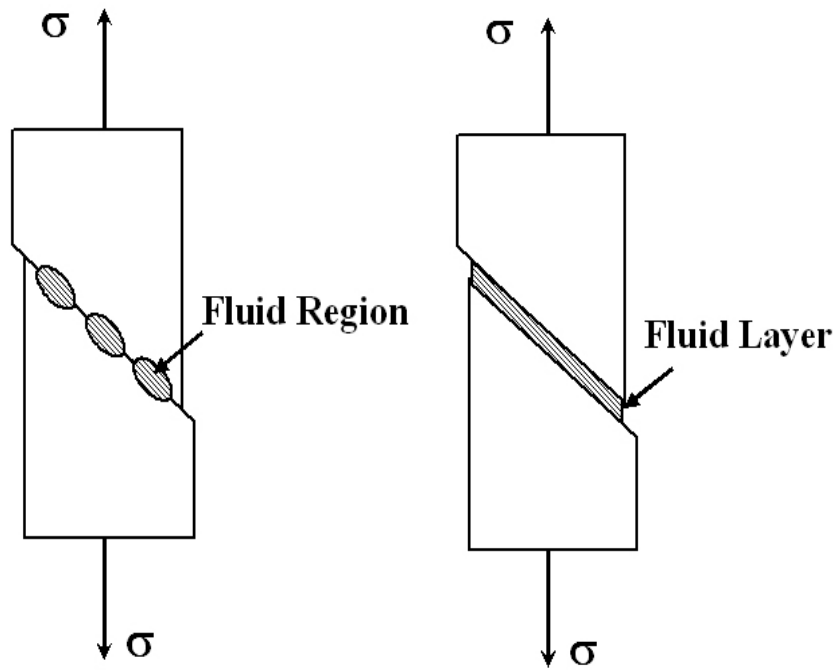


Figure 2.14 Schematic drawing of the fluid zones of amorphous alloy.

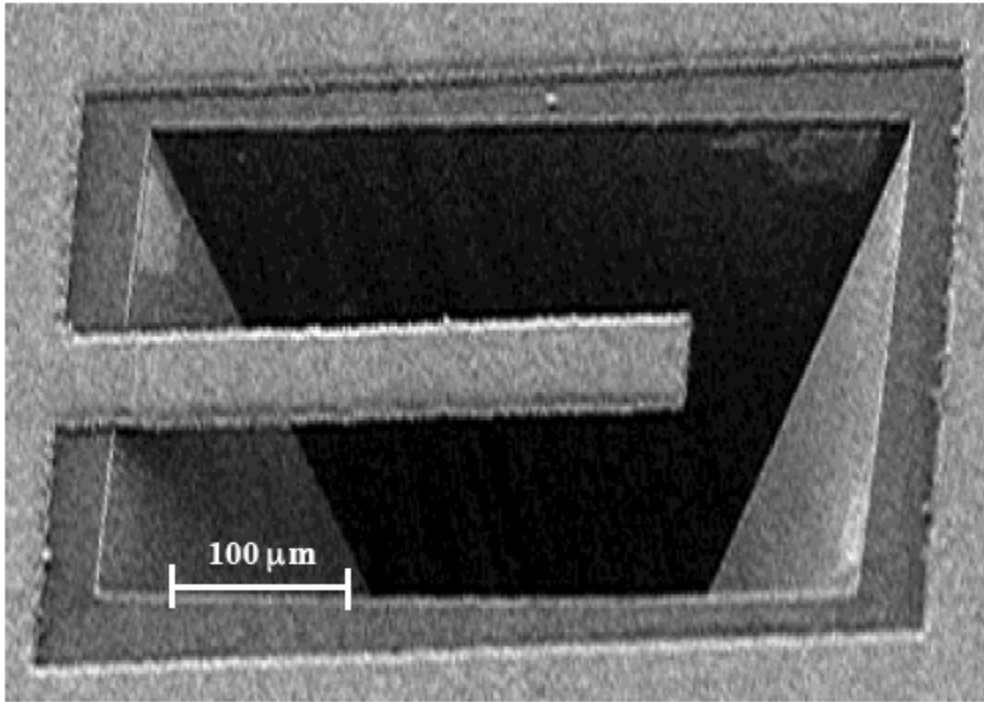


Figure 2.15 SEM micrograph of the cantilever microbeam for the bending test [29].

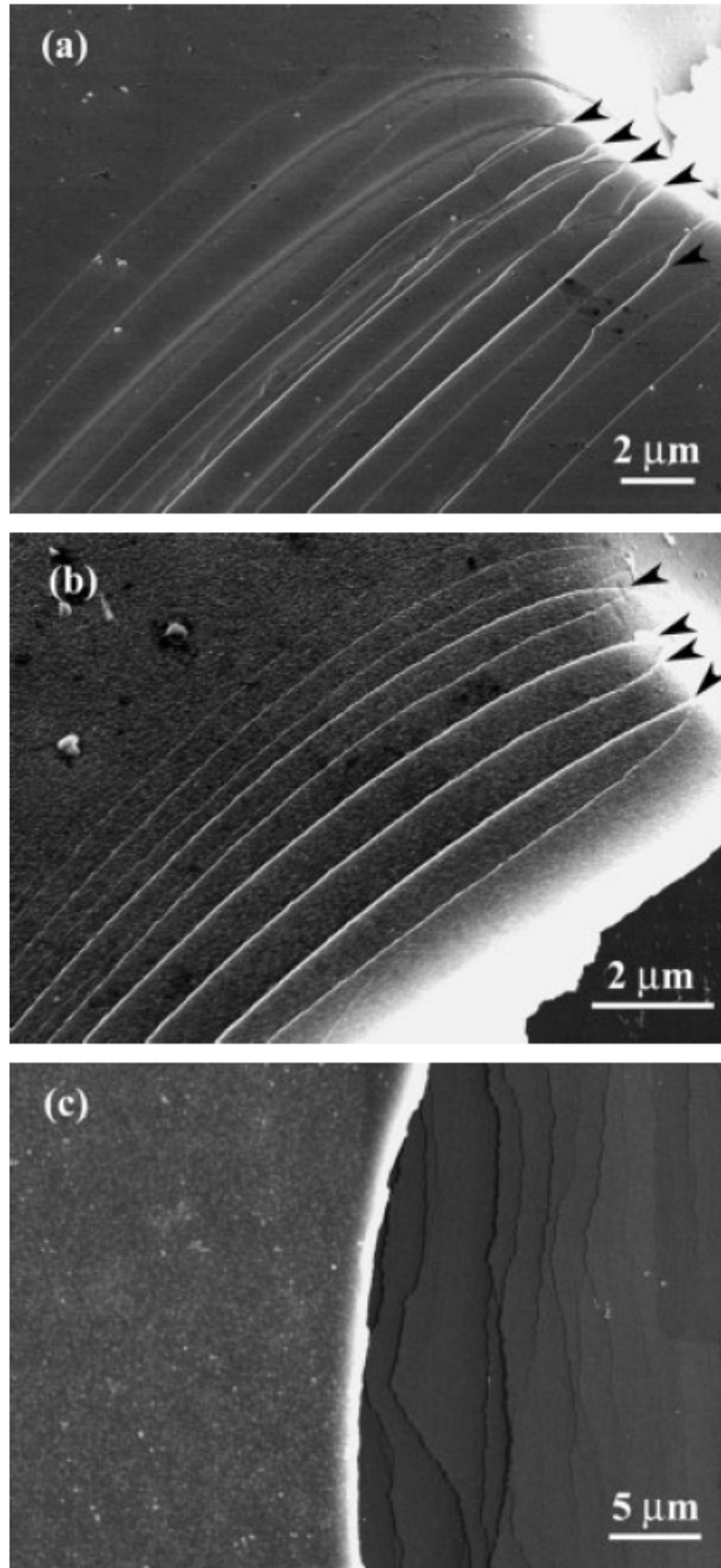


Figure 2.16 SEM observations of the damaged surfaces at the fixed end of Pd-TFMGs microbeams deformed by bending: (a) sample 1, (b) sample 2, (c) sample 3 [102].

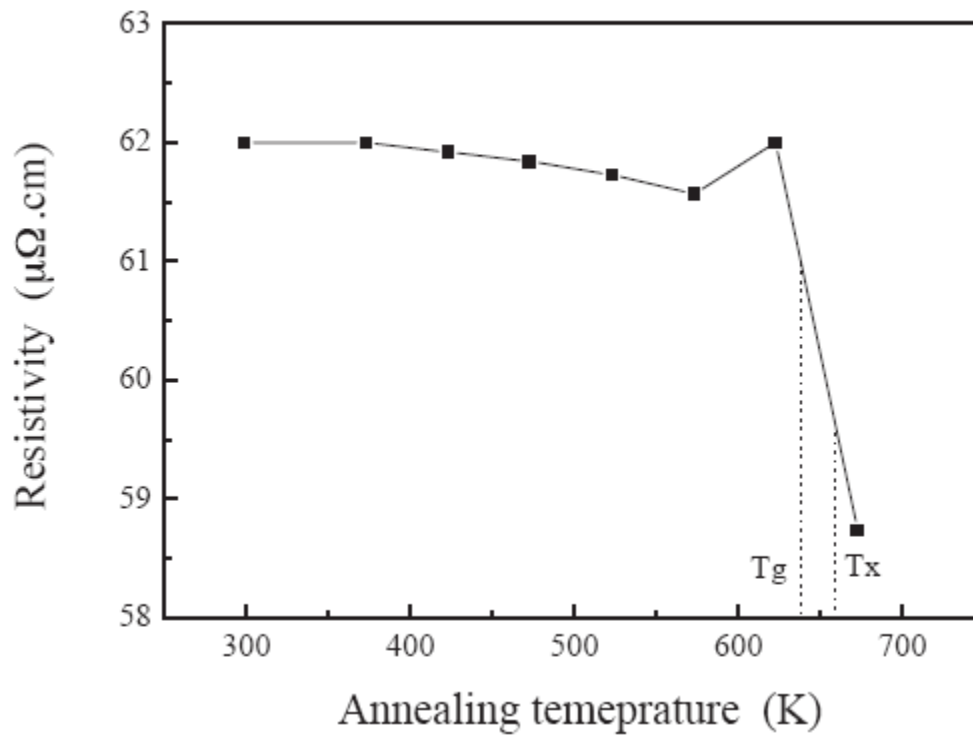


Figure 2.17 Resistivity and annealing temperature of Pd-TFMG [29].

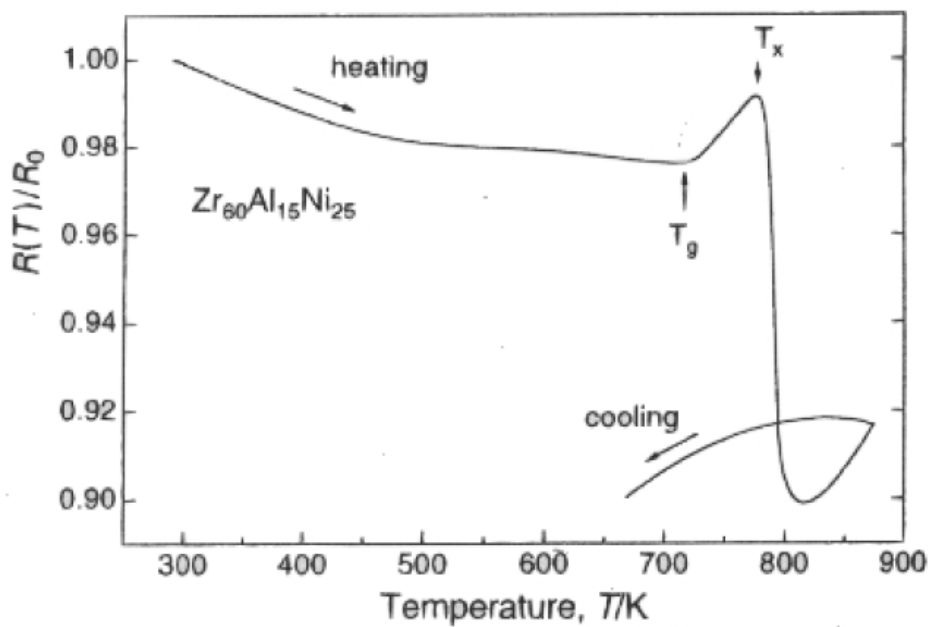


Figure 2.18 Change in electrical resistance with increasing annealing temperature for Zr-based amorphous alloy [29].

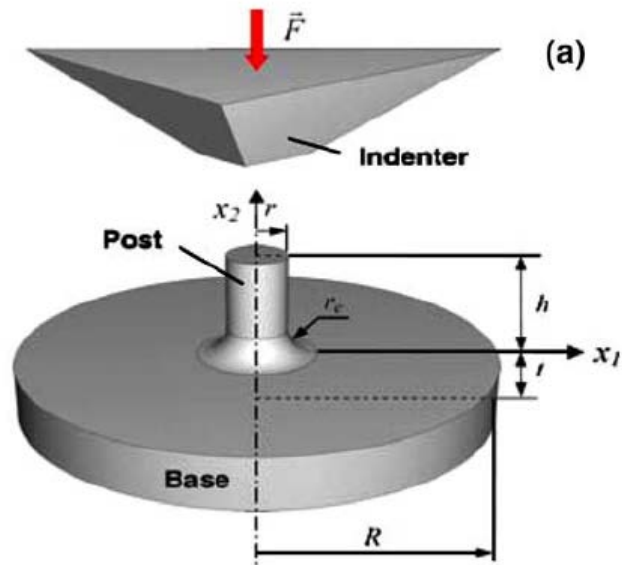


Figure 2.19 Schematic of a cylindrical post and its base [107].

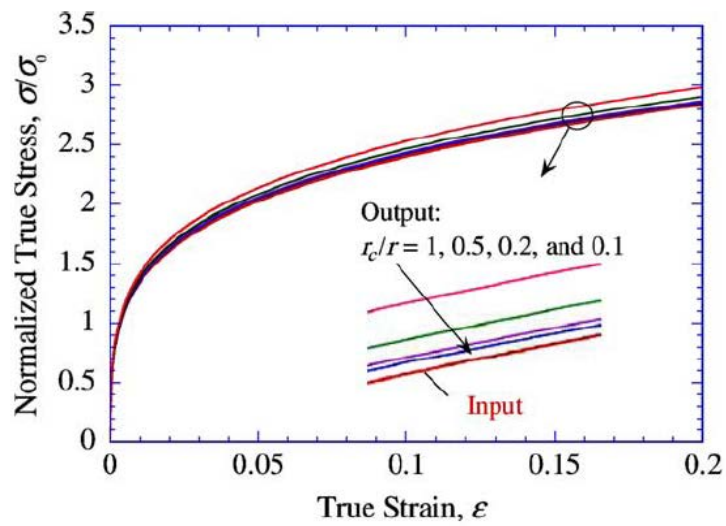


Figure 2.20 Effect of specimen geometry (fillet size) on numerical simulation. The inset shows an enlargement of the circled region to facilitate comparison [107].

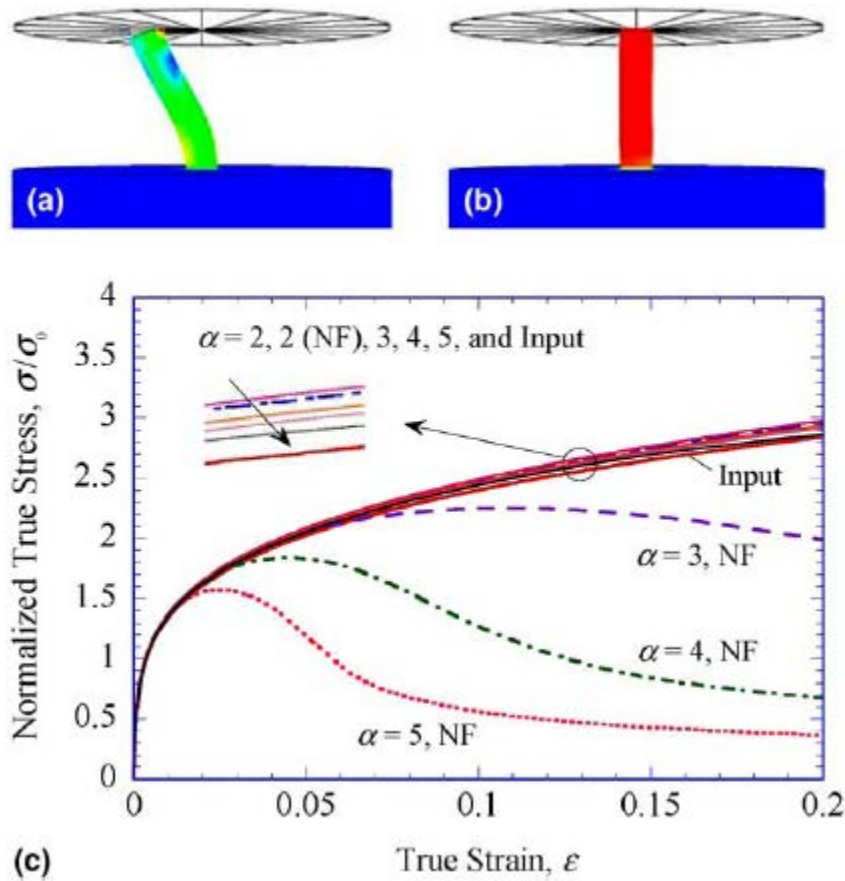


Figure 2.21 (a) Deformed configuration of a circular cylindrical pillar with an aspect ratio $\alpha = 5$ at a strain of 0.1. (b) Deformed configuration of the pillar at the same strain of 0.1, but now considering friction. (c) Input and output stress-strain curves for a pillar with aspect ratios $\alpha = 2\sim 5$, both with friction and without friction (NF) [107].

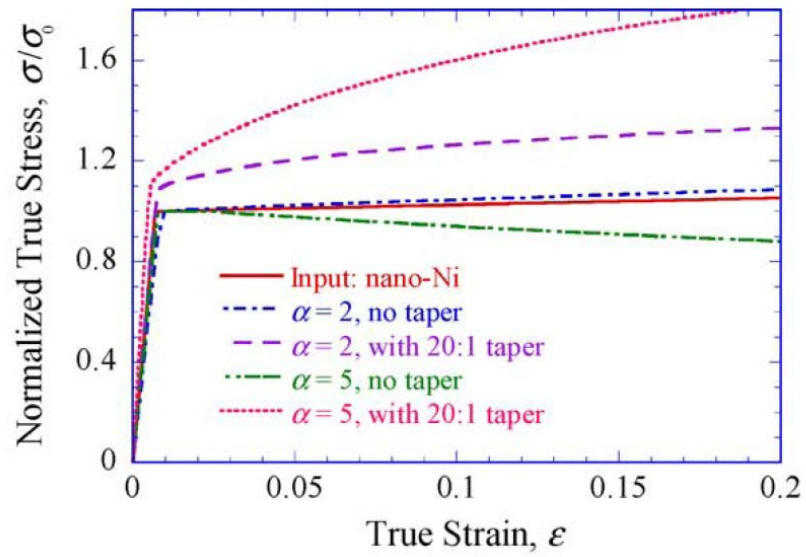


Figure 2.22 Effect of taper and system misalignment on numerical simulations output [107].

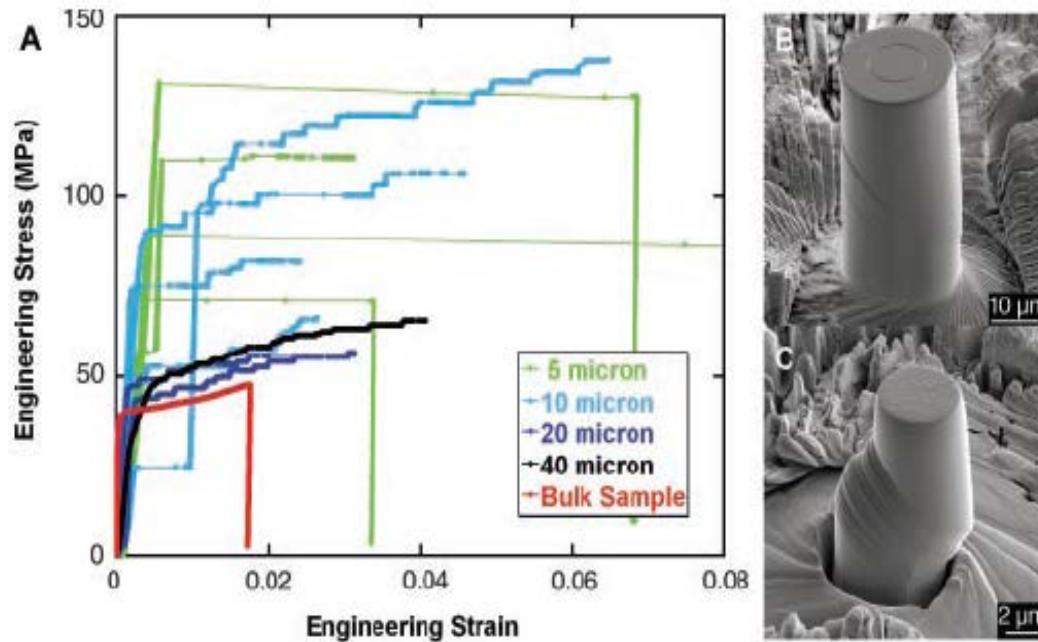


Figure 2.23 Mechanical behavior at room temperature for Ni₃Al-Ta microsamples. (A) Representative stress-strain curves for microsamples ranging in size from 20 to 0.5 μm in diameter. (B) A SEM image of 20-μm diameter microsample, where the sample achieved ~10% strain during the rapid burst of deformation. (C) A SEM image of 1-μm-diameter microsample after testing [106].

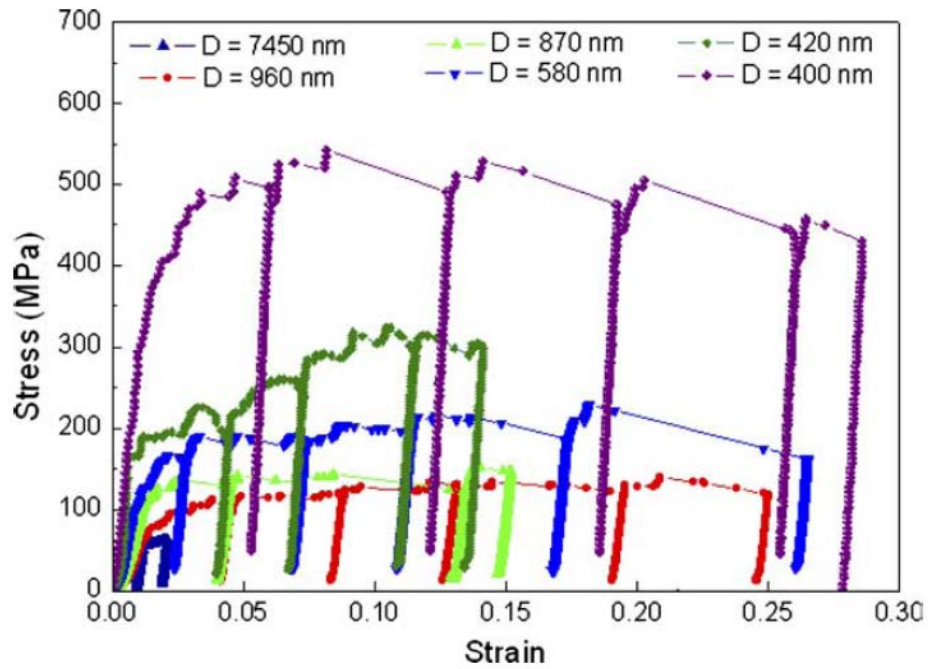


Figure 2.24 Stress–strain behaviors of micropillars: flow stresses increase significantly for pillars with a diameter of 500 nm and less [108].

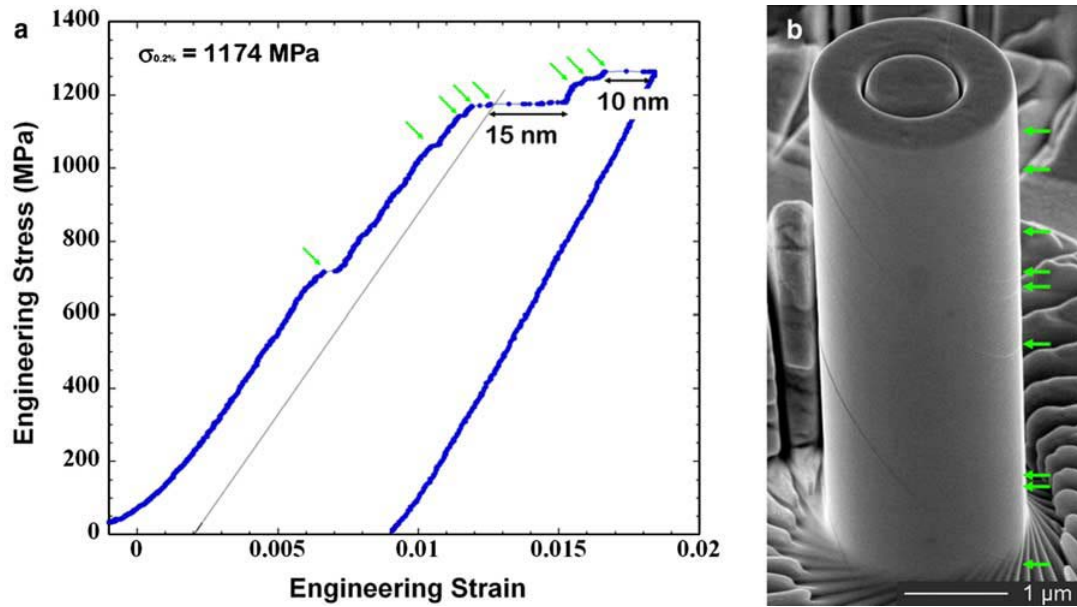


Figure 2.25 (a) A stress–strain curve for a 2 μm diameter micro-crystal of Ni₇₆Al₂₄. Strain bursts are indicated by arrows. (b) A SEM image of the same micro-crystal shown in (a). The appearance of slip lines on the surface of the micro-crystal are indicated by arrows [111].

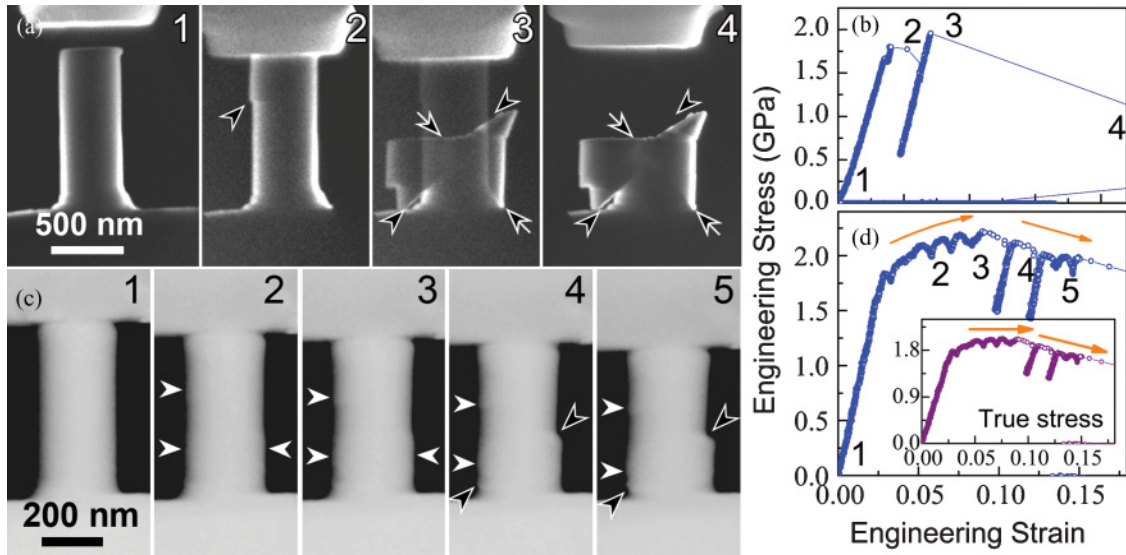


Figure 2.26 Dark-field TEM images showing the deformation of (a) 640 nm and (c) 365 nm diameter pillars: the numbering in (a) and (c) corresponds to the instances numbered in the stress-response curves in (b) and (d), respectively, the inset in (d) being true stress. Open and solid white arrows annotate SBs and local bumps, respectively [125].

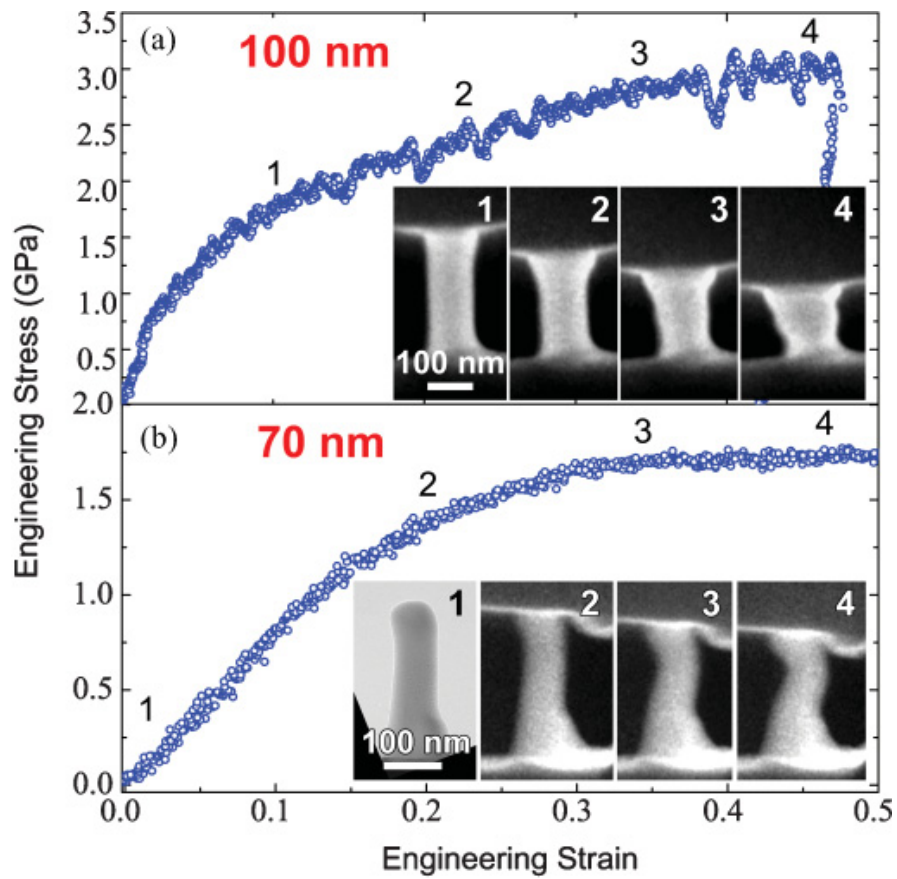


Figure 2.27 Stress and morphological evolutions of nanopillars with diameters of (a) 100 nm and (b) 70 nm, respectively, as functions of strain [125].

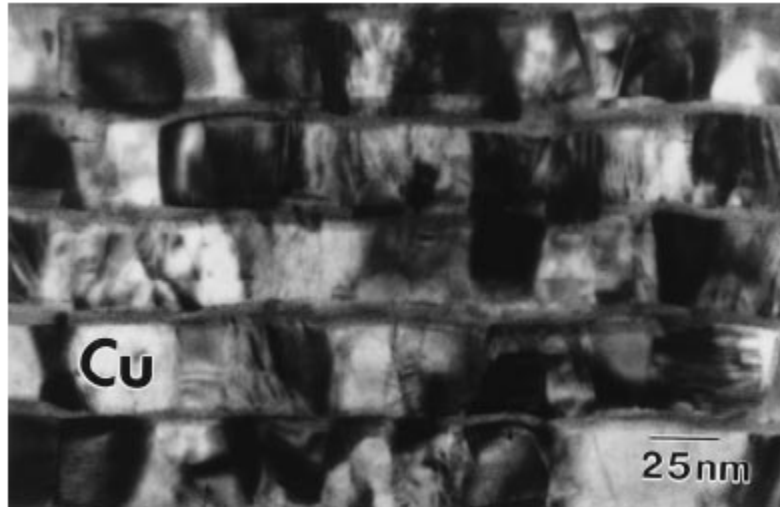


Figure 2.28 TEM microstructure of a deposited Cu-Zr nanolaminate. Between the Cu layers are amorphous Cu₄Zr₃ layers [55].

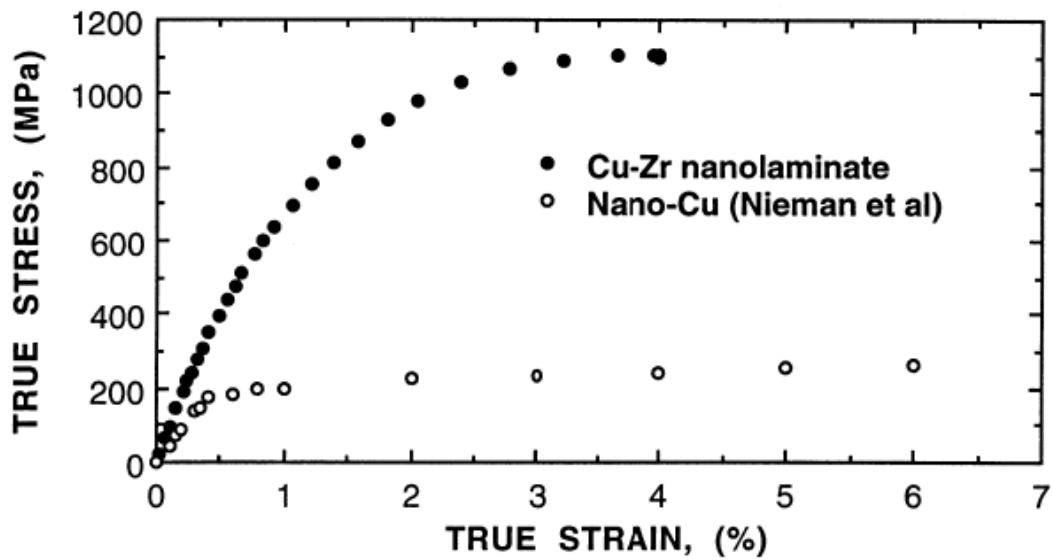


Figure 2.29 Stress-strain curve for Cu-Zr nanolaminate deformed at a strain rate of $2 \times 10^{-3} \text{ s}^{-1}$ [55].

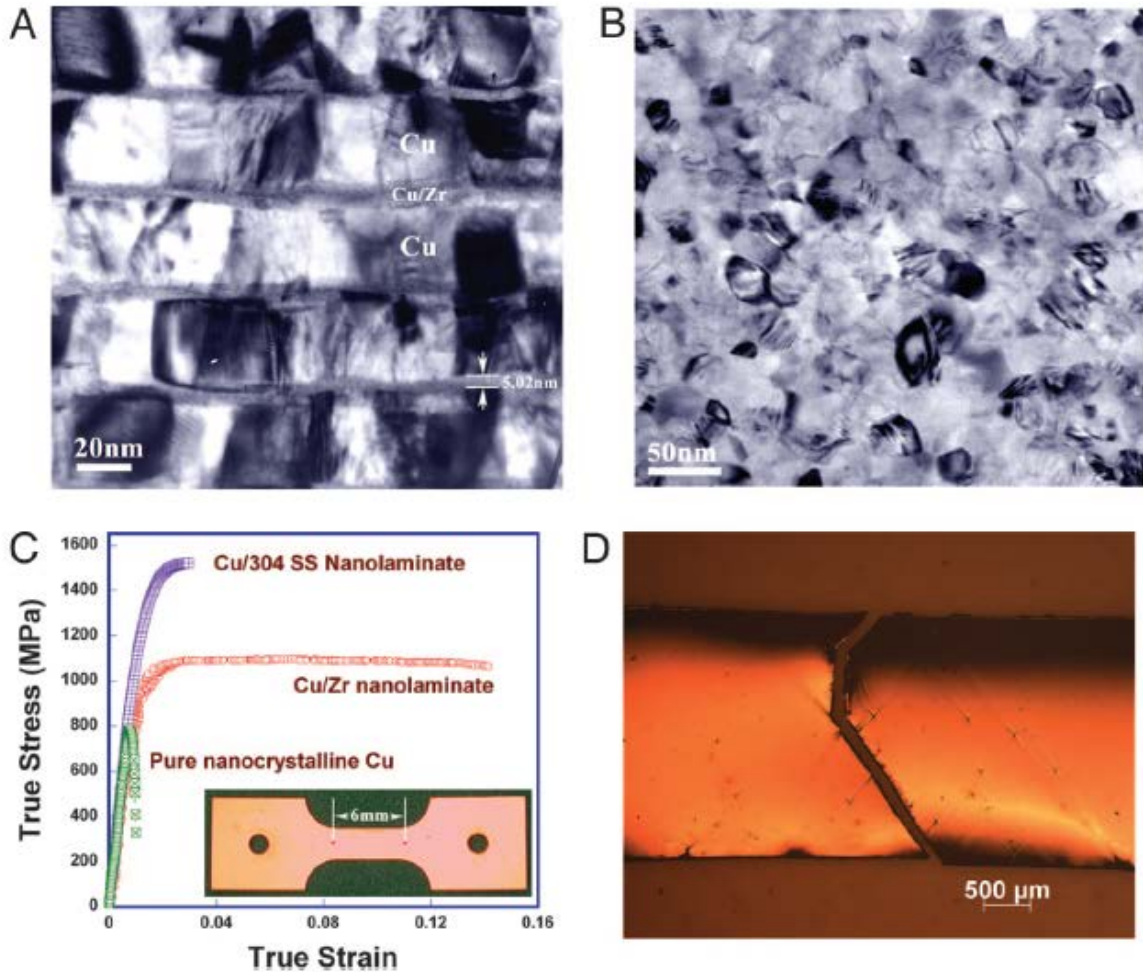


Figure 2.30 Cross-sectional (a) and planview (b) TEM images of the as-deposited 5 nm/35 nm nanocrystalline Cu and amorphous Cu/Zr intermixing multilayer nanostructures. (c) True stress-strain curves for Cu/Zr nanolaminates. (d) The top-view of the gauge section after fracture for 5/35 Cu/Zr nanolaminate [61].

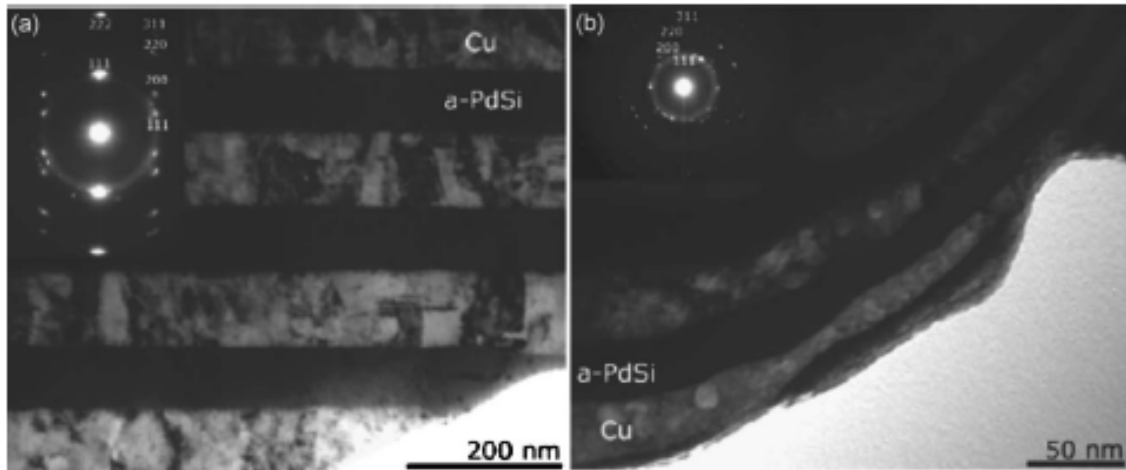


Figure 2.31 Bright field TEM images of 100 nm Cu/*a*-PdSi multilayer: (a) as-deposited and (b) tip region of a bent foil. The *a*-PdSi layers appear as thin dark lines [131].

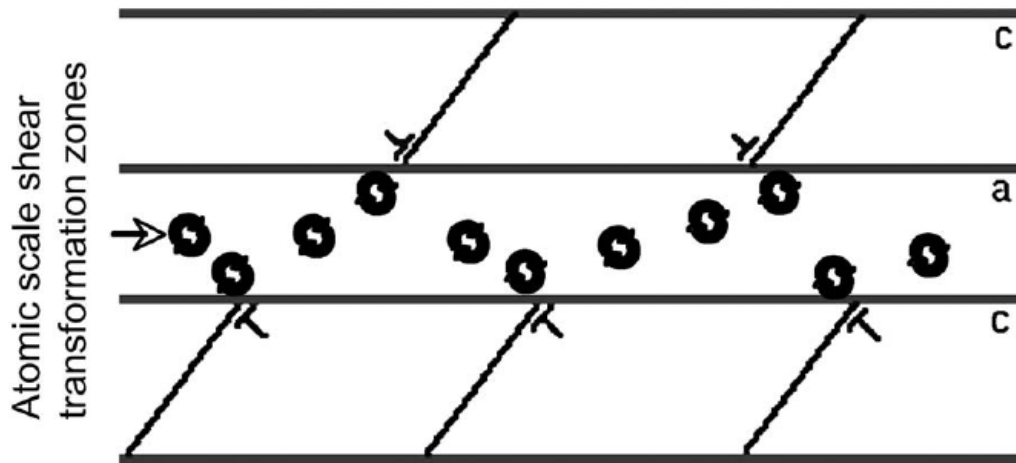


Figure 2.32 Schematic illustration of slip transmission across nanometer-scale crystalline (c)/amorphous (a)/crystalline sandwich structures [131].

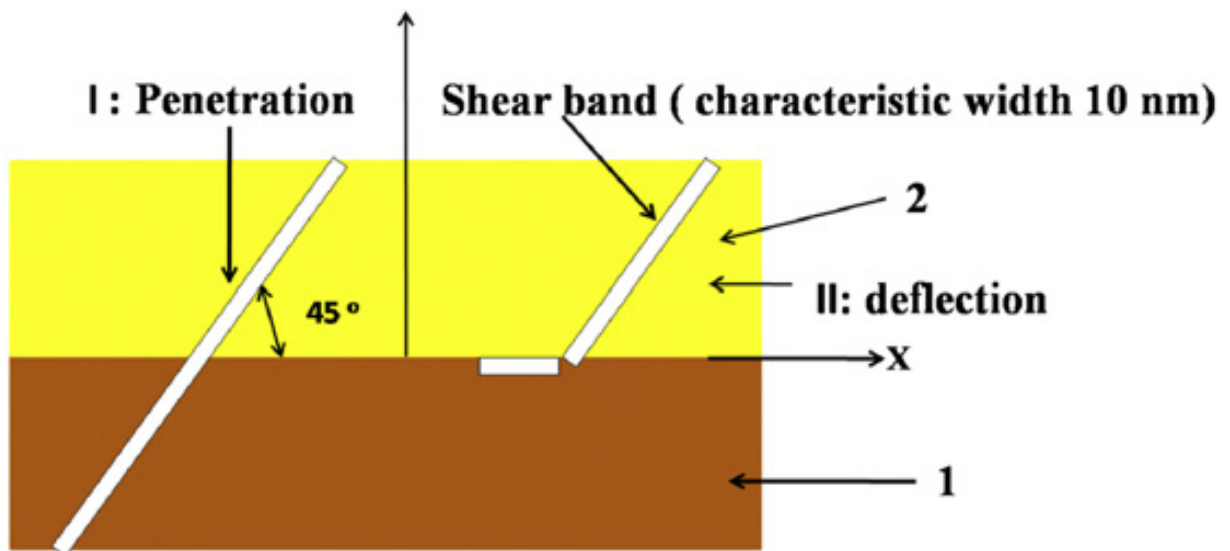


Figure 2.33 Shear band penetration or deflection on the interface of dissimilar materials [133].

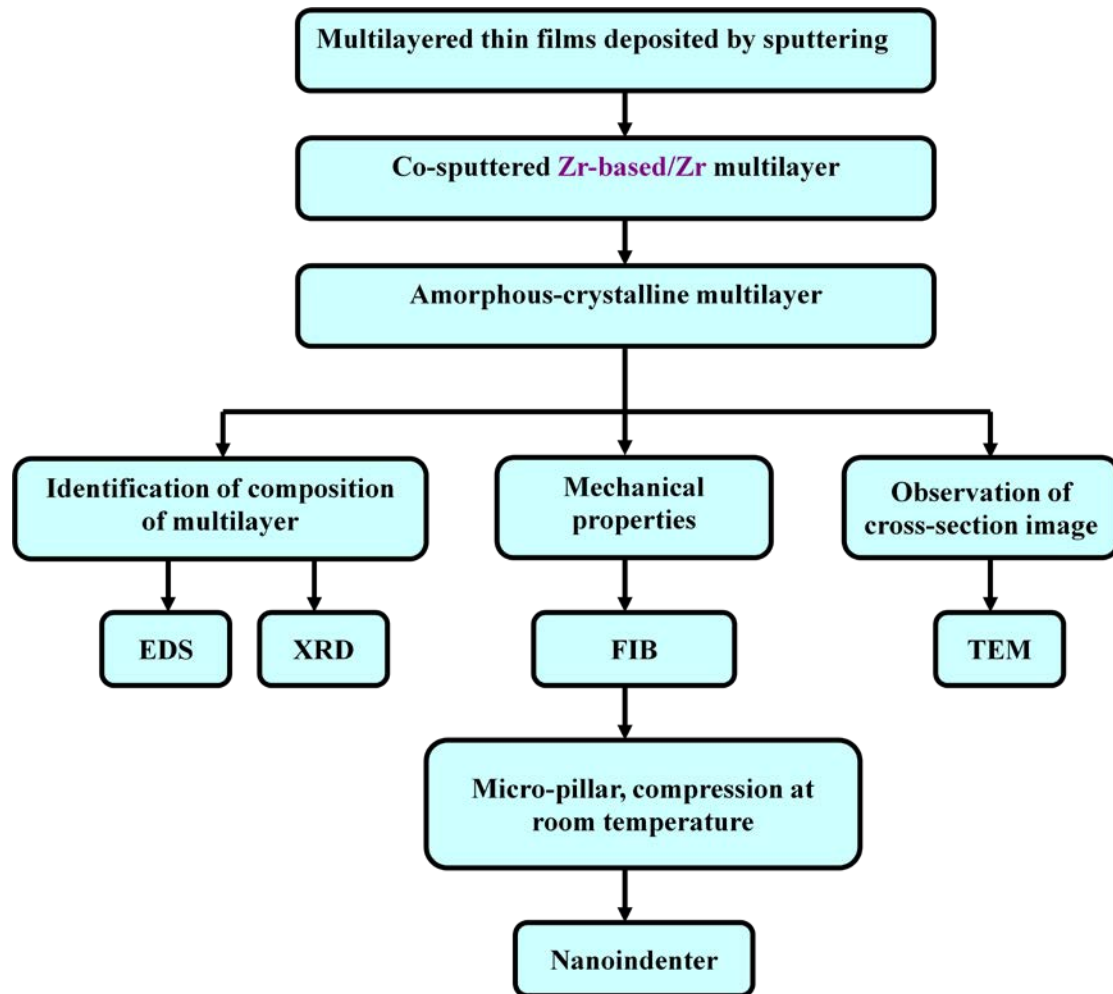


Figure 3.1 The flow chart of the experimental procedures in this study.

Co-sputtering

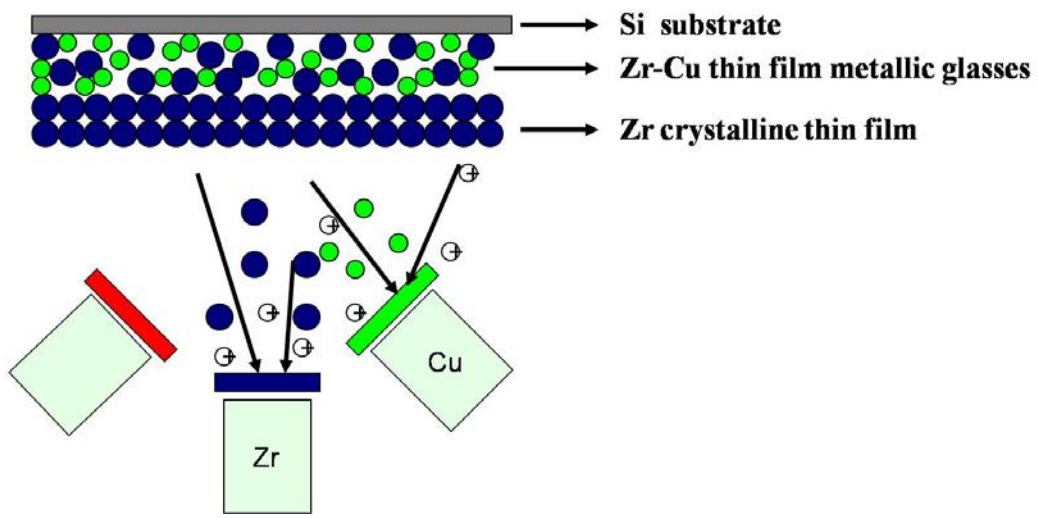


Figure 3.2 Schematic illustrations for co-sputtering process.



- | | |
|----------------------------------|-------------------------------------|
| 1. Nano Indenter® XP | 2. Vibration Isolation Table |
| 3. Vibration Isolation Cabinet | 4. Monitor |
| 5. Computer | 6. Continuous Stiffness Measurement |
| 7. Data Acquisition/Control Unit | 8. Printer |

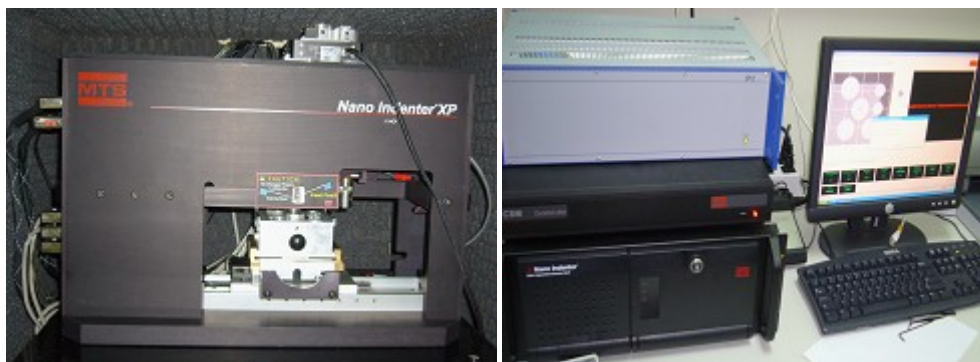


Figure 3.3 The standard Nano Indenter® XP is a complete, turnkey system consisting of the major components illustrated.



Fig. 3.4 The appearance of dual focus ion beam system (FIB, SEIKO SMI3050).

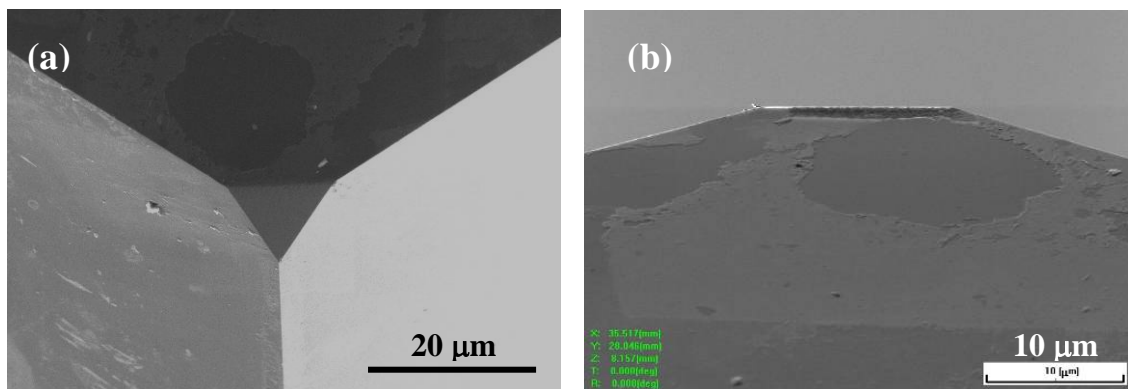


Figure 3.5 SEM micrographs of the flat-punch tip: (a) plane view and (b) side view.

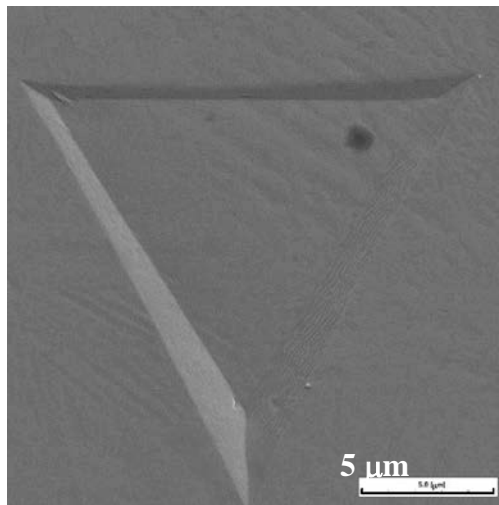


Figure 3.6 SEM micrograph showing the projected area of the punch tip.

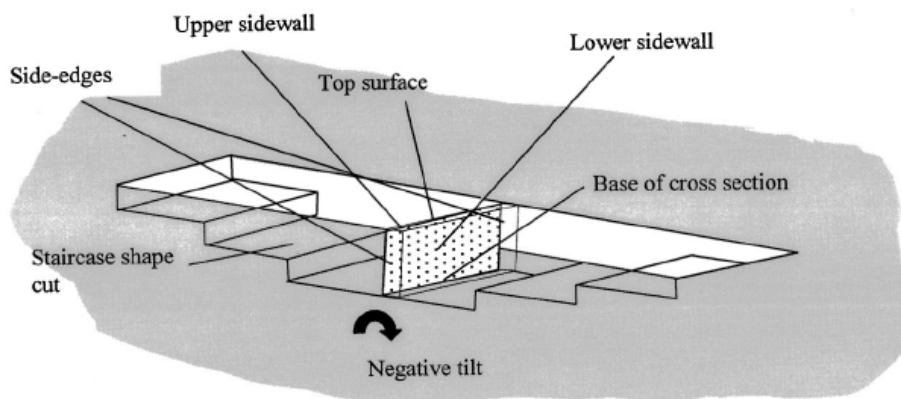


Figure 3.7 Schematic illustration for fabricating TEM specimen by FIB [137, 138].

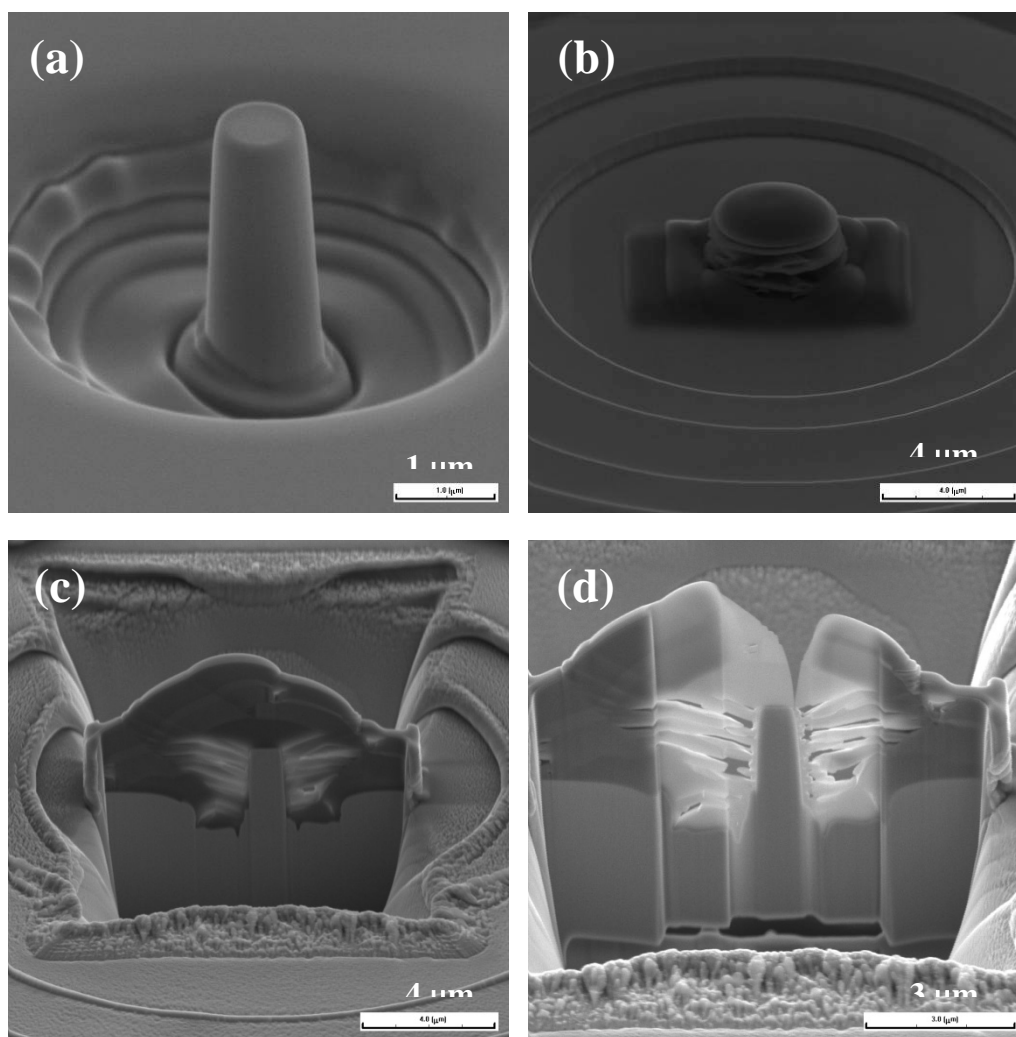


Figure 3.8 TEM sample preparation procedures: (a) Zr-TFMG micropillar with 1 μm diameter before compression test, (b) carbon is deposited around the pillar to fill the empty, (c) an energetic Ga ion beam is used to cut the trench, and (d) TEM sample can be further thinned by using the Ga ion beam with relative lower voltage or current.

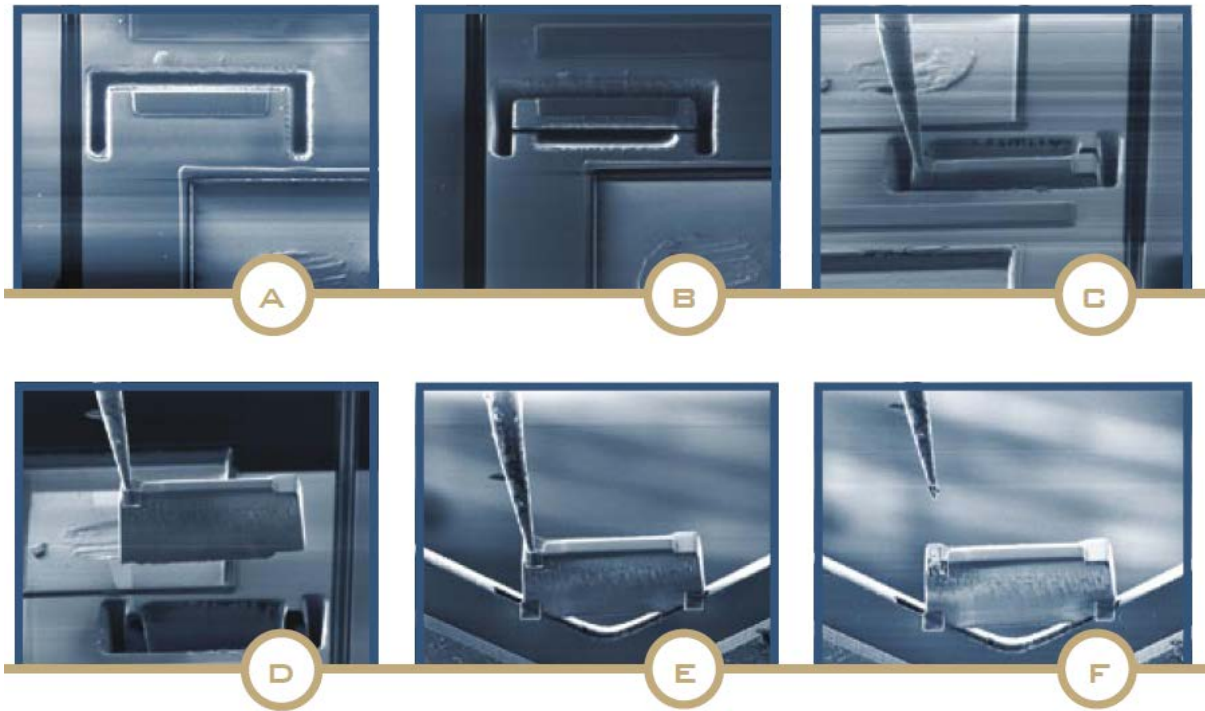


Figure 3.9 Typical six steps of in-situ lift-out method: (A) first cut; (B) release cut; (C) tip attach; (D) extraction; (E) holder attach; (F) and tip separation.

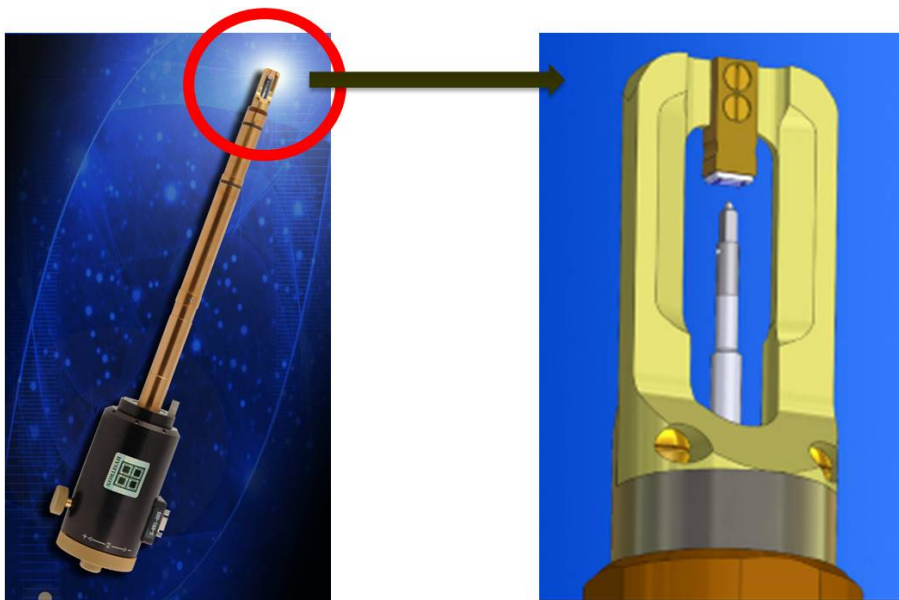


Figure 3.10 Showing the PI 95 TEM picoindenter holder. Holder detail: by positioning the indenter tip directly opposite the sample and perpendicular to the electron beam, the deformation event can be viewed in situ.

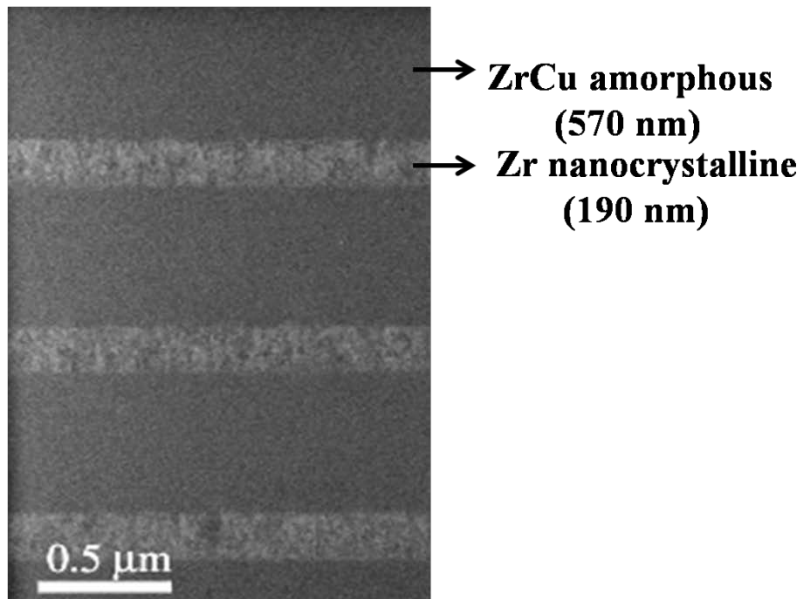


Figure 4.1 Cross-sectional TEM bright-field image of the L7 multilayer thin film.

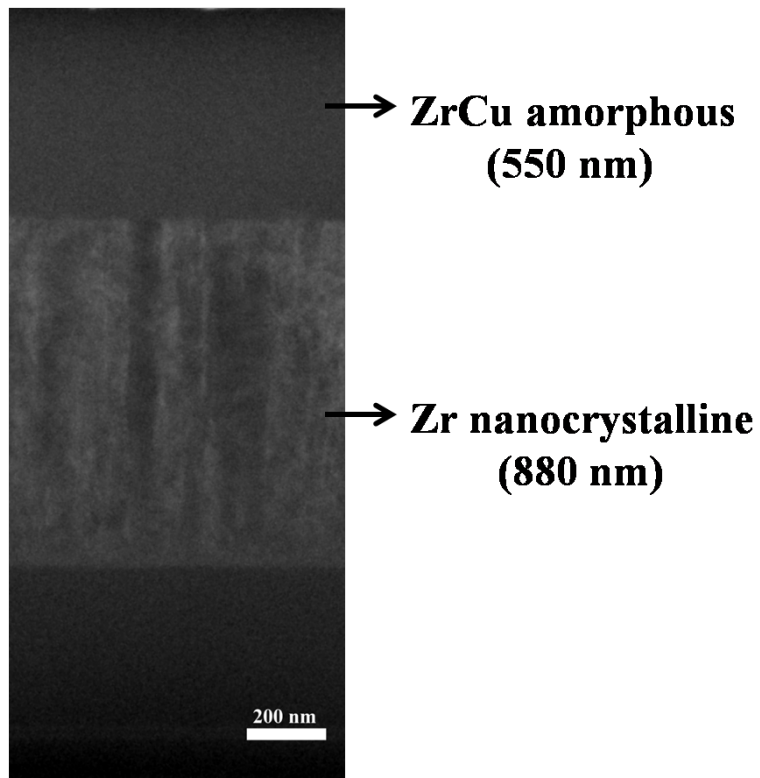


Figure 4.2 Cross-sectional TEM bright-field image of the L3 multilayer layer thin film.

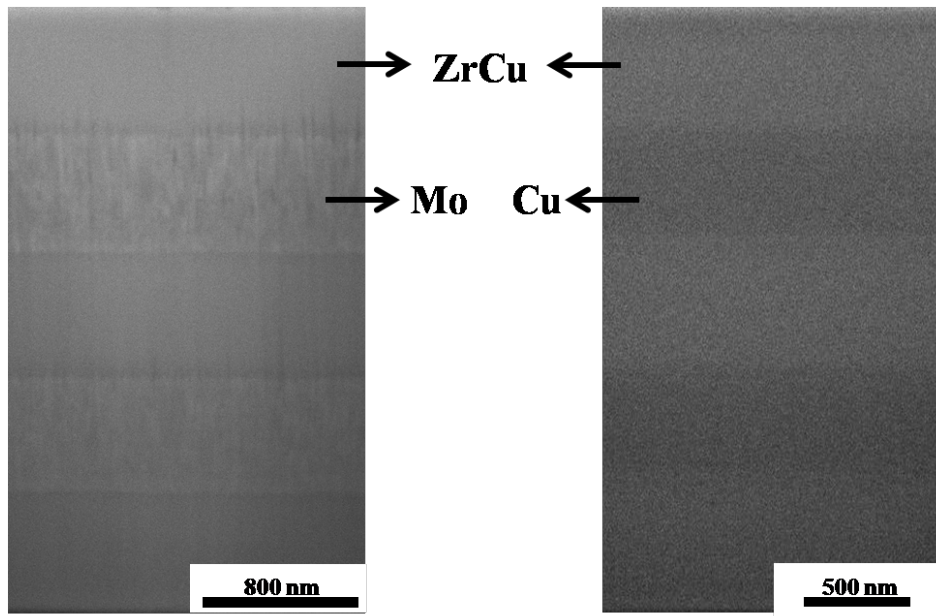


Figure 4.3 Cross-sectional SEM images of (a) ZrCu/Mo/ZrCu and (b) ZrCu/Cu/ZrCu multilayer thin films. The thickness of each layer is close to 500 ± 10 nm.

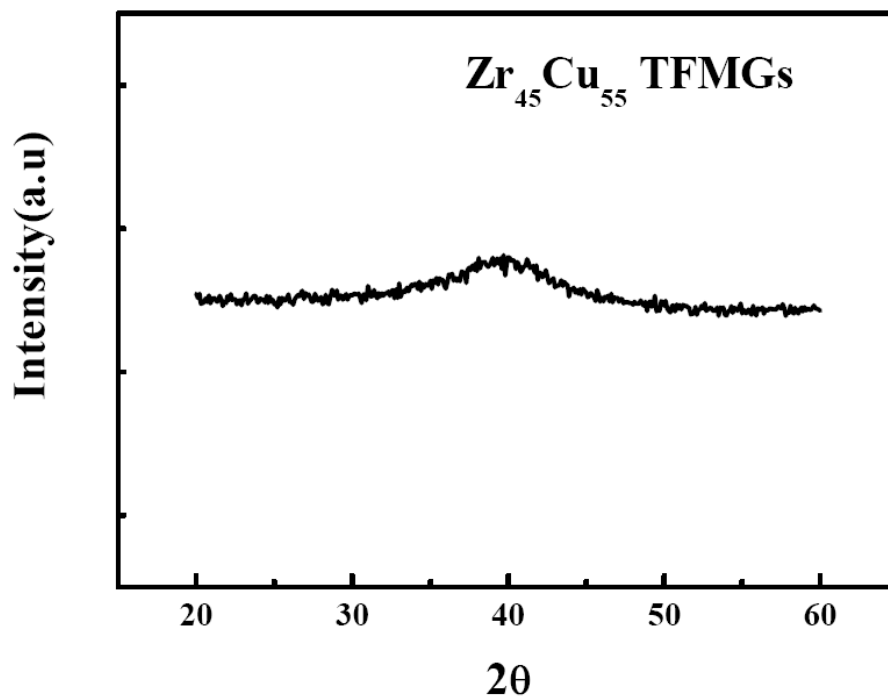


Figure 4.4 XRD pattern of the as-deposited ZrCu thin film.

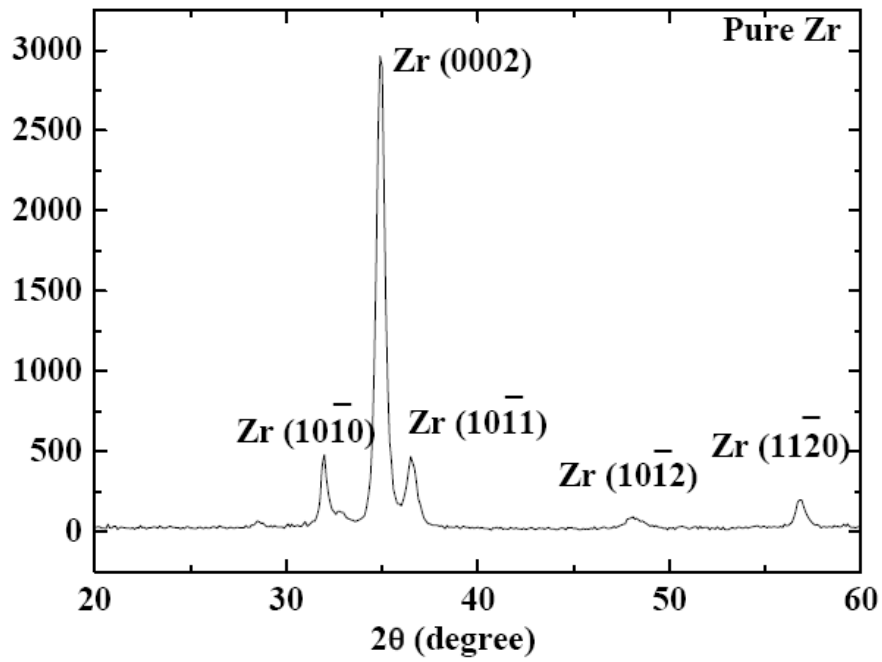


Figure 4.5 XRD pattern of the as-deposited pure Zr thin film [141]

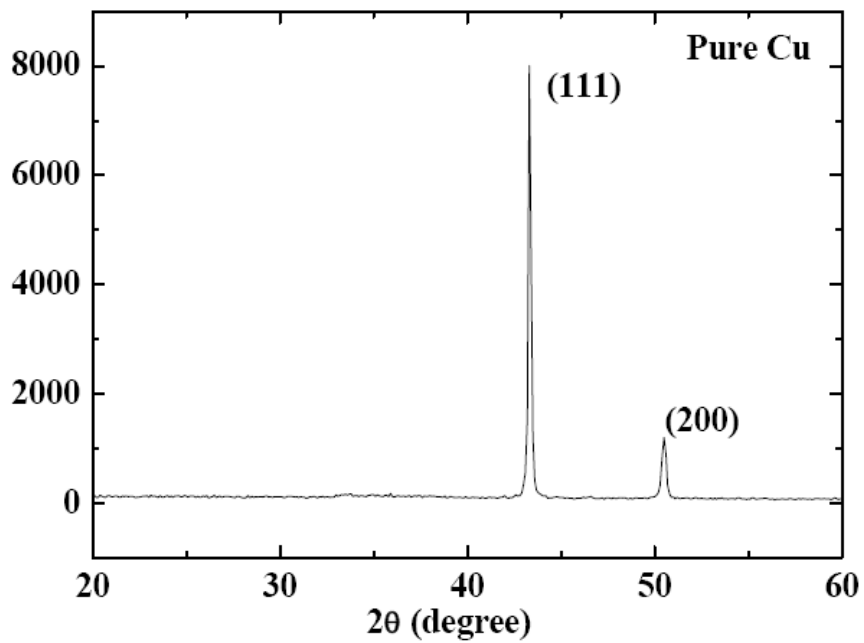


Figure 4.6 XRD pattern of the as-deposited Cu thin film [141].

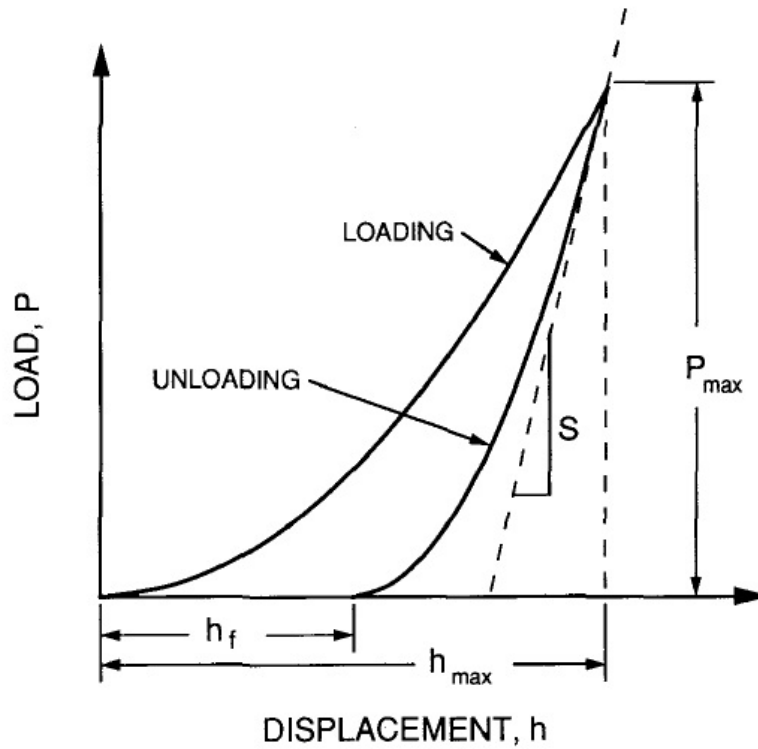


Figure 4.7 A representative load-displacement data for an indentation experiment. The quantities shown are P_{max} : the peak indentation load; h_{max} : the indenter displacement at peak load; h_f : the final depth of the contact impression after unloading; and S : the initial unloading stiffness [142].

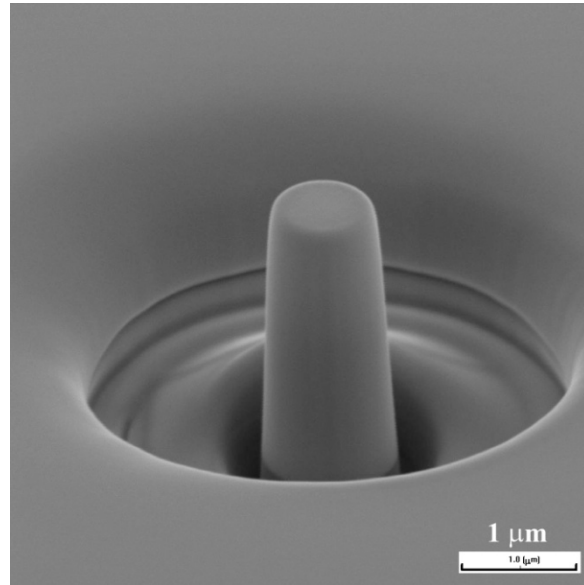


Figure 4.8 SEM micrograph of the undeformed ZrCu micropillar, 1 μm in diameter.

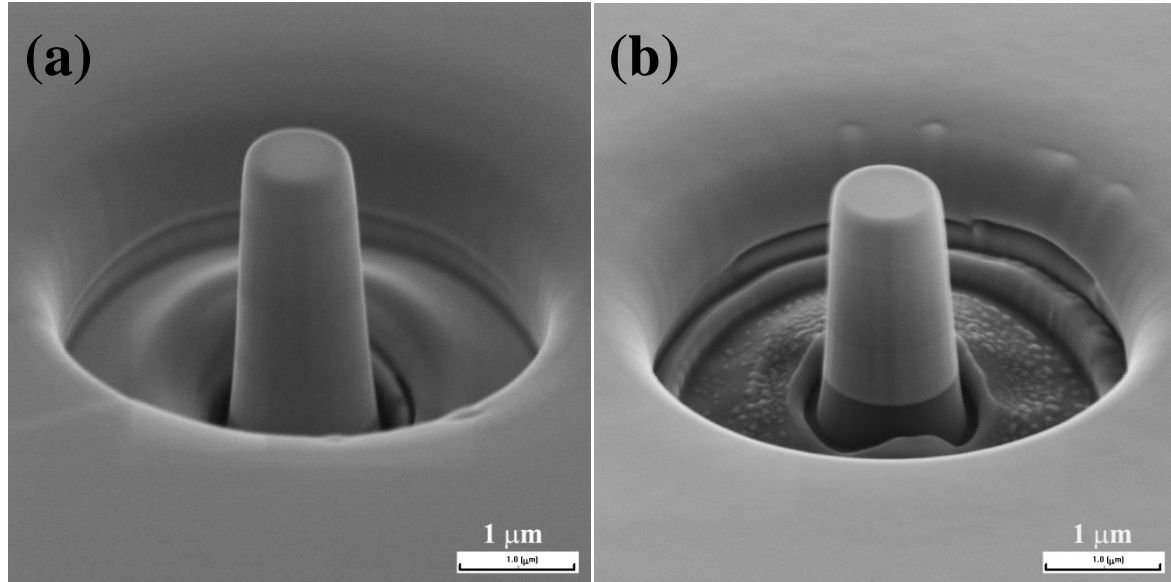


Figure 4.9 SEM micrographs of the undeformed (a) L7 and (b) L3 micropillars, 1 μm in diameter. (Note: In Fig. 4.9(b), the dark layer on the bottom of pillar is silicon wafer.)

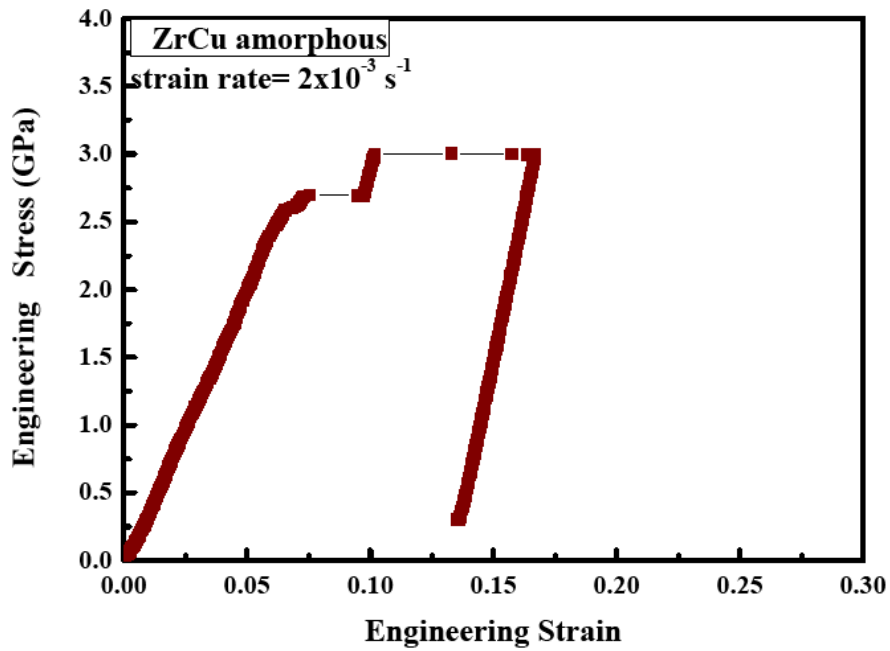


Figure 4.10 The compressive stress-strain curve of the monolithic ZrCu amorphous micropillar loaded at a strain rate of $2 \times 10^{-3} \text{ s}^{-1}$ to a preset displacement of 300 nm.

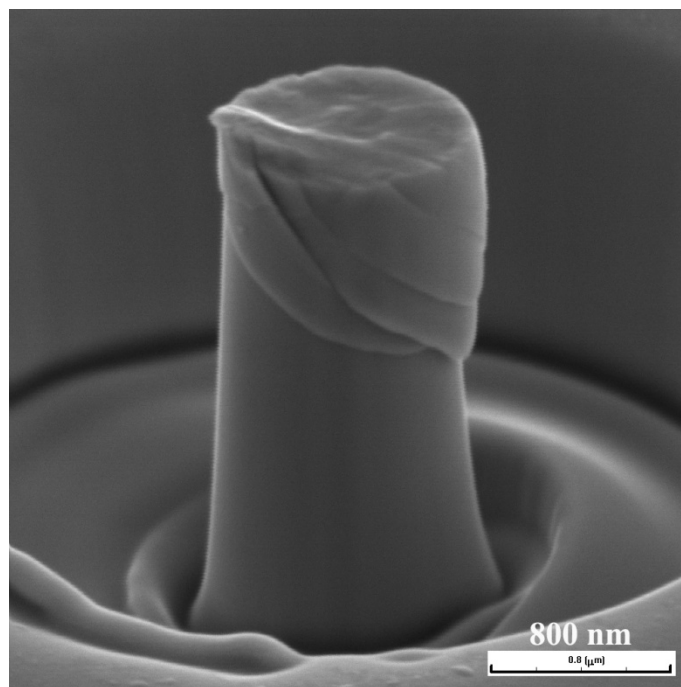


Figure 4.11 SEM micrograph of the deformed monolithic ZrCu amorphous micropillar.

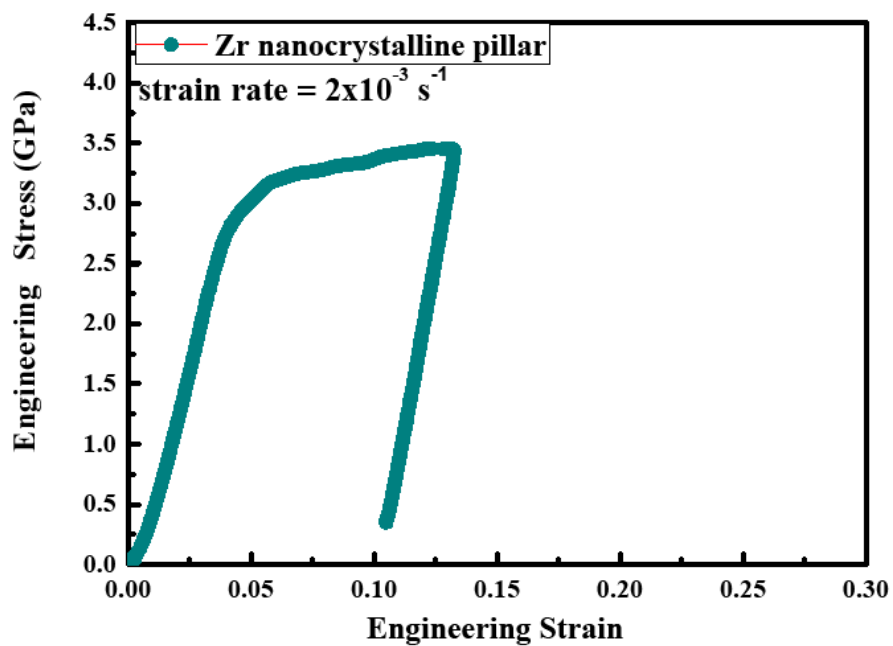


Figure 4.12 The compressive stress-strain curve of monolithic Zr nanocrystalline micropillar loaded at a strain rate of $2 \times 10^{-3} \text{ s}^{-1}$ to a preset displacement of 300 nm.

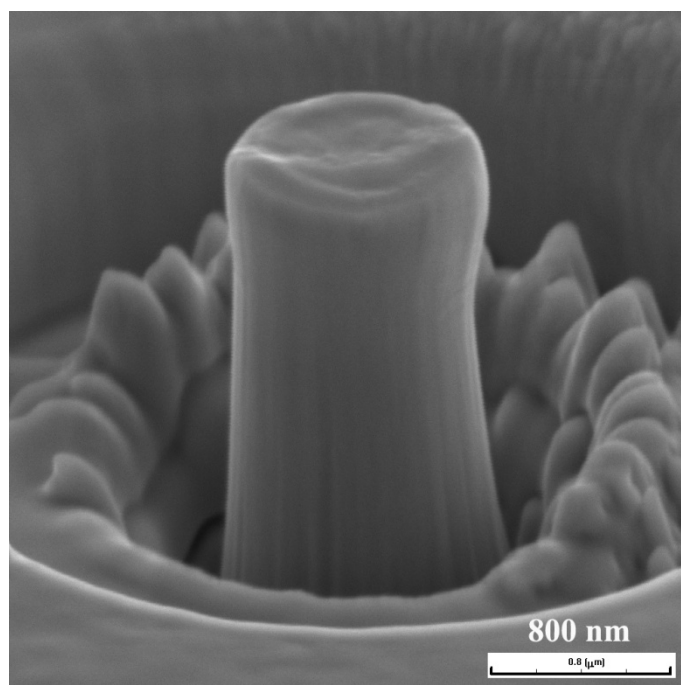


Figure 4.13 SEM micrograph of the deformed monolithic Zr nanocrystalline micropillar.

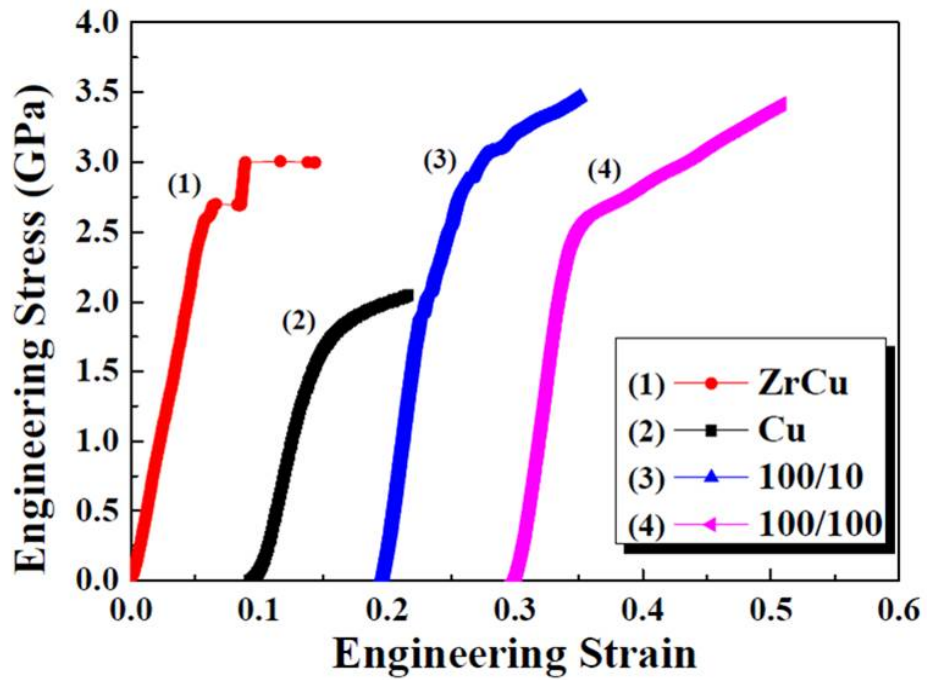


Figure 4.14 The engineering strain-stress curves of different micropillar samples loaded by microcompression tests.

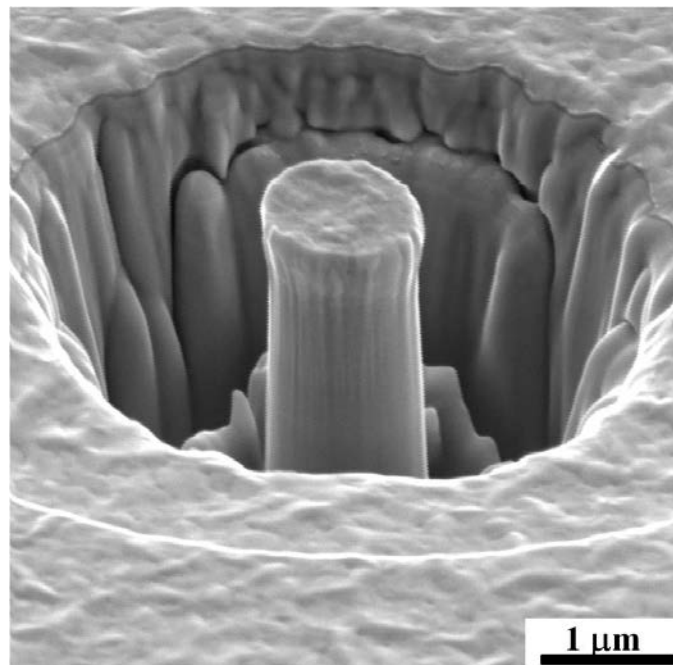


Figure 4.15 SEM micrographs showing the appearance of monolithic nanocrystalline Cu deformed micropillars samples, 1 μm in diameter.

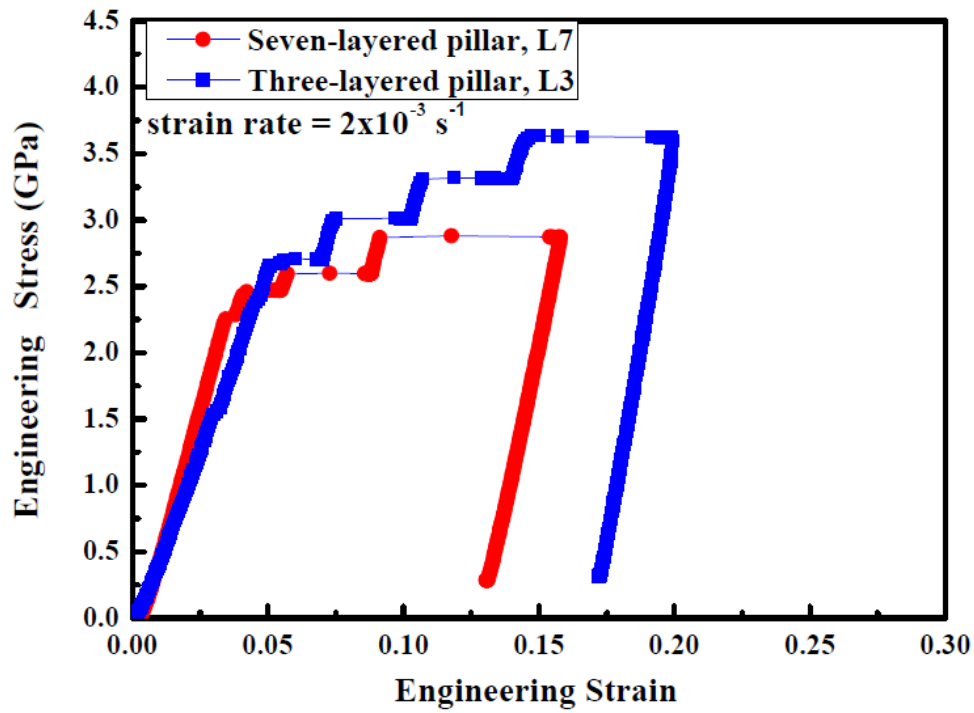


Figure 4.16 The engineering stress and strain curves of the L7 and L3 multilayered pillars compressed at $2 \times 10^{-3} \text{ s}^{-1}$ to a predetermined displacement of 300 nm (~15% strain).

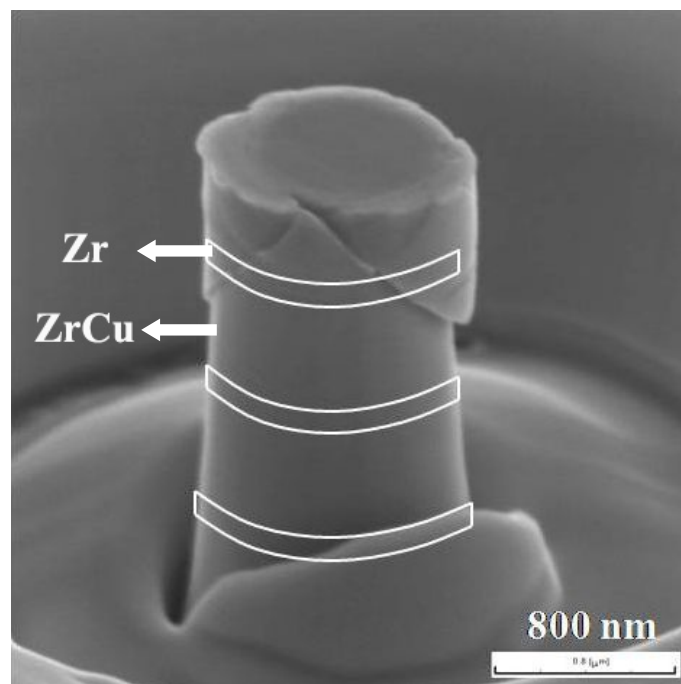


Figure 4.17 SEM micrograph of the deformed L7 ZrCu/Zr multilayer micropillar.

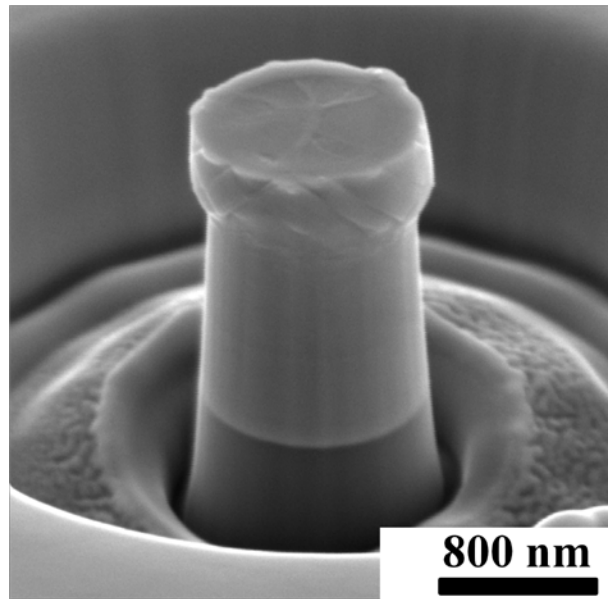


Figure 4.18 SEM micrograph of the deformed L3 ZrCu/Zr multilayer micropillar. The top amorphous layer is appreciably barreled. Whereas many localized shear bands form, there is no sign of deep penetration of shear bands in the nanocrystalline Zr layer.

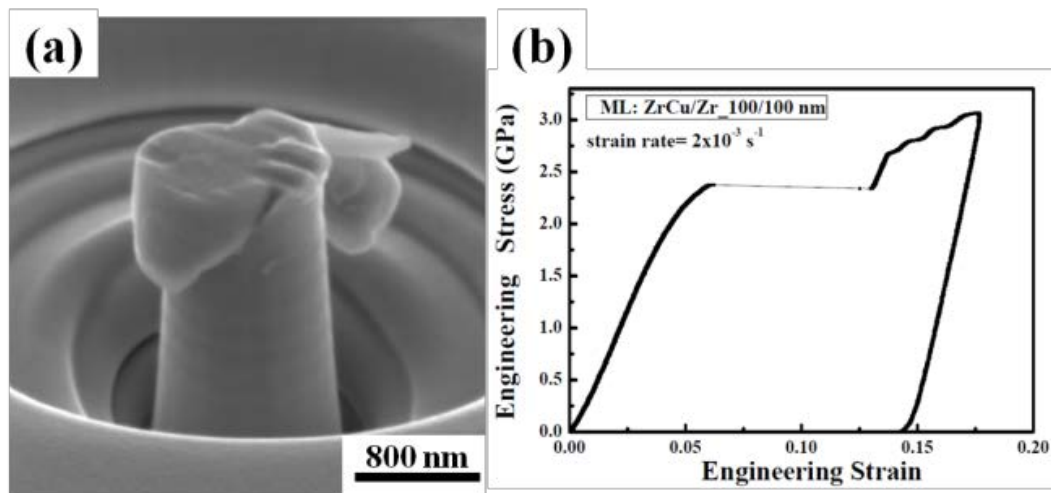


Figure 4.19 (a) SEM micrograph showing the compressed ZrCu/Zr (100/100 nm) pillar to a present displacement of 300 nm. (b) The engineering stress and strain curve of the ZrCu/Zr laminated pillar loaded at $2 \times 10^{-3} \text{ s}^{-1}$ to a preset displacement of 300 nm.

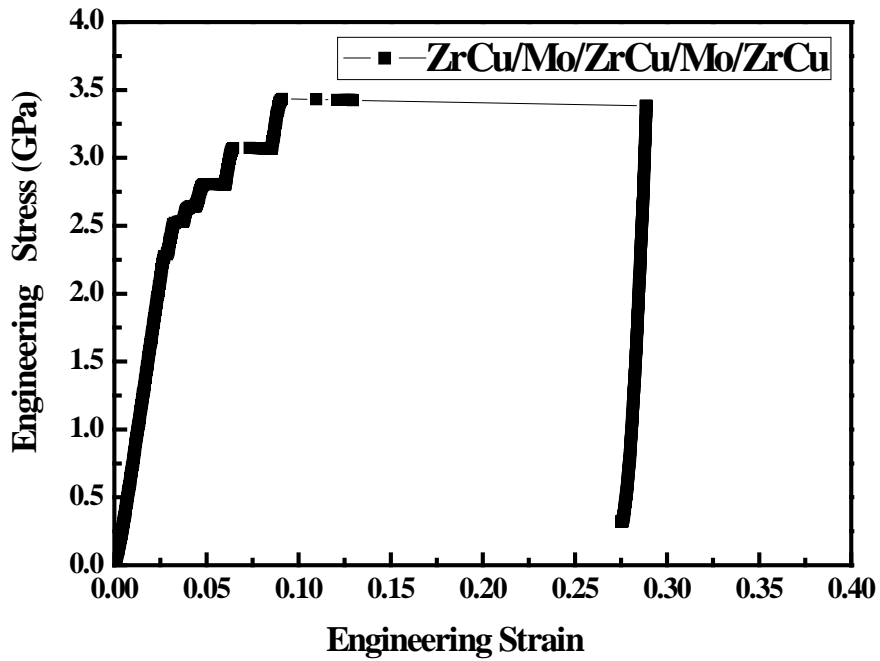


Figure 4.20 The engineering stress and strain curve of five-layer (ZrCu/Mo laminates) pillar loaded at $2 \times 10^{-3} \text{ s}^{-1}$ to a preset displacement of 300 nm.

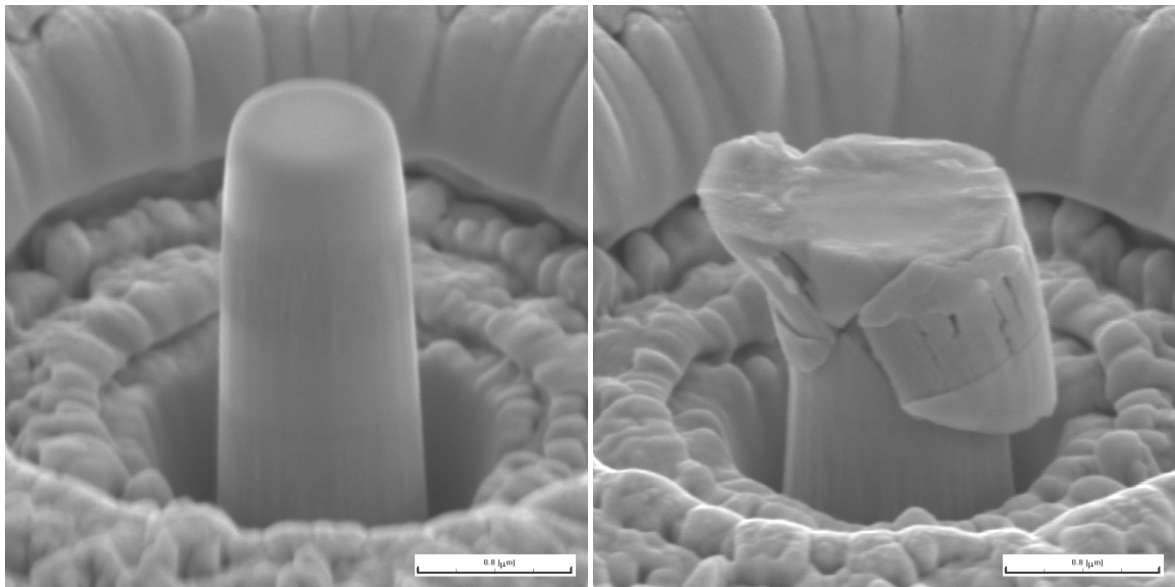


Figure 4.21 SEM micrographs showing: (a) 1- μm -diameter five-layer ZrCu/Mo micropillar. (b) the compressed pillars to a present displacement of 300 nm.

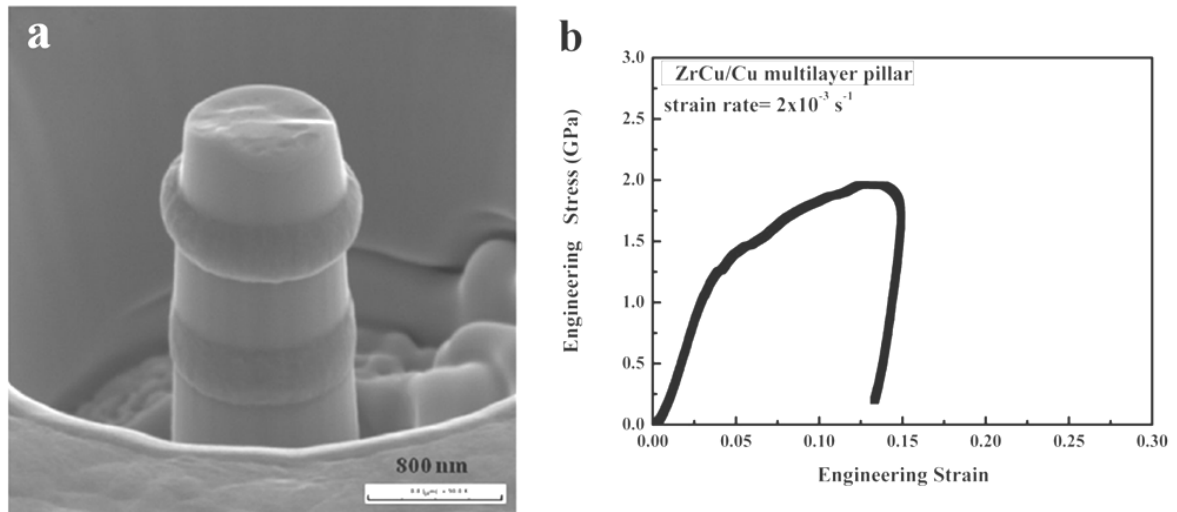


Figure 4.22 (a) SEM micrograph showing the ZrCu/Cu five-layer pillar compressed to a predetermined displacement of 300 nm (~15% strain), and (b) the recorded engineering stress and strain curve.

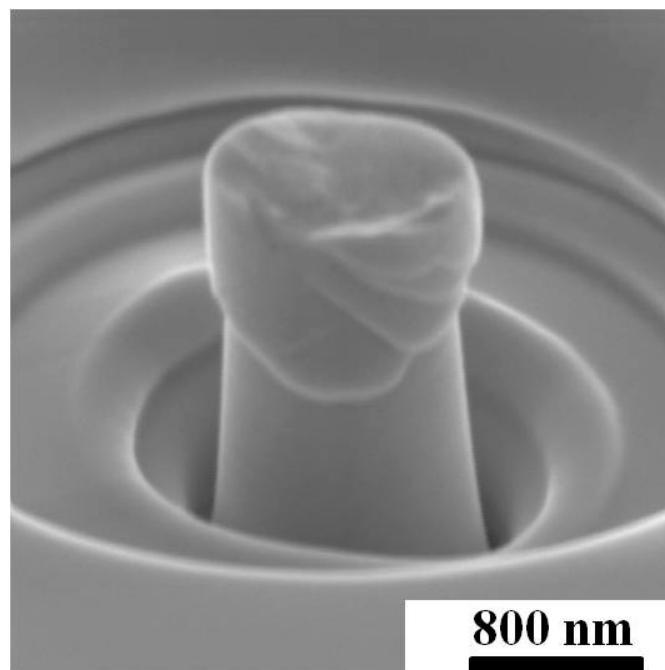


Figure 4.23 SEM micrographs showing the appearance of the ZrCu/Cu 100/10 nm deformed micropillars, 1 μm in diameter.

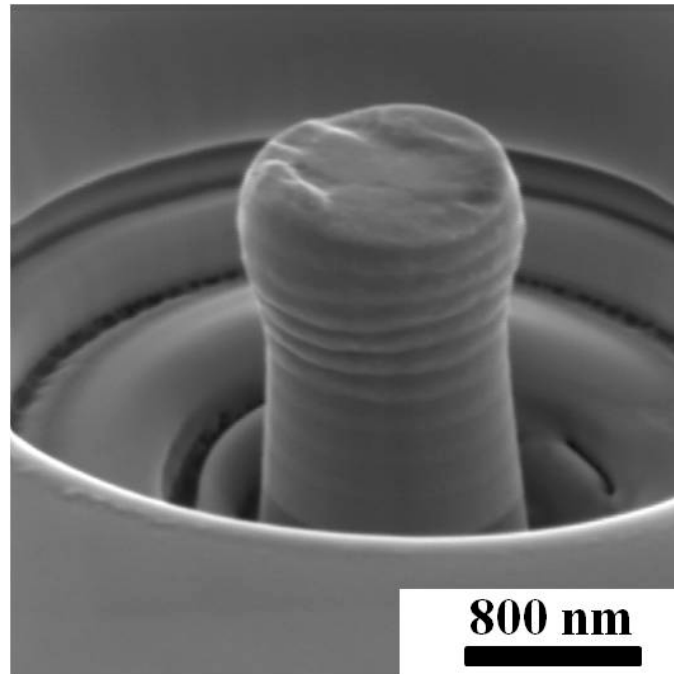


Figure 4.24 SEM micrographs showing the appearance of the round deformed micropillars of 100/100 nm ZrCu/Cu micropillar, 1 μm in diameter.

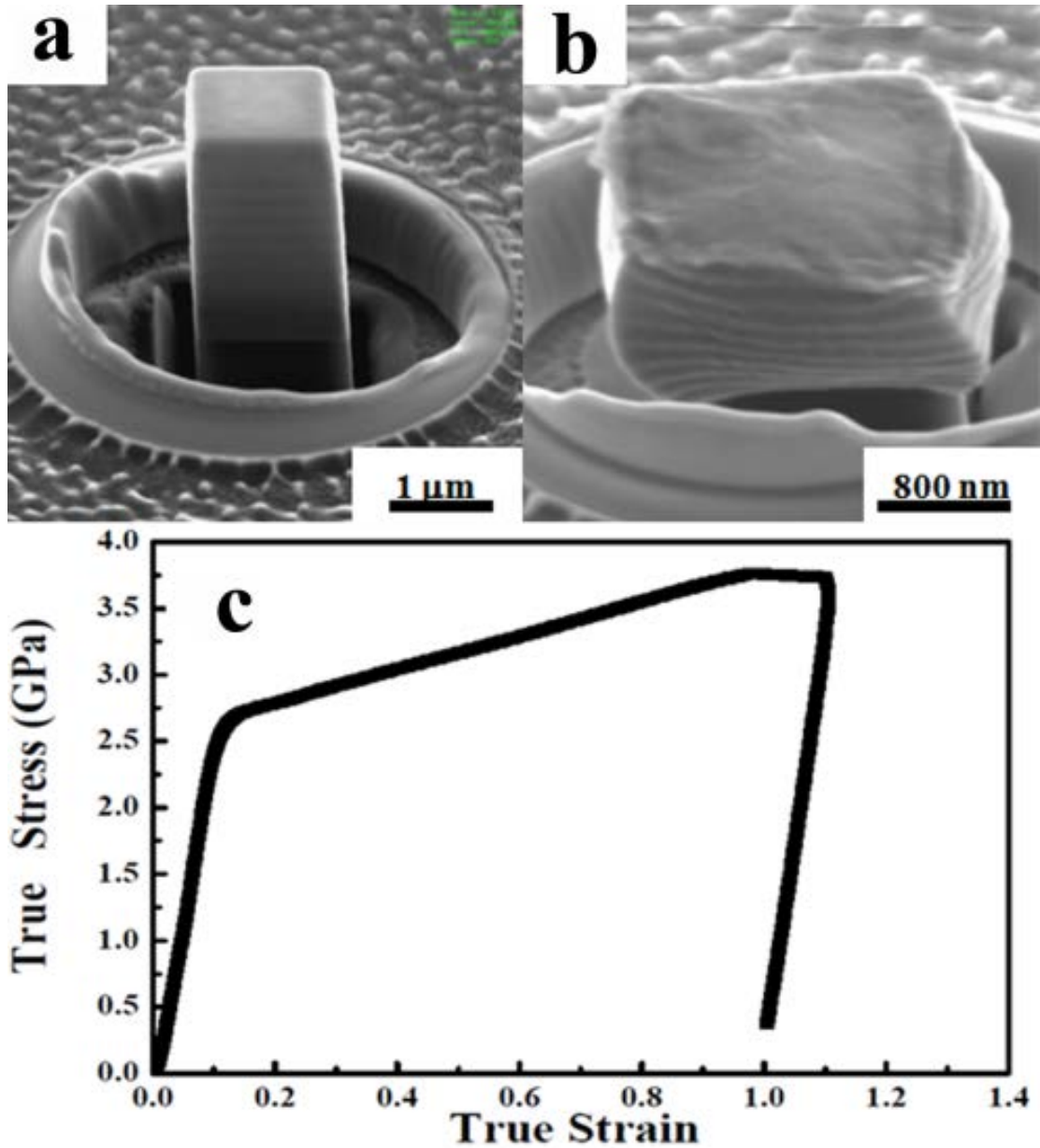


Figure 4.25 SEM micrographs showing the appearances of the (a) undeformed and (b) strained up to ~100% 100/100 nm ZrCu/Cu rectangular micropillars. (c) A typical true stress-strain curve of the 100/100 nm ZrCu/Cu rectangular micropillar subjected to microcompression test.

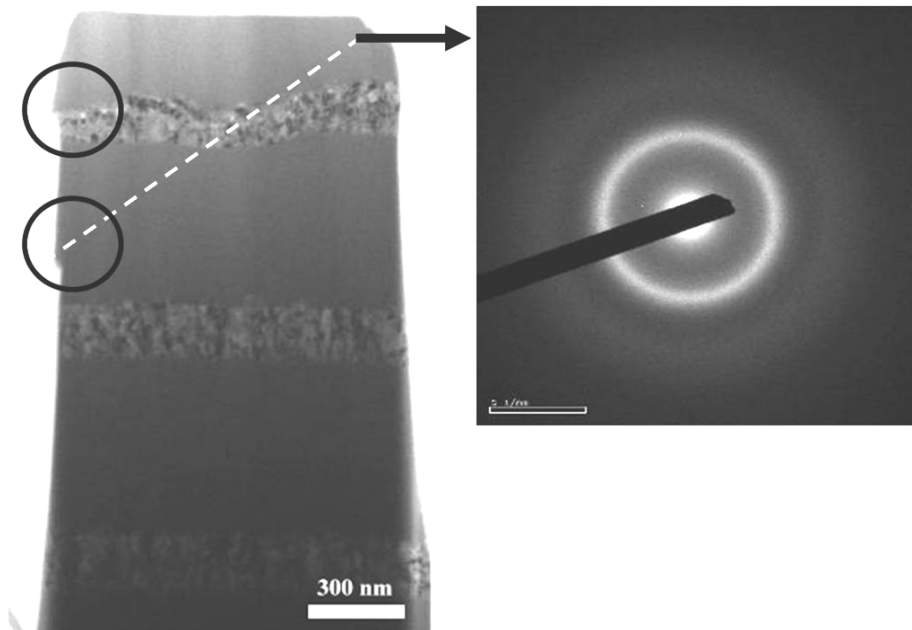


Figure 4.26 TEM longitudinal section of the L7 multilayer pillars compressed to a predetermined displacement of 300 nm (~15% strain).

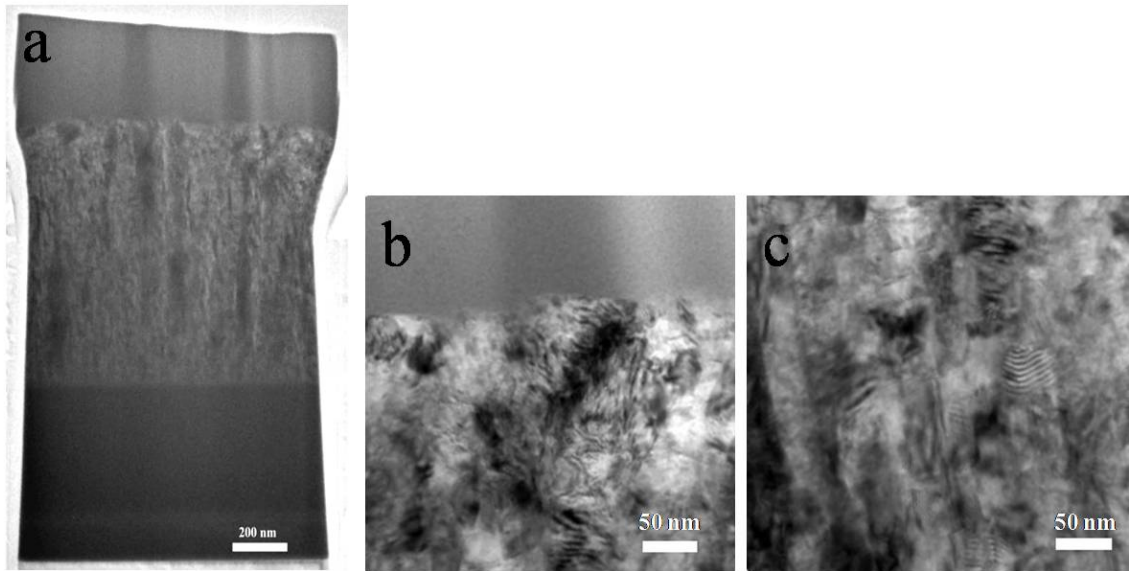


Figure 4.27 TEM micrographs showing the ZrCu/Zr interface of the deformed L3 pillar. The shear bands were stopped by Zr crystalline layer. The thickness of top amorphous was decreased from the 550 nm to 280 nm after the microcompression and the Zr layer was decreased from 880 nm to 830 nm. (b) and (c) TEM micrographs of the amorphous/crystalline interface and the deformed crystalline Zr layer.

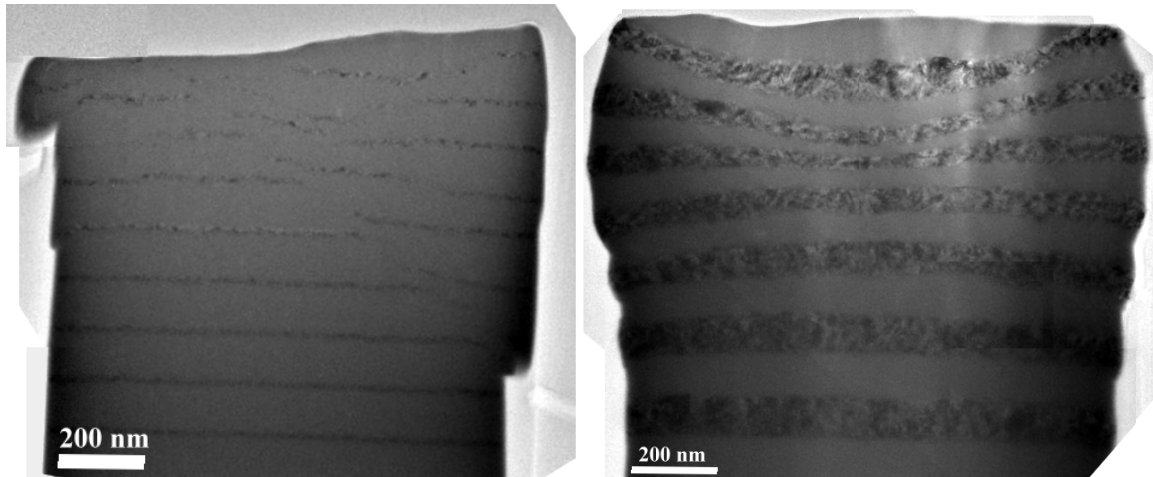


Figure 4.28 TEM micrographs showing the appearances of the deformed (a) 100/10 nm and (b) 100/100 nm ZrCu/Cu round micropillars.

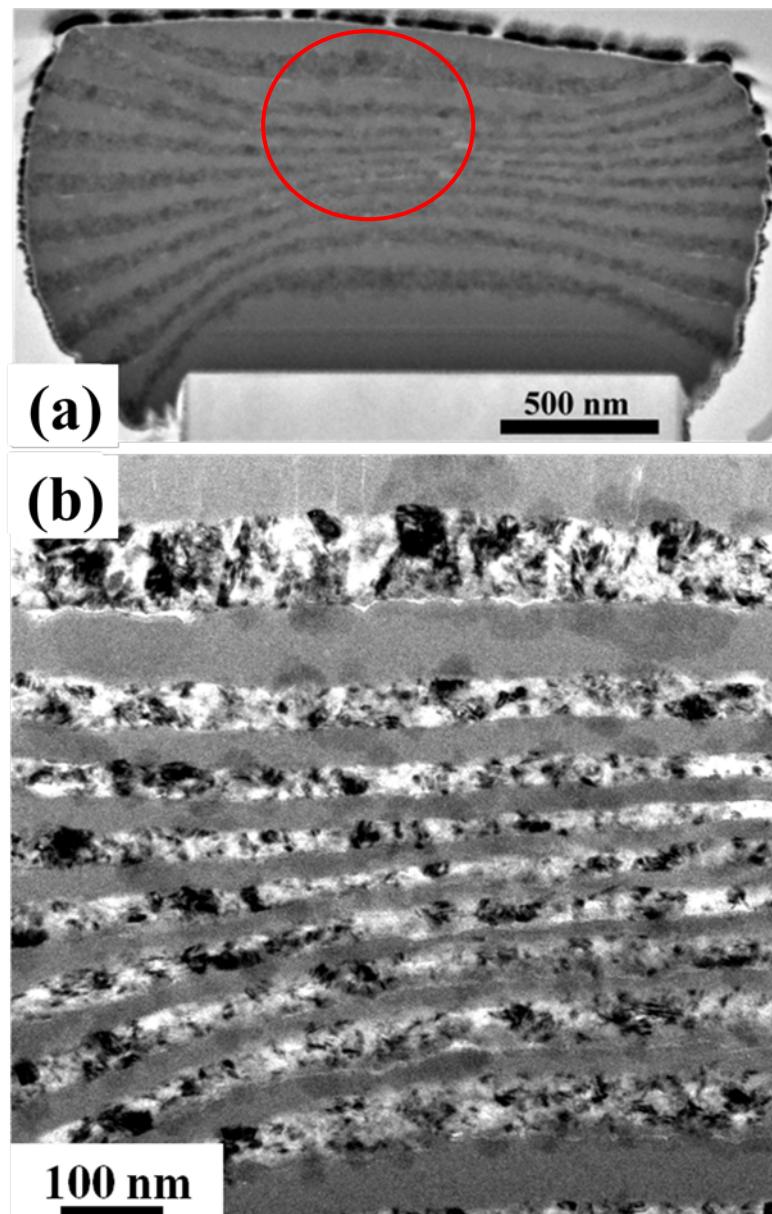


Figure 4.29 (a) TEM micrographs showing the appearances of the deformed 100/100 nm ZrCu/Cu rectangular micropillars. (b) High-magnitude TEM image of the circular region marked in Figure 4.29 (a).

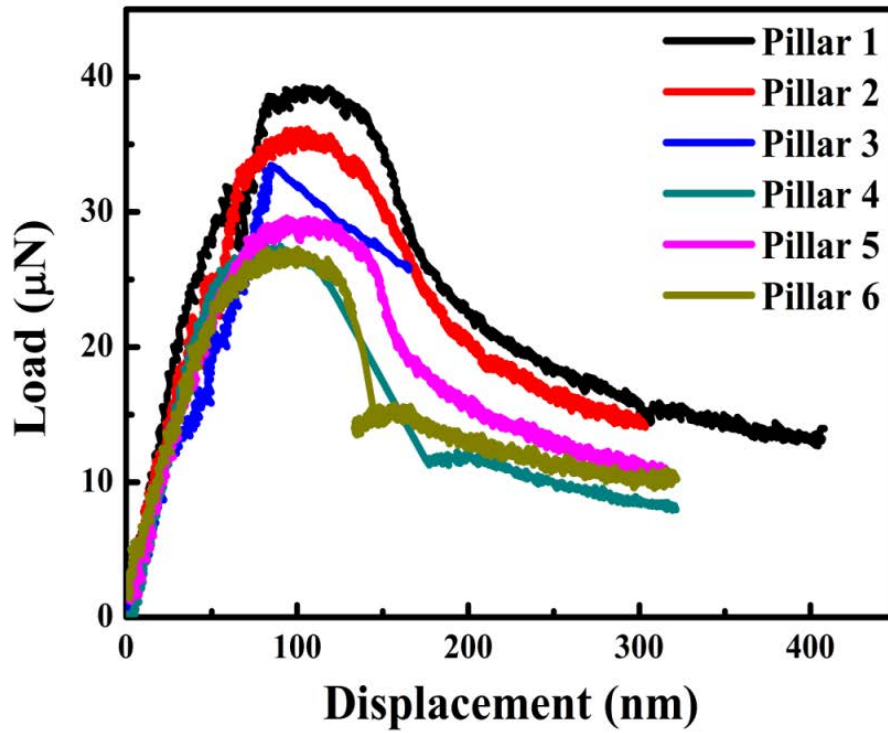


Figure 4.30 Representative load-displacement curves of the in situ TEM nanocompression tests on the ZrCu thin film metallic glass nanopillars, 140 nm in diameter.

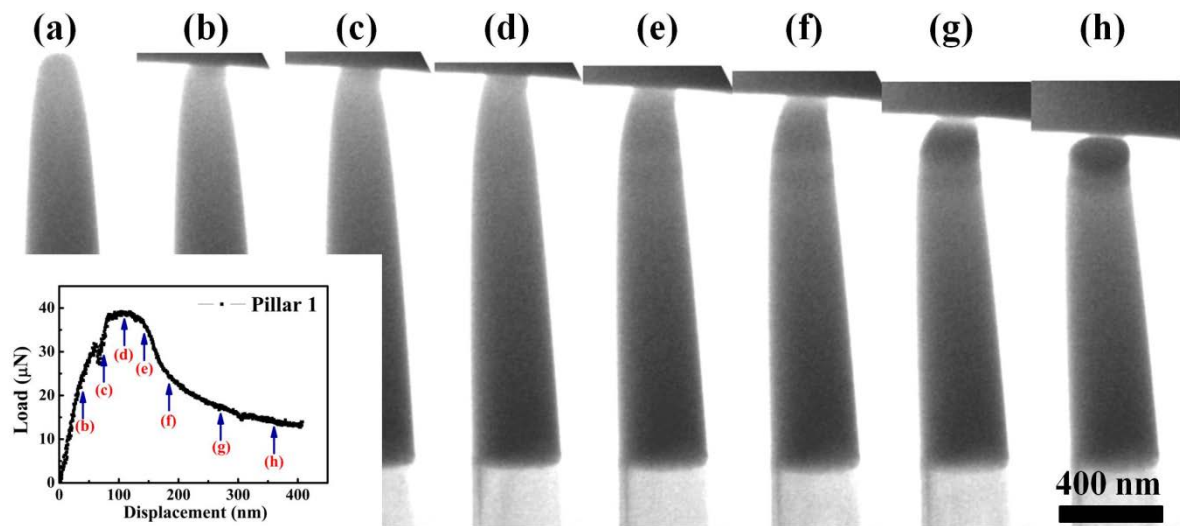


Figure 4.31 Video snaps taken from the in-situ TEM compression showing the deformation of Zr-based pillar (Pillar 1). The different stages of the nanocompression process are depicted by individual frames [(a)-(h)] at different strains: (a) undeformed, (b) ~2%, (c) ~4%, (d) ~6%, (e) ~8%, (f) ~10%, (g) ~15%, and (h) ~20%. The corresponding stress strain curve is inserted on the left bottom corner for point to point correspondence.

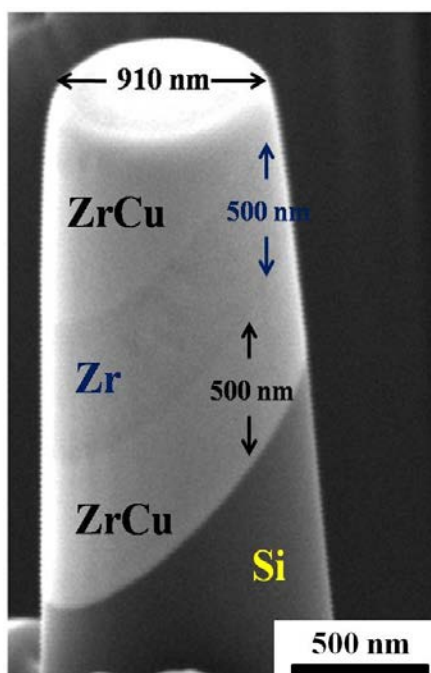


Figure 4.32 SEM image of the undeformed multilayered pillar, with labels of the diameter, height, and composition.

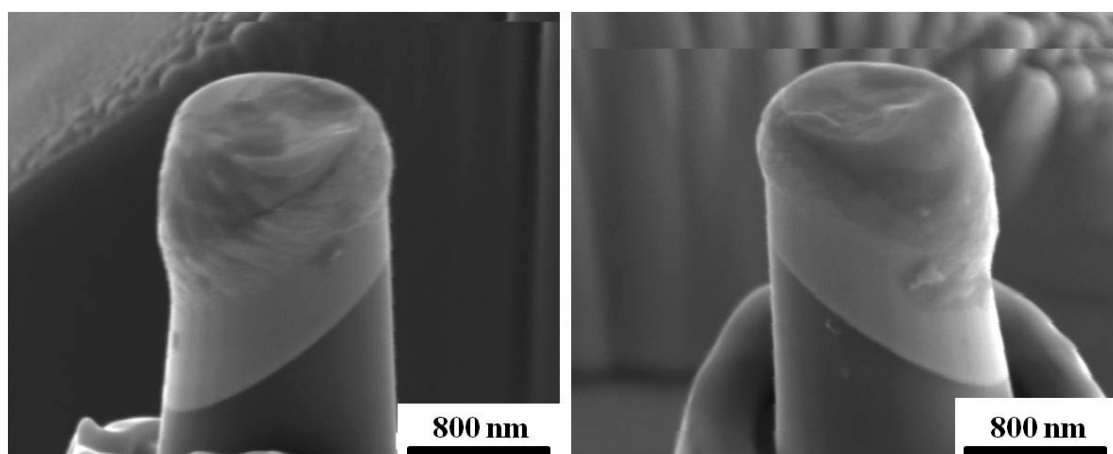


Figure 4.33 SEM images of the pillar deformed to the preset displacement of 260 nm, taken from two sides of the pillar.

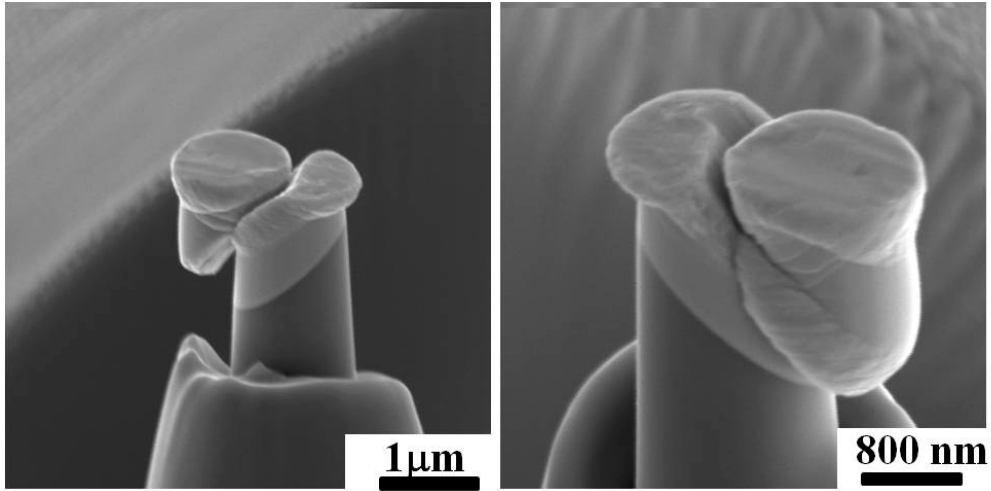


Figure 4.34 SEM images of the pillar deformed till to failure, taken from two sides of the pillar.

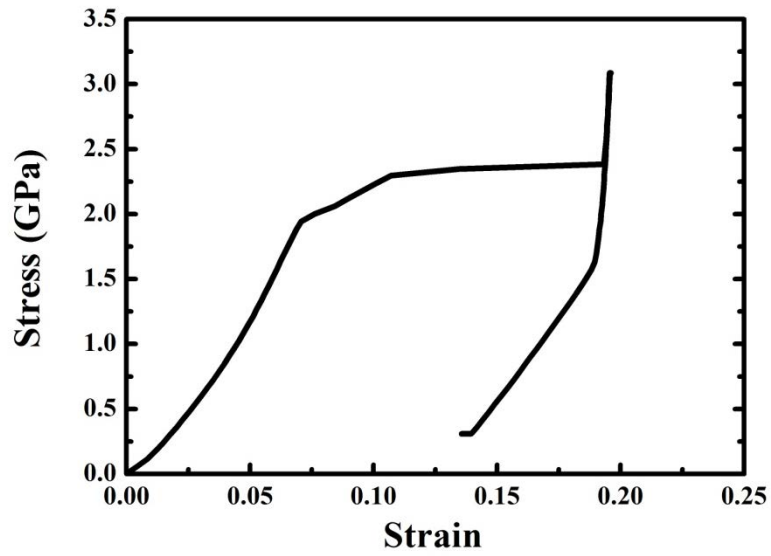


Figure 4.35 The compression stress and strain curve of the inclined multilayered pillar deformed till to failure.

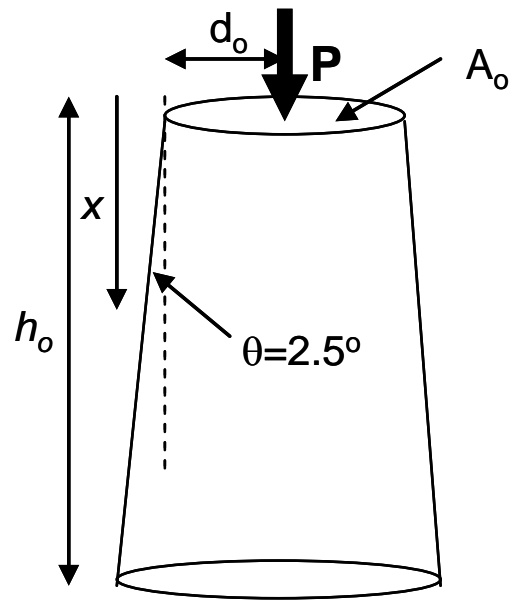


Figure 5.1 Schematic illustration for the deformation in a tapered sample.

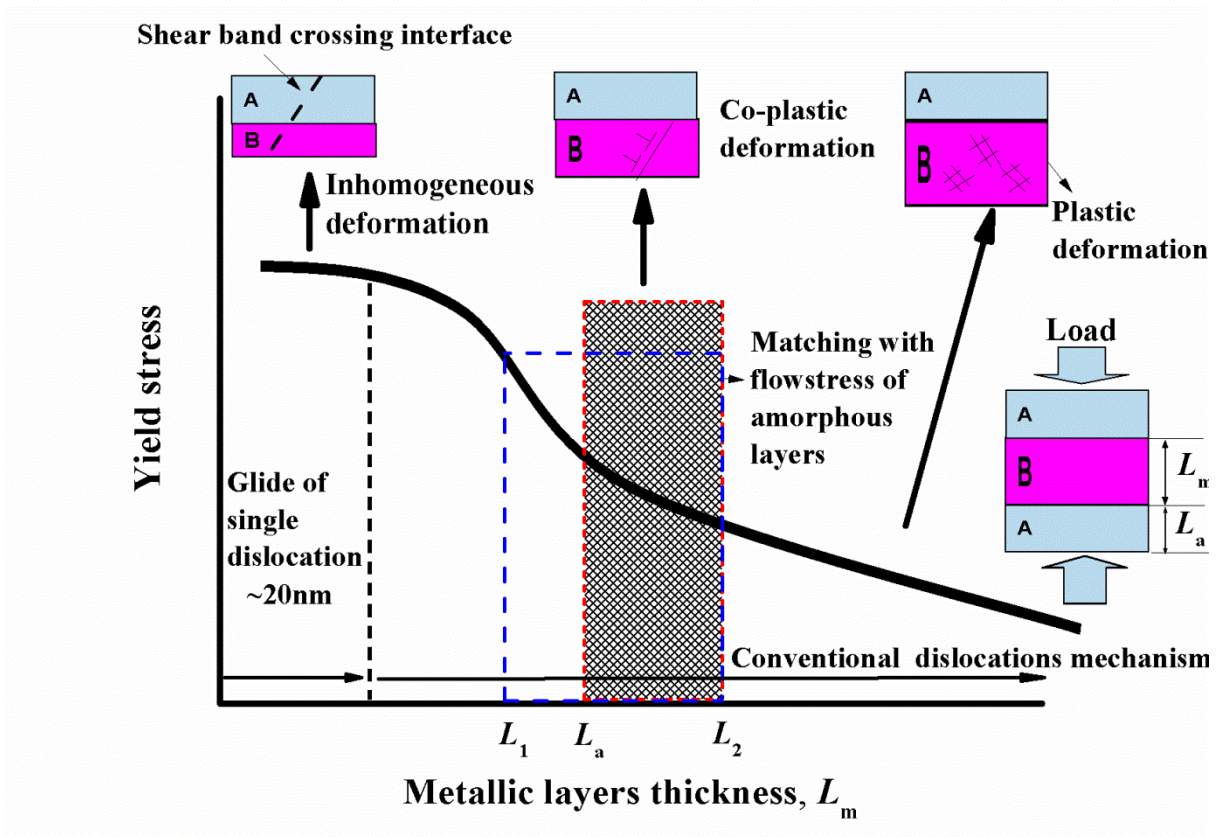


Figure 5.2 Schematic illustration of the deformation mechanism in the metallic amorphous/crystalline nanolayered composites as a function of metallic layers thickness.

A: inherently ductile metallic amorphous layers (e.g. ZrCu) with L_a thickness; B: soft pure metallic layers (e.g. Cu). Pronounced semi-homogeneous and superplastic-like deformation can occur when $L_a \leq L_m \leq L_2$.

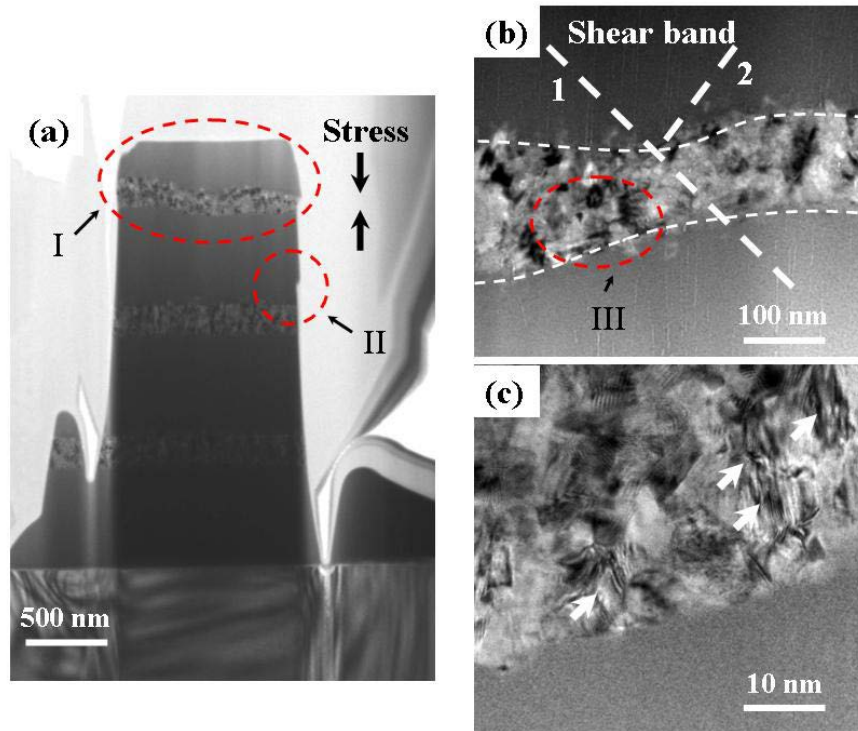


Figure 5.3 Showing the deformation planar defects (twins and stacking faults) in the nano-scale grained Zr layer, as indicated in Figure 5.3(c).

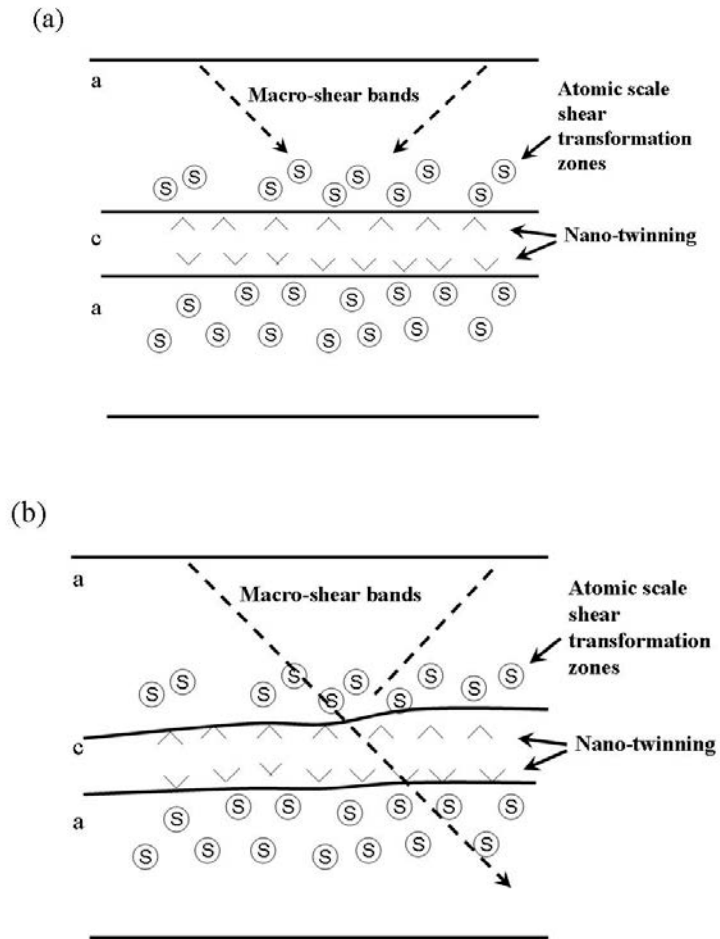


Figure 5.4 Schematic illustration of interaction between the amorphous/crystalline interfaces.

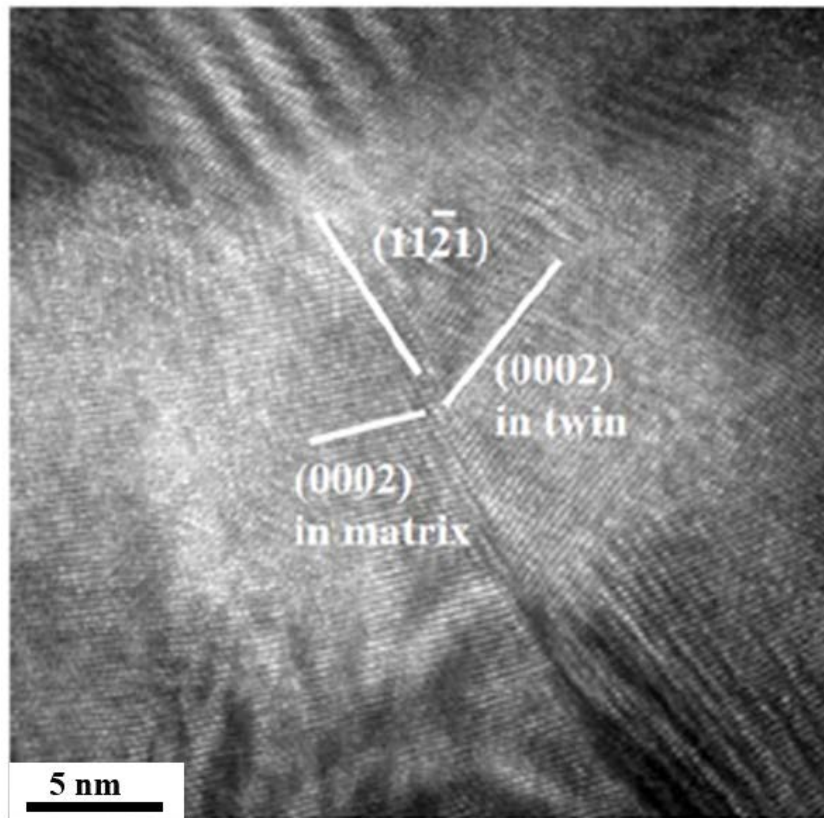


Figure 5.5 HRTEM lattice image showing one of the twinning operation in the nano-crystalline Zr layer. The (0002) planes in the matrix (on the left) possess an angle of 130° with respect to the (0002) planes in the twin region (on the right). The habit plane (or the *K1* undistorted plane) $(11\bar{2}1)$ lying at the center, possessing an angle of 68.93° with respect to both (0002) planes in the matrix and in the twin.

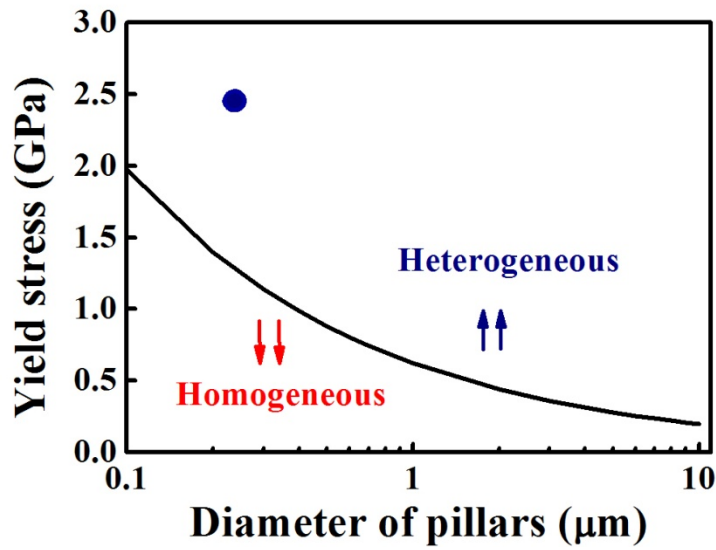


Figure 5.6 The calculated solid line showing the estimate of the minimum stress required to raise the strain energy high enough to allow for shear band formation. (Upper right region: shear banding heterogeneous deformation; lower left region: homogeneous deformation.)

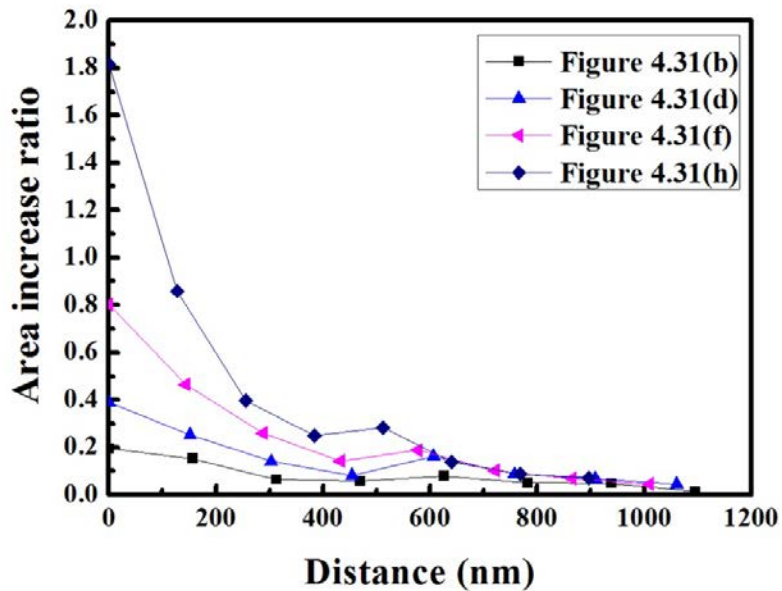


Figure 5.7 Change in cross-sectional area versus distance for Figures 4.31(b), (d), (f), and (h). Distance stands for distance the top of the pillar sample.

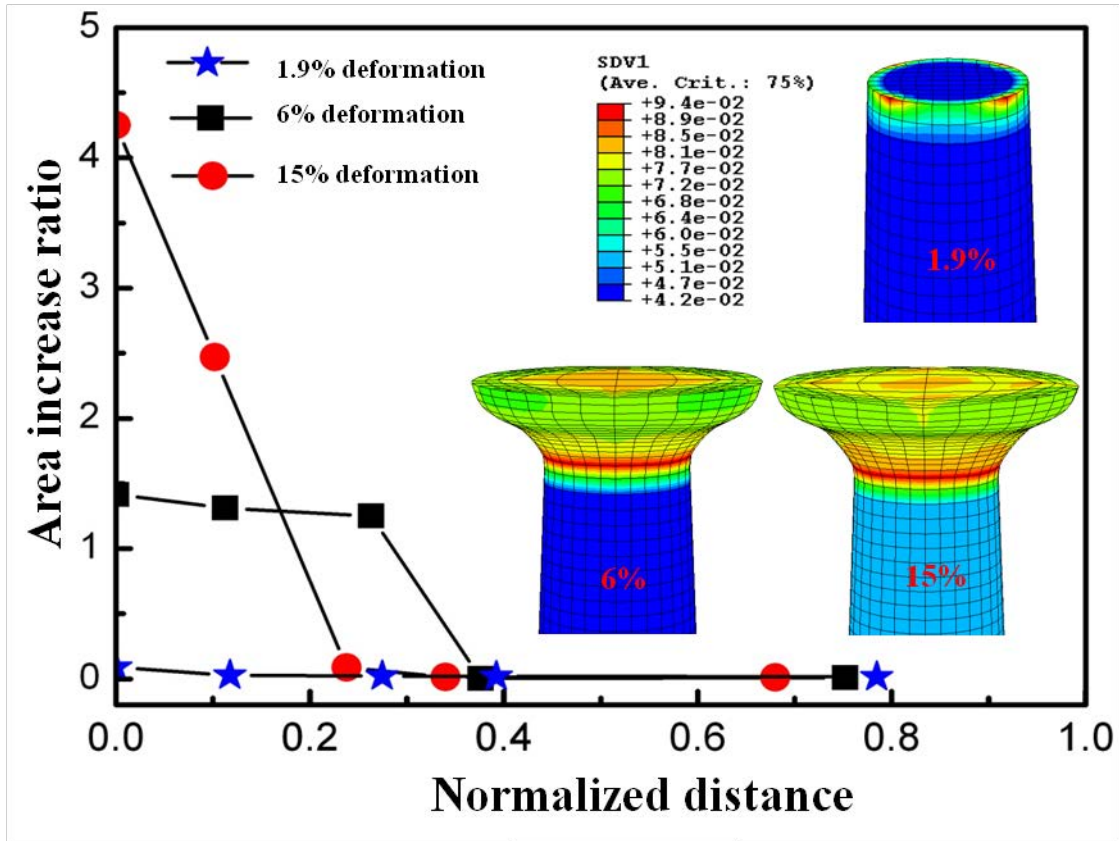


Figure 5.8 Area change ratio as a function of the distance from the specimen top (normalized by the base diameter) at three representative deformation stages with free volume contours in the insets. Contour plots are given in deformed mesh with displacement magnification ratios being 1 in all three directions.